FLOW OF VISCOELASTIC FLUIDS THROUGH BANKS OF CYLINDERS: AN EXPERIMENTAL AND NUMERICAL INVESTIGATION

by

William H. Hartt, IV

Dissertation submitted to the Faculty of Virginia Polytechnic Institute and State University in partial fulfillment of the requirements for the degree of

DOCTOR OF PHILOSOPHY

in

Chemical Engineering

APPROVED

Donald G. Baird

Dr. Donald G. Baird

Richey M. Davis

Dr. Richey M. Davis

Ronald D. Kriz

Dr. Ronald D. Kriz

A. C. Loos

Dr. A.C. Loos

Garth L. Wilkes

Dr. Garth L. Wilkes

January 1995

FLOW OF VISCOELASTIC FLUIDS THROUGH BANKS OF CYLINDERS: AN EXPERIMENTAL AND NUMERICAL INVESTIGATION

by

William H. Hartt, IV

Donald G. Baird, Chairman

Chemical Engineering

(ABSTRACT)

In this research it is attempted to determine whether the pressure drop for a polymer melt flowing transversely through a square array of cylinders can be predicted using purely viscous models or whether a viscoelastic constitutive equation is required. To predict these pressure drops, finite element calculations were performed using the generalized Newtonian fluid (GNF) model with the Bird-Carreau viscosity function, as well as two viscoelastic constitutive equations, the Phan-Thien and Tanner (PTT) model and the Rivlin-Sawyers (RS) model with the Papanastasiou, Scriven, and Macosko (PSM) damping function. The constitutive equations were fit to the steady shear viscosity of a LLDPE melt and a LDPE melt. The PTT and RS models were also fit to uniaxial extensional stress growth data for each melt. The predictions of the pressure drop by means of the finite element calculations and a capillary model based on Darcy's Law were compared to pressure drops from experiments performed with the two polymer melts. The agreement between experimental data and theoretical predictions was best for the calculations using the PTT model. The calculations using the PTT model as the constitutive equation indicate that time dependent fluid

properties and extensional rheology must be correctly predicted by the constitutive equation used if accurate pressure drops of viscoelastic fluids flowing through banks of cylinders are to be calculated.

This research is also concerned with the comparison of the results of numerical simulation of confined flow past a cylinder to birefringence data for two polymer melts. The Phan-Thien and Tanner (PTT) constitutive equation and the Rivlin-Sawyers constitutive equation with the Papanastasiou, Scriven, and Macosko (PSM) damping function were each fit to the shear viscosity and extensional viscosity data of both linear low-density polyethylene (LLDPE) and low-density polyethylene (LDPE) melts to determine the values of the model parameters. Finite element calculations were carried out using the 4x4SUPG and 4x4SU methods for the PTT model and the method developed by Dupont et al. for the RS model. Isochromatic birefringence patterns calculated from the predicted stress field and the stress-optic law were compared to birefringence data. Agreement was found between the birefringence data and the numerical predictions, except in the immediate vicinity of the cylinder surface. Large extensional stresses were observed and predicted along the centerline downstream of the cylinder for LDPE. This behavior was not observed or predicted for LLDPE. Stress fields obtained from birefringence measurements for LDPE flowing past three cylinders in a channel indicate an effect of deformation history on the flow behavior of LDPE. It is shown that the PTT model does not correctly predict the rheological behavior of LDPE as a function of shear history because the time scale of structural recovery is much longer than the relaxation time associated with viscoelasticity.

To my family

Acknowledgements

The author wishes to express his appreciation to professor Donald G. Baird for the patience, endurance, and guidance which was given. The author would also like to express his gratitude to the faculty of the Chemical Engineering, Chemistry, and Engineering Science and Mechanics departments for his formal education. Special appreciation goes to my committee, Profs. Davis, Kriz, Loos, Wilkes, and Ragab.

The author would also like to express his appreciation to the following people:

My wife, how can I ever thank you.

All members of Dr. Baird's lab, for teaching me some valuable lesson in some way or another.

Drs. Dimitris Collias, Hugh O'Donnell, and Paulo De Souza for their guidance and willingness to jump into any technical discussion, and take the opposing viewpoint on a whim.

The new kids: Mike McLeod, Chris Robertson, and Rob Young for making things entertaining.

Members of Drs. Wilkes's and Davis's lab for trying to convince me that all matter is not a continuum.

Doug Macrae, for not. Special thanks for all of his SGI help.

Dr. Jo Ellen DePorter for showing me that Ph.D.'s can be cool.

The National Science Foundation for feeding me.

Original Contributions

The following is a list of original contributions contained within this dissertation:

1. An explanation of the effect of transient rheology and extensional rheology on the pressure drop of viscoelastic fluids flowing through porous media.

2. The conclusion that viscoelastic models are required if accurate calculations of flow behavior of polymer melts in porous media are desired.

3. Determination of the stress field of two different polymer melts flowing past a cylinder in a planar channel, showing the effect of extensional strain hardening behavior.

4. Observation of the effect of deformation history on the flow of LDPE past cylinders in a planar channel.

Format of Dissertation

This dissertation is written in a journal format. Chapters 3 and 4 are self-contained papers that separately describe experiments, results, and conclusions pertinent to each chapter.

TABLE OF CONTENTS

List of Figures

List of Tables

1.0 Introduction

Flow of viscoelastic fluids through banks of cylinders is of practical interest in many industrial operations. For example, the impregnation of thermoplastic composite fiber tows has been the focus of a great deal of research recently. There are currently no accurate methods available to predict a priori the pressure drops required in the impregnation of composites. While many researchers are modifying the traditional approach to porous media first proposed by Darcy [1,2] which is adequate for most problems involving Newtonian fluids, rheologists have begun to examine the fundamental characteristics of the flow of viscoelastic fluids in geometries typical of composite fiber tows. Specifically, researchers have been attempting to predict pressure drops of fluids with elasticity flowing transverse to ideal arrays of cylinders [3,4,5]. Other industrial processes which involve flow geometries similar to beds of cylinders are enhanced oil recovery and many injection molding processes involving drop-out pins. Enhanced oil recovery processes often involve flow of dilute solutions of polymers into porous media which may be treated as a similar problem to banks of cylinders. In addition, many manufacturing processes involve flow of molten polymers around cylindrical obstructions. Currently there are no methods of predicting pressure drops or flow kinematics which occur as viscoelastic fluids flow through banks of cylinders or any other type of porous media.

Viscoelastic fluids differ from Newtonian fluids in several ways. The viscosity of viscoelastic fluids is generally dependent on the shear rate, while a Newtonian fluid has a constant viscosity. Viscoelastic fluids also behave differently from Newtonian fluids in extensional, or stretching flows. Viscoelastic fluids often have an extensional viscosity greater than three times the shear viscosity as in the case for Newtonian

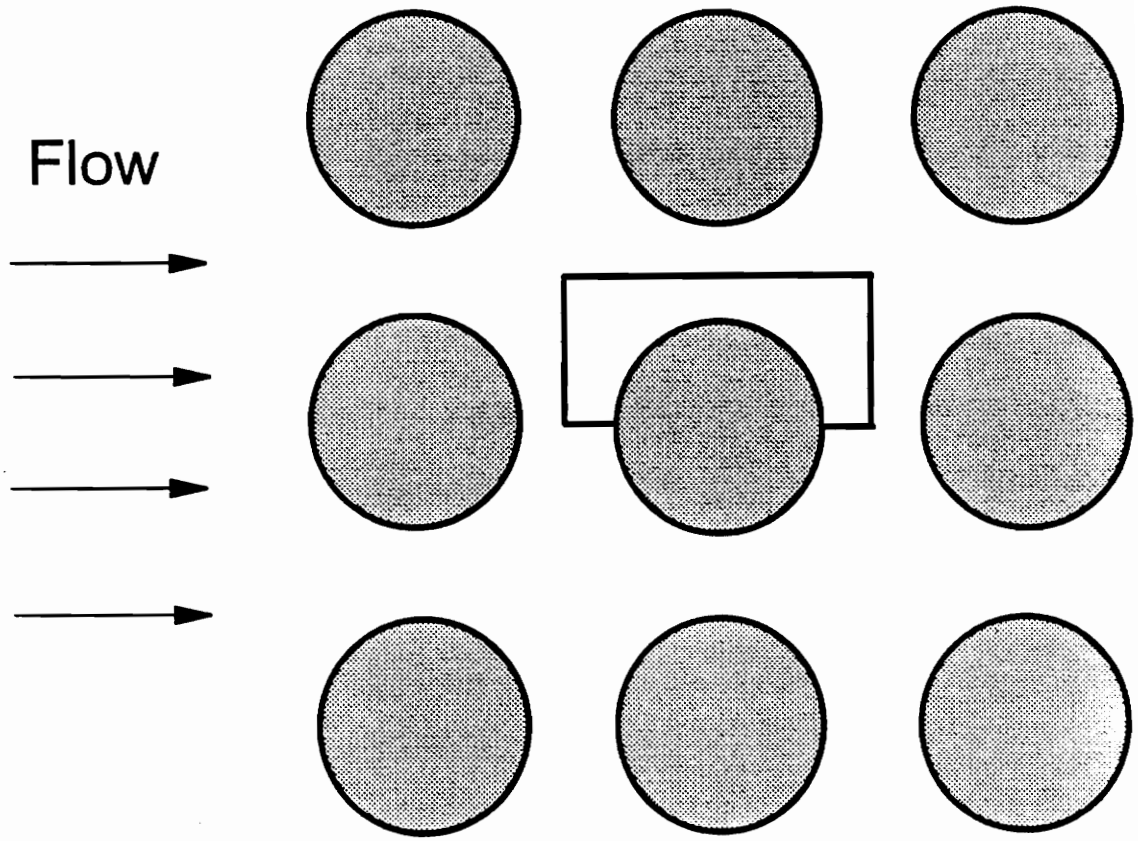

Figure 1.1. Flow geometry for transverse flow through a square array of cylinders. The shaded area is referred to as a unit cell.

fluids. The final difference between viscoelastic and Newtonian fluids which will be mentioned here is fluid memory. The flow behavior of viscoelastic fluids is dependent on previous flow history while Newtonian fluid behavior is not.

All of the behavior discussed above affects the flow of viscoelastic fluids in banks of cylinders. The converging and diverging nature of the geometry shown in Fig. 1.1 results in high shear rates as well as high extension rates. In addition, fluid memory has an impact on the resistance of flow through this geometry since the fluid experiences a series of accelerations and decelerations as it flows between successive cylinders.

Recent research has been focused on calculating the pressure drop in a unit cell, as shown in Fig. 1.1, and assuming that this pressure drop is additive throughout the flow domain [7,8]. All of the calculations performed to date have predicted a decreasing flow resistance as flow rate is increased, while many experiments show an increasing flow resistance as flow rate is increased [7,8]. There is very little experimental data for simple geometries which may be used to evaluate models, especially for polymer melts. The experimental data that does exist for the flow of viscoelastic fluids through banks of cylinders or other similar geometries generally exhibits an increased flow resistance when compared to Newtonian fluids. Most experiments have been performed in very complex geometries such as granular beds or mobile fiber beds where analysis of the flow is difficult. In addition, only pressure drop versus flow rate data is available in these experiments. Therefore analysis of failure of mathematical models to predict experimental behavior is not very thorough.

There is a need for detailed experiments characterizing the flow of viscoelastic fluids around cylinders so that a more complete comparison is available for computational results. A strict comparison of a numerical simulation to an experiment

requires measurements of the fluid velocity, stresses, and pressure. Flow visualization techniques such as particle tracking and birefringence allow these unknowns to be measured experimentally. An important assumption which should be addressed in flow visualization measurements is the additivity of pressure drops of each unit cell as shown in fig. 1. Viscoelastic fluid memory may have a significant impact on the pressure drop in successive unit cells. Another issue which should be adressed is the extensional behavior of the viscoelastic fluid which is being examined, experimentally or numerically. Therefore the choice of flow geometry and fluid are critical if useful information is to be gained.

The ultimate goal of this research is to accurately predict the pressure drops of viscoelastic fluids flowing through an ideal bank of cylinders. To accomplish this goal, the characteristics of the viscoelastic flow past a single cylinder, two cylinders, and three cylinders will be measured and compare with computations. The results of these experiments and computations will determine how many cylinders need to be taken into account when computing pressure drops through banks of cylinders.

2.0 Literature Review

In this chapter, previous research which is relevant to the experimental characteristics and numerical simulation of viscoelastic flow between cylinders will be reviewed. In section 2.1, traditional approaches to flow through porous media will be discussed. Although the approaches have been shown to be inadequate for predicting viscoelastic flow behavior, the reasons for these shortcomings are useful in describing viscoelastic effects. In section 2.2, experimental investigations of flow of viscoelastic fluids through banks of cylinders will be reviewed and in section 2.3, numerical simulations of viscoelastic flow through banks of cylinders and other related geometries will be reviewed.

2.1 Traditional Approaches to Flow through Porous Media

The most popluar methods of treating flow through porous media to date have been variations of the empirical law proposed by Darcy [1]. The more successful modifications have been developed by Blake, Kozeny, and Carmen (BKC) [9]. In this section the development of the BKC equation will be presented and its inadequacies when applied to flow through banks of cylinders of viscoelastic fluids reviewed.

The BKC equation has been generally accepted as inadequate to model viscoelastic flow in porous media. However, the predictions of the BKC equation for viscoelastic fluids have been used as a measure of the deviation of viscoelastic flow behavior from Newtonian flow behavior. Therefore, it is necessary to present the BKC

equation so that useful discussion concerning the experimental studies of viscoelastic flow in porous media may be reviewed.

2.1.1 Blake-Kozeny-Carmen Equation

The BKC equation uses Darcy's law as a starting point. Darcy [1] experimentally found that the flow rate of gases through a bed of spheres was proportional to the pressure drop:

$$q = K\frac{\Delta P}{L}, \tag{2.1}$$

where K is the constant of proportionality representing the flow resistance, q is the volumetric flow rate, and ΔP/L is the pressure drop per unit length. Kozeny proposed a capillary model which approximated a porous media by a bundle of tubes with the same average radius and a tortuous path [9]. Kozeny modified the equation for Poiseuille flow in two ways. First he replaced the radius with a hydraulic radius defined as the ratio of capillary area perpendicular to flow to the wetted perimeter of the capillary. Second, he introduced the concept of effective length ,L_e, which accounts for the tortuosity of the path. The resulting equation is

$$u = \frac{r_h^2}{K_o \mu}\frac{\Delta P}{L_e}, \tag{2.2}$$

where u is the average velocity, r_h is the mean hydraulic radius, and K_o is a shape factor related to the mean hydraulic radius. The mean hydraulic radius for a tube with a circular cross section is R/2. Therefore, the shape factor necessary for this tube is K_o=2. Kozeny also corrected the velocity in terms of porosity. The velocity in a porous media will be higher than that of a media with porosity=1. He suggested a relationship of the form

$$q = (1 - v_s)u, \tag{2.3}$$

where v_S is the sphere volume fraction. Eq. 2.3 is referred to as the Dupuit-Forchheimer assumption [10]. For spherical particles, the mean hydraulic radius may be written as

$$r_h = \frac{r_s}{3}\left(\frac{1 - v_s}{v_s}\right). \tag{2.4}$$

When Eqs. 2.3 to 2.4 are then substituted into Eq. 2.2 the following results:

$$q = \frac{r_s^2}{9K_o K_1 \mu}\frac{(1 - v_s)^3}{v_s^2}\frac{\Delta P}{L}. \tag{2.5}$$

Carmen introduced another parameter, K1, to this equation to account for tortuosity [12] to give

$$qK_1 = (1 - v_s)u. \tag{2.6}$$

Inclusion of Eq. 2.6 into Eq. 2.5 yields the familiar BKC equation which is the most widely used pressure drop-flow rate relationship for Newtonian fluids

$$q = \frac{r_s^2}{9K_o K_1^2 \mu}\frac{(1 - v_s)^3}{v_s^2}\frac{\Delta P}{L} = \frac{S}{\mu}\frac{\Delta P}{L}, \tag{2.7}$$

where S is the permeability. The product $K_o K^2_1$ is referred to as the Kozeny constant and has been found to be equal to 5 by several investigators [10-15].

Flow of Newtonian fluids through beds of spheres is empirically well described by Eq. 2.7 [2]. In Fig. 2.2, the experimental results of several researchers are plotted as friction factor versus Reynolds number. The friction factors calculated by the BKC equation agree well with the experiments below Reynolds numbers of about 3.

The BKC equation applies only to laminar flow. This is a direct result of the derivation of the velocity being Poiseulle flow. Blake defined an appropriate Reynolds number for flow through a bed of spheres, and using the data of many researchers

determined that the BKC equation was valid up to Re~3, using the Reynolds number in Eq. 2.8 [11]. He defined the Reynolds number to be

$$\mathrm{Re} = \frac{d_s \rho q}{\mu v_s}, \tag{2.8}$$

where d_S is the sphere diameter in the bed, ρ is the density, and v_S is the solid volume fraction of the bed of spheres. The fluid models used for turbulent flow will not be reviewed here since it is rarely encountered in processes involving thermoplastic melts.

It is customary to express the resistance to the flow offered by a particular geometry in terms of the friction factor, f. Analagous to flow through a tube in which f is correlated to Re, one can define f and Re as follows:

$$\begin{aligned} f &= \frac{\Delta P}{\rho u^2}\frac{r}{L}\frac{\varepsilon^3}{(1-\varepsilon)} \\ \mathrm{Re} &= \frac{ur\rho}{4k\mu(1-\varepsilon)} \\ f \cdot \mathrm{Re} &= 1 \end{aligned}, \tag{2.9}$$

where ε is the porosity.

2.1.2 Anisotropic Porous Media

The development of the BKC equation reviewed here involves the assumption that the geometry being modeled is isotropic, or the permeability, K, is the same in all directions. This assumption is valid in a bed of spheres of equal size. However the geometry of a bundle of fibers is inherently anisotropic if the fiber axes lie preferentially in one direction such as shown in Fig 2.2. The BKC equation may be extended to bundles of fibers by modifying the hydraulic radius and defining S as a second order tensor [10]. The mean hydraulic radius may be defined as

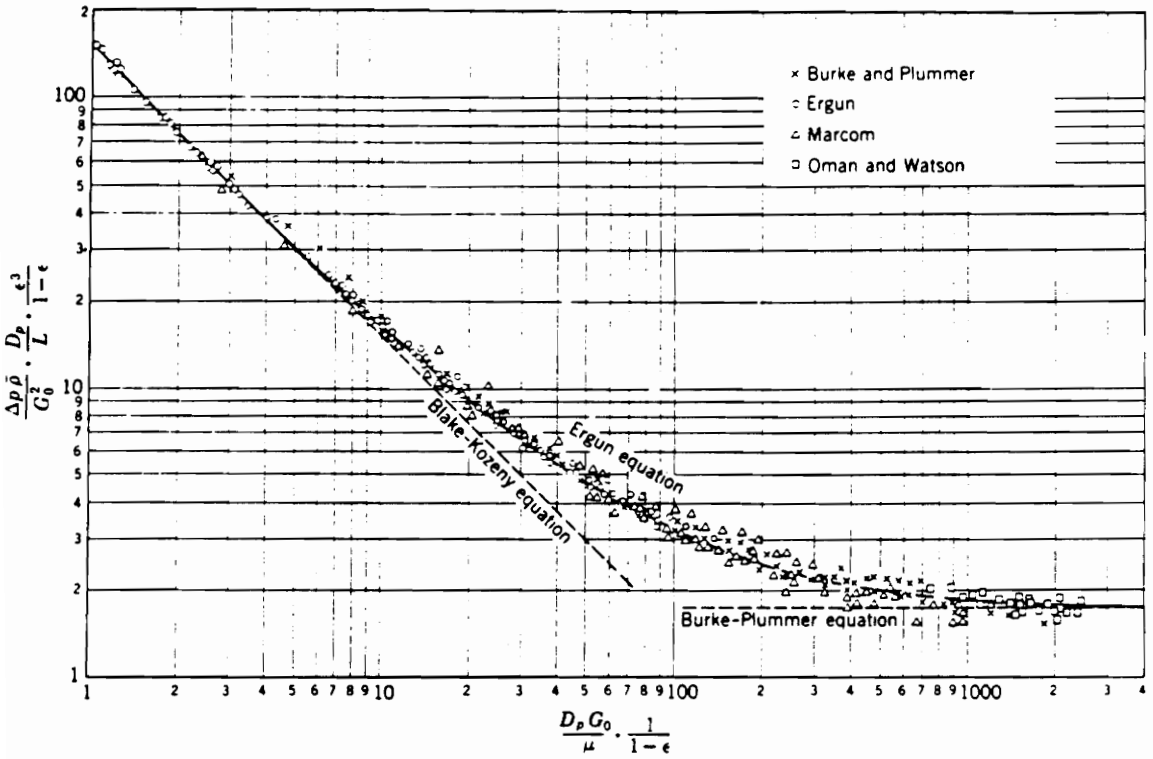

Figure 2.1. Experimental and predicted friction factor versus Re as measured by several investigators [9].

$$r_h = \frac{r_f}{2}\frac{1-v_f}{v_f}, \tag{2.10}$$

where r_f is the fiber radius and v_f is the fiber volume fraction. The BKC equation then becomes

$$q = \frac{r_f^2}{4K_o K_1^2 \mu}\frac{\left(1-v_f\right)^3}{v_f^2}\frac{\Delta P}{L}. \tag{2.11}$$

In order to address the anisotropy of the porous media, Eq. 2.1 has been generalized to the following form [10]

$$\underline{q} = -\frac{\underline{\underline{S}}}{\mu}\nabla P, \tag{2.12}$$

where q is a vector respresenting the superficial velocity component in a each direction and S is a second order symmetric tensor. By choosing a coordinate system which coincides with the principle flow direction, S may be written as [10]

$$\underline{\underline{S}} = \frac{r_f^2}{4}\frac{\left(1-v_f\right)^3}{v_f^2}\begin{bmatrix} \frac{1}{\left(K_o K_1^2\right)_1} & 0 & 0 \\ 0 & \frac{1}{\left(K_o K_1^2\right)_2} & 0 \\ 0 & 0 & \frac{1}{\left(K_o K_1^2\right)_3} \end{bmatrix}, \tag{2.13}$$

where $(K_o K_1)_i$ is the permeability in the i direction. It has been shown that the permeability in any direction may be calculated from the principal permeabilities [16]. For the two dimensional case of fibers arranged in one direction

$$\frac{1}{S} = \frac{\cos^2 a}{S_{11}} + \frac{\cos^2 b}{S_{22}}, \tag{2.14}$$

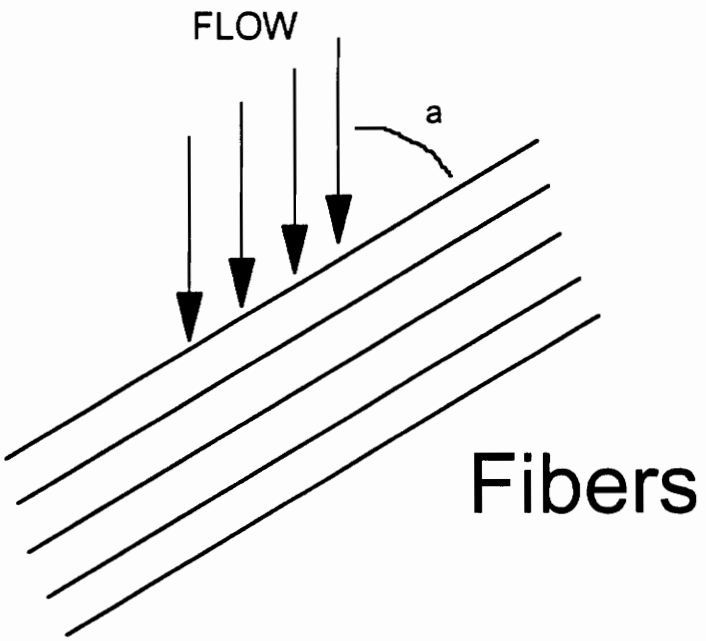

Figure 2.2. Geometry of aligned bed of fibers; a and b are the angles between the velocity vector and the principle permeabilities.

where S_{ii} are the principal permeabilities and a and b are the angles between the velocity vector and the corresponding principal permeability.

2.1.3 Derivation of the BKC Equation for Shear Thinning Fluids

Khomami and coworkers [17] have summarized the conditions where the assumption of a constant capillary diameter are not appropriate: very low porosity, very high porosity, adsorption and surface effects, blocked paths, elongational strains, and pore nonuniformities. Of interest here is the case of very low porosity and extensional strains which are occur in flow through ideal arrays of fibers.

The BKC equation may be modified by deriving eq. 2, the velocity in a tube, for a power law fluid instead of Newtonian fluid. The results of this modification are summarized in ref. 9 and 18. The resulting dimensionless parameters f and Re are

$$f^* = \left(\frac{\Delta \mathrm{Pr}}{\rho u^2 L}\right)^{\frac{1}{n}} \frac{\varepsilon^{2+\frac{1}{n}}}{(1-\varepsilon)^{\frac{1}{n}}}$$

$$\mathrm{Re}^* = \frac{u^{\frac{2}{n}-1} r \rho^{\frac{1}{n}}}{(1-\varepsilon)} \frac{n}{(3n+1)} \left(\frac{1}{mk^*}\right)^{\frac{1}{n}} \qquad (2.15)$$

where n is the power law index, m the consistency, and k* the modified Kozeny constant. Again the product f*Re*=1.

2.2 Experimental Studies

Researchers who performed the first studies of flow of viscoelastic fluids through banks of cylinders and other porous media found that the predicted pressure drops calculated by the BKC equation were significantly lower than the measured experimental pressure drops [5,17,19,20,21]. This increased resistance to flow was attributed to "elastic effects," as it is still often referred to. The physical origin of the increased resistance to flow is now believed to be a result of the extensional flow behavior of viscoelastic fluids although extensional effects are still often ignored in rheological characterization and numerical simulations [5,21].

The bulk of experiments performed on the flow of viscoelastic fluids through banks of cylinders have used polymer solutions. Polymer solutions are experimentally easier to work with than polymer melts because experiments may be performed at room temperature. In addition, the Boger fluids, M1 fluids, and A1 fluids have a constant viscosity and allow the elasticity to be varied. As opposed to fitting a model to fluid behavior, these fluids are fitted to the model. This has allowed simulations to be performed with Maxwell and Oldroyd type constitutive equations which are believed to be numerically less demanding than constitutive equations which predict more complex polymeric behavior such as shear thinning and extensional viscosity.

The rheological characterization of the viscoelastic fluids examined in flow through complex geometries generally involves the measurement of the shear viscosity and the extensional viscosity. The shear viscosity is easily measured for both polymer solutions and polymer melts. However, the extensional behavior is more difficult to measure. Producing a homogenious flow field has been accomplished for high viscosity polymer melts, but not polymer solutions. Extensional viscosity

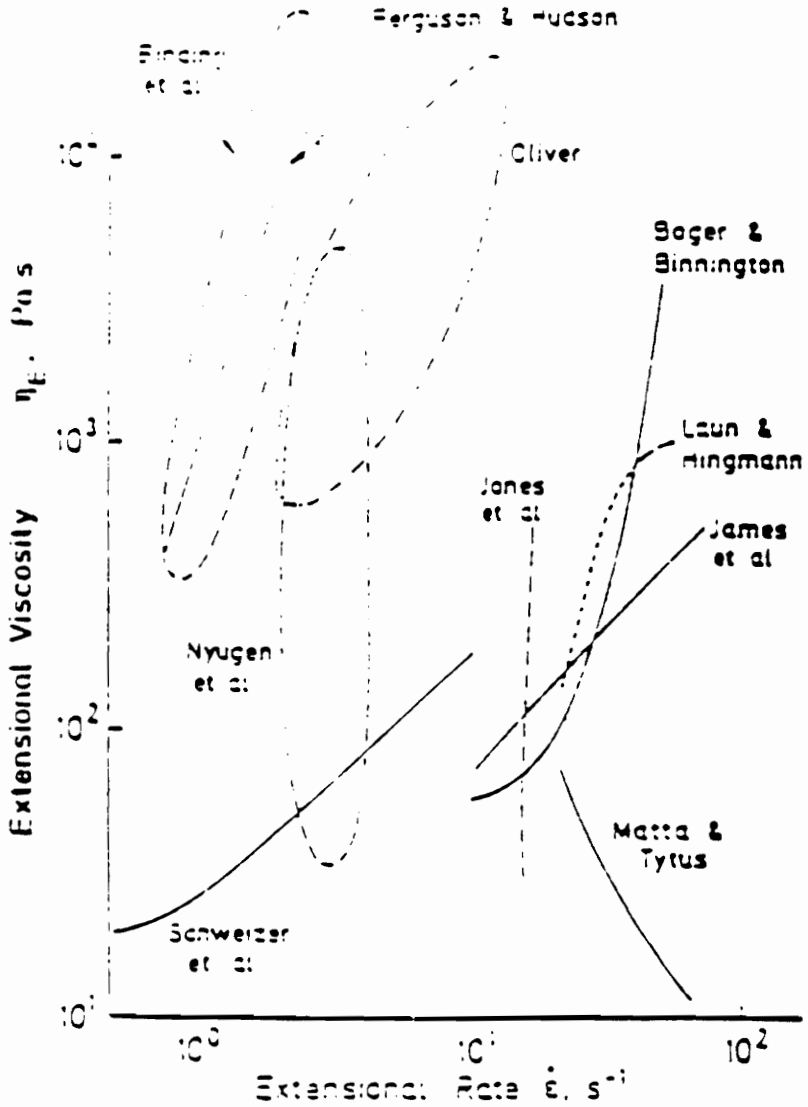

Fig. 2.3. Experimental measurements of the extensional viscosity performed by deveral investigators of the M1 fluid (similar to Boger Fluids) [32].

measurements by several researchers are shown in Fig. 2.3 for a single fluid, the M1 fluid. The large differences between measurements was attributed to nonhomogeneous flow fields. When one is attempting to analyze flow behavior in geometries where extensional behavior is expected to play a major role, it is desireable to know the extensional behavior of the fluid. Polymer solutions clearly do fall into this category.

The flow geometry of a bank of cylinders consists of converging and diverging flow regions where extensional strain rates may be very high. Thus extensional behavior would be expected to be a major factor in the flow of viscoelastic fluids through banks of cylinders. The role of extensional viscosity in the flow through complex geometries has been examined by several researchers. Durst et. al. examined the effect of extensional behavior on the flow of polyacrylamide solutions through beds of spheres and modified the BKC equation to incorporate the extensional effects into the equation [21]. The modified BKC equation was derived from theoretical principles but empirical fits of the pressure drop versus flow rate data were required for quantitative fits of the pressure drop flow rate data.

Jayaraman and coworkers [5] and Khomami and coworkers [18] have examined the effects of viscoelasticity on flow of fluids transverse to square and hexagonal arrays of cylinders. These researchers were aware that the modified BKC eq. is inadequate and have utilized this equation mainly to determine the onset of elastic effects (all of the authors termed the deviation from the BKC equation as "elastic effects" although the precise nature of these deviations has only been hypothesized). Jayaraman and coworkers [5] devised a "cross flow" apparatus with two different types of cylinder packing: square and circular (hexagonal) to examine the effects of polymer extensibility. Three different types of fluids were utilized: Newtonain, Boger Fluids, and viscoelastic shear thinning solutions. A fiber spinning

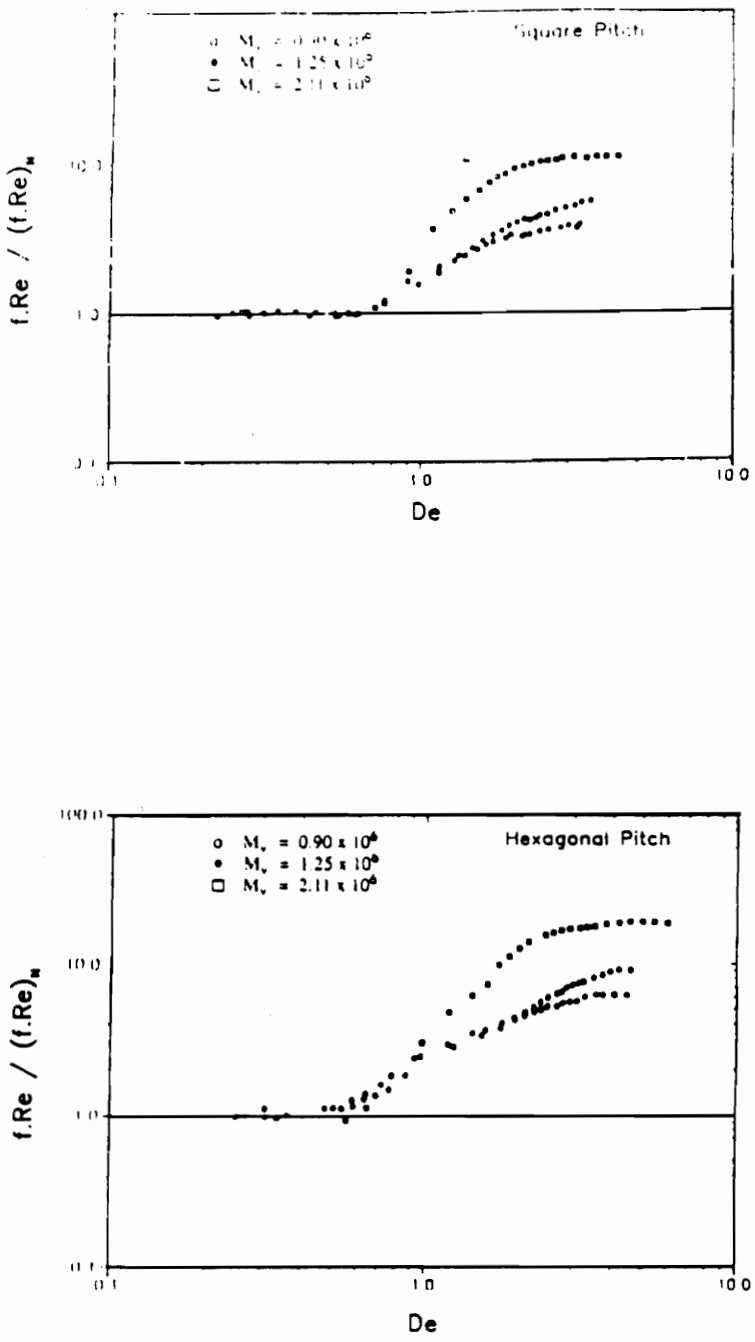

Fig. 2.4. Flow resistance of Boger fluids in square and hexagonal arrays of cylinders [5].

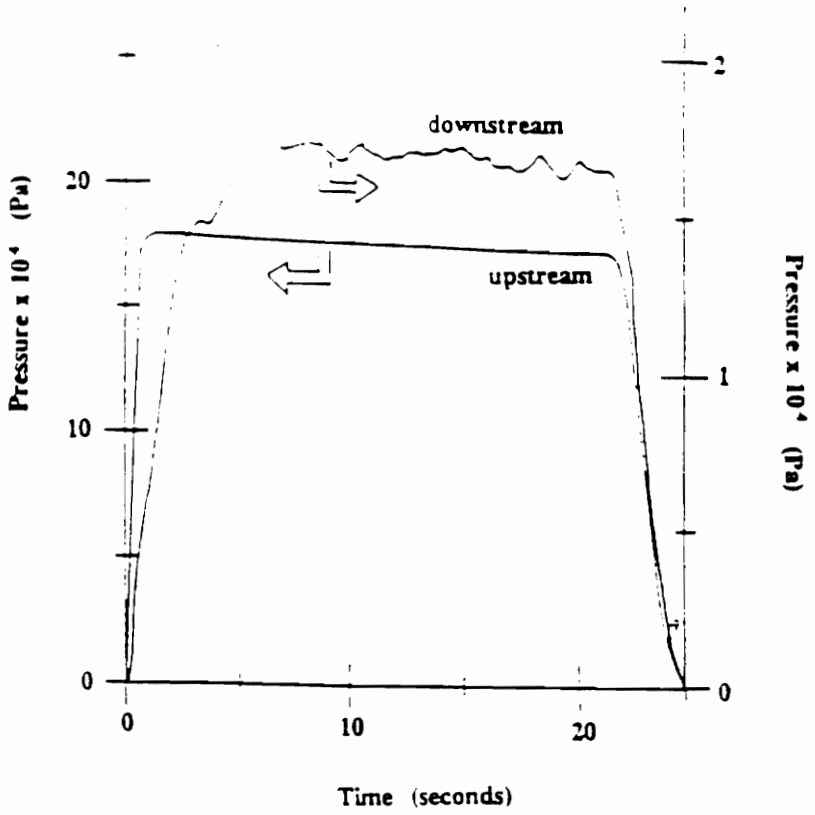

Fig. 2.5. Upstream and downstream pressure a Boger fluid flowing through a square array of cylinders [5].

apparatus was used to determine the extensional flow characteristics and the authors claimed that all of the fluids were well characterized. This is questionable due to the results shown in section 2.1 for solution extensional rheology. Fig. 2.4 shows results for the Boger fluids in both a square array and hexagonal array of cylinders. The results are plotted as a normalized f.Re product versus the Deborah number. The Kozeny constant was determined experimentally and then substituted back into f and then the product f.Re was normalized by dividing by the f.Re product for the Newtonian case. This type of analysis will result in the normalized product being equal to 1 for flows which do not deviate from Newtonian behavior. The Deborah number was defined by the equation

$$De = \lambda_1 \frac{\alpha v_o}{a}, \qquad (2.16)$$

where a is the cylinder radius, λ_1 is the fluid relaxation time, and α is a geometric factor. The geometric factor was determined from Stokes flow simulations and is related to the stretch rate of the flow. In Fig. 2.4 it is shown that the product of f and Re deviates from Newtonain flow at about De~1 for both geometric arrays when this definition of De is used. It is also interesting to note that the resistance to flow was higher for the hexagonal array of cylinders despite a more efficient packing associated with this geometry (the shortest distance between adjacent fibers is smaller for square arrays than hexagonal arrays) for the same volume fraction.

In Fig. 2.5 is shown a trace of the pressure drop versus time data obtained for a Boger fluid in experiments performed by Jayaraman et. al. The high frequency oscillations in the downstream pressure indicate the presence of a flow instability. The origin of the instability can only be speculated since only the pressure drop and flow rate were known for these experiments. However, it is important to realize that the fluid used in this experiment is a solution of a high molecular weight polymer only

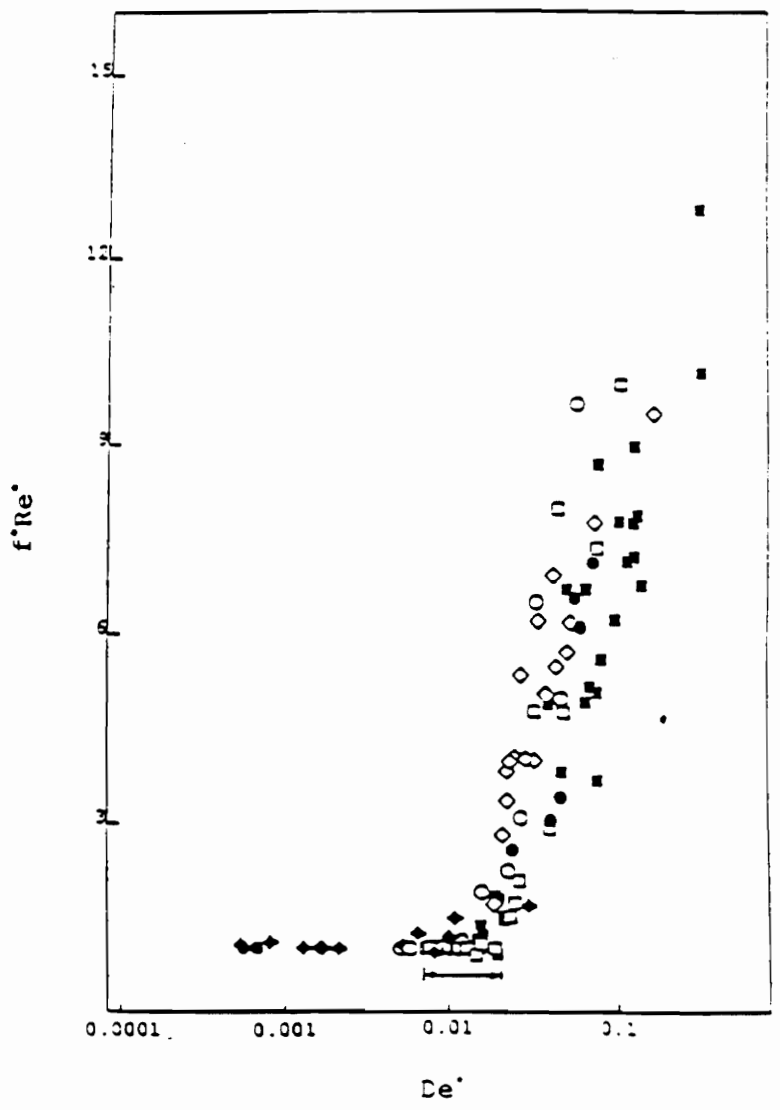

Fig. 2.6. Flow resistance of a Boger fluid flowing through a square array of cylinders [18].

about 7 degrees Celcius above the theta temperature. A strong flow field, such as the extensional flows generated in their apparatus may result in stress induced phase separation.

Khomami and coworkers [18] utilized a series of fluids similar to those of Jayaraman and coworkers. Their results are qualitatively similar to those of Jayaraman et. al. [5]. However, the Deborah number was calculated using a definition developed by Dunlap and Leal [22]. Dunlap and Leal proposed an alternative to the conventional Deborah number which more accurately describes the strain on the polymer molecules in dilute solutions. This approach was only meant for dilute solutions and results in a dimensionless parameter $\theta\varepsilon_V\sqrt{\lambda}$, where θ is the relaxation time, and ε_V and λ are related to the velocity field [23]. In Fig. 2.6 is shown a representative result of their data. The increase in flow resistance began at a dimensionless parameter of 0.01 for all of their viscoelastic fluids.

A final note in this area comes from the investigation previously discussed by Durst et. al. [21]. Durst states that "the large discrepancy between theory and experiments is due to only taking one part of the relevant shear strain into account and also due to neglecting the pressure loss caused by the elongation strain." The inherent assumptions of the BKC equation do not permit an inclusion of elongational parameters in any way. Therefore, new approaches are needed to model viscoelastic flow through medias with low porosity.

2.3 Numerical Studies

The equations governing the 2D flow of viscoelastic fluids generally consists of the continuity equation, momentum equation, and a constitutive equation in two dimensions. These equations are very nonlinear [24] and have mixed elliptic/hyperbolic characteristics [25]. The complex nature of these equations leads to difficulties in obtaining accurate solutions, numerically or analytically. Traditional finite element methods are inadequate for solving these equations for De>1. Numerical methods capable of handling the numerical challenges presented by the viscoelastic flow problem are necessary if an accurate solution is to be obtained.

There are several different approaches that have been taken for numerically solving the flow of a viscoelastic fluid between cylinders. Souvaliotis and Beris have implemented domain decomposition spectral techniques which have already been successful in Newtonian fluid mechanics problems [8]. These spectral techniques may be used in either collocation or a weighted residual method. Fully spectral methods require that the computational domain be mapped onto a rectangle without producing any singularitites, thus eliminating most complex geometries. Domain decomposition overcomes this limitation by splitting the computational domain into smaller, simpler domains. This techniques allows some of the flexibility associated with traditional finite element methods

Talwar and Khomami have implemented higher order techniques through the *p* version of the finite element method [7]. The *p* version posesses many advatages in that complex geometries may be used, and computational flexibilty exists since the polynomial order is allowed to fluctuate in the intervariable (u,v,p,..) and interelement

(flow direction) sense. Talwar and Khomami have only applied the higher order methods to smooth geometries (i.e. without singularities).

The final numerical approach which has been applied to the flow of viscoelastic fluids though banks of cylinders is the artificial diffusivity method introduced by Marchal and Crochet [26]. This method is based on streamline upwinding (SU) originally proposed by Brooks and Hughs for high Reynolds number Newtonian flow problems where convection dominates [27]. The SU method involves biasing of the weighting functions upstream along the streamlines. Marchal and Crochet implemented the SU method by discretizing the constitutive equation in the Galerkin sense, and applying SU to only the convective terms.

While the SU method of Marchal and Crochet is stable and convergent, the accuracy of the method has been a source of controversy (as most upwinding methods have been). Tanner and Jin analyzed the SU method along with the Galerkin and SUPG methods in a 1-dimensional case in order to determine the accuracy of the SU method [28]. The SU method was the least accurate of the three methods. Tanner concluded that the SU method are unlikely to be as accurate as higher order methods. However, the SU method allows solutions which are not attainable with all other methods to date. Therefore more work is necessary to determine the accuracy of the SU mehod.

The geometry associated with flow transverse to banks of cylinders has received recent attention from the standpoint of computing the pressure drop for flow between two cylinders, as shown in Fig. 2.7, and applying this pressure drop additively throughout the flow domain [7,8]. The focus of the experiments [29] and numerical work [7,8,29] was entirely on Newtonian fluids and Boger fluids. Georgiou et. al [29] used an Oldroyd model to predict the flow resistance and Fig. 2.8 shows the

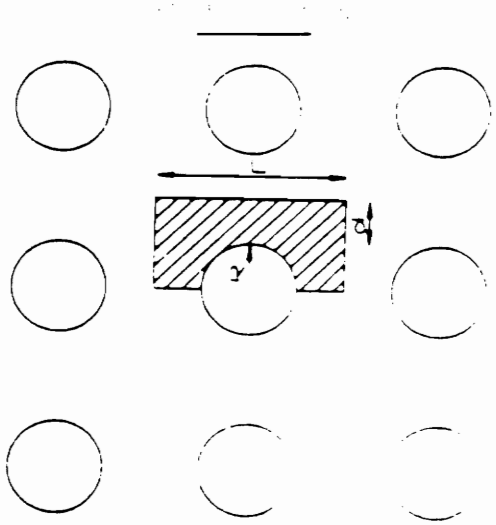

Fig. 2.7. **Domain of computations for calculation of cell flow resistance in a bank of cylinders.**

qualitative agreement. The flow cell and geometry used are shown in Fig. 2.9 and it should be noted that the flow did not approximate a two dimensional flow. The focus of Talwar and Khomami [7] and Souvaliotis and Beris [87] was to develop higher order finite elements and spectral methods, respectively. The predicted flow resistances of Souvaliotis and Beris [8] were compared only to other numerical simulations and were not found to be in agreement. Talwar and Khomami [7] compared the flow resistance predicted by an upper convected Maxwell fluid and Oldroyd B fluid to experiments performed using Boger fluids [64,66]. The results are shown in Fig. 2.10. The flow resistance, fRe, computed by Talwar et. al. [7] and Souvaliotis et. al. [8] show a decreasing flow resistance with increasing De, or equivalently We. This is in contrast to experimental results as indicated in Fig. 2.10.

In summary, the prediction of pressure drops or flow resistances of viscoelastic fluids has not at present been predicted a priori as would be desired for industrial applications. More experimental data for simple geometries involving cylinders is needed, especially with polymer melts. The issue which was neglected by Talwar and Khomami as well as Souvaliotis and Beris is the choice of constitutive equation. The convected Maxwell model and Oldroyd-B model were used in all computations. The behavior of these constitutive equations in uniaxial extensional flow is well known: the stresses computed by the Maxwell model diverge to infinity when the extension rate is 1/2De; the stress computed by the Oldroyd-B model increase linearly with strain rate. Both of these predictions are unrealistic with respect to polymeric liquids, although the exact nature of the extensional behavior of polymer solutions in extensional flow is not known.

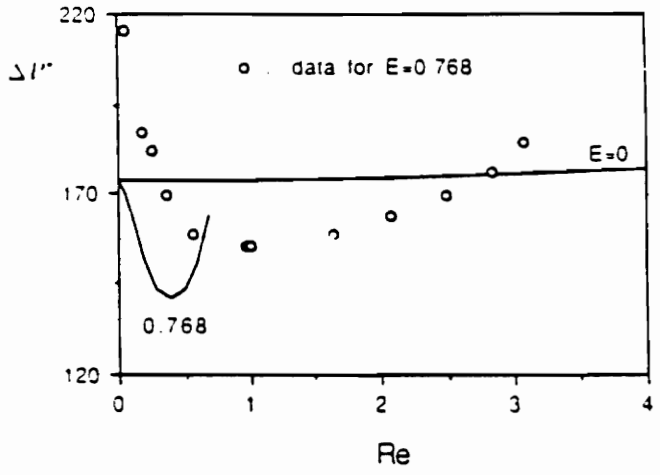

Fig. 2.8. Experimental and computed pressure drop (ΔP) versus Reynolds number (Re) of a Boger fluid flowing through a staggered series of cylinders, shown in Fig. 2.9 [29].

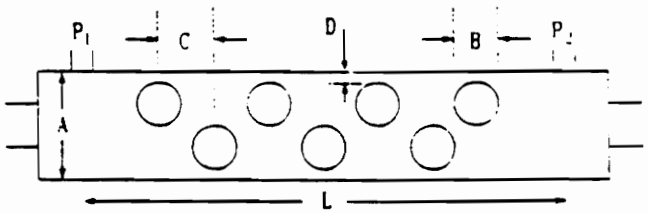

Dimensions of model geometries: (mm)

Geometry	A	B	C	D	L
#1	23	12.5	33.75	3.5	326
#2	23	12.5	33.75	3.5	326

Fig. 2.9. Experimental geometry used by Crochet et. al. [29].

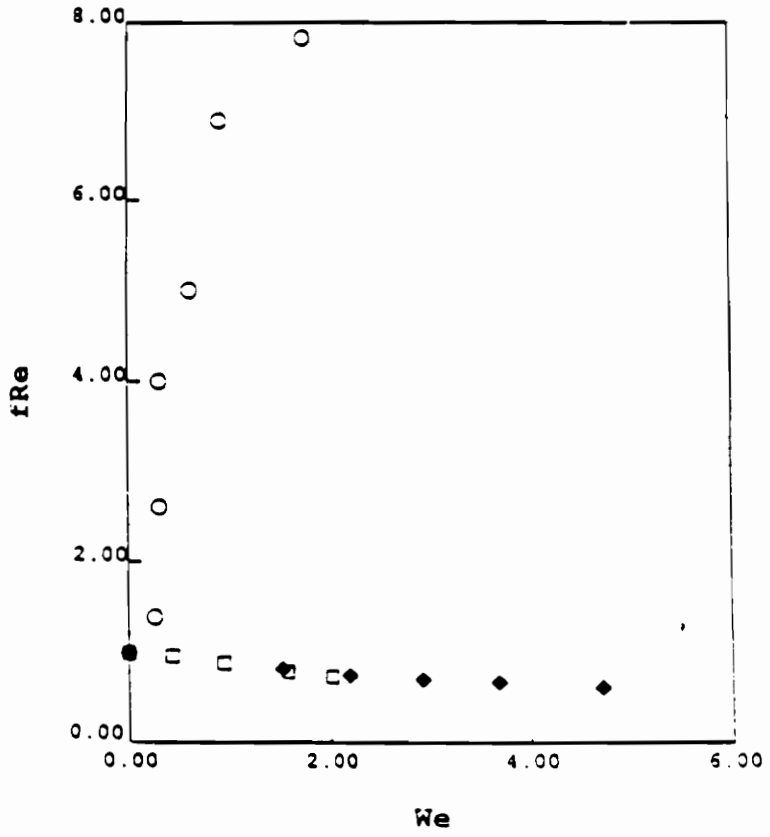

Fig. 2.10. Comparison of predicted and experimental flow resistance (fRe) versus Weissenberg number (We) of a Boger fluid through a bank of cylinders [7]. The open circles are experimental values and the diamonds and squares are computed values.

2.4 Flow Geometries Related to Flow through Porous Media

There are flow problems which have already been extensively studied which are related to flow through porous media. As previously discussed, the characteristic converging and diverging nature of flow through banks of cylinders may be captured in other geometries. For example, one of the first geometries where extensional flow was found to be important was the entry flow problem. In this section, the entry flow problem and the periodically constricted tube will be briefly reviewed with an emphasis on the aspects important to flow through banks of cylinders.

2.4.1 The Entry Flow Poroblem

Flow of fluids through porous media with small void fractions, such as flow through composite fiber tows, undergo abrupt contractions and expansions. The flow problem of a viscoelastic fluid flowing through a sudden contraction may be the most experimentally and numerically studied problem in viscoelastic fluid mechanics. Both the experimental and numerical aspects of this problem have been reviewed by White, Gotsis, and Baird [30]. The geometry of the problem is shown in Fig. 2.11. The vorticies present in the flow of some viscoelastic fluids at very low Reynolds numbers, where inertial effects are nonexistent, are also shown qualitatively in Fig. 2.11, and in Fig. 2.12 is shown experimentally observed vortices for LDPE. The most significant result given by White, et. al. [30] is that not all viscoelastic fluids form vortices when flowing through an abrupt contraction. They hypothesized that vortices form only for strain hardening fluids in a contraction. Despite the depth of research into the entry flow problem, there are still some uncertainties involving the formation of vortices by

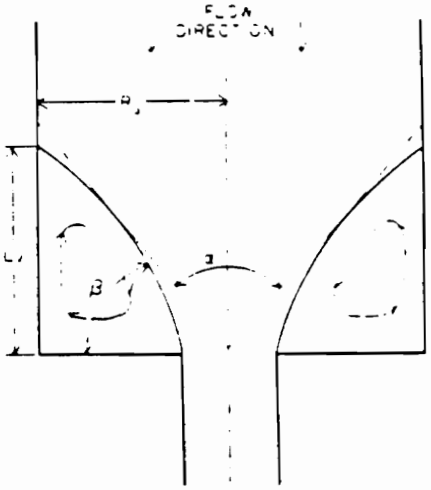

Fig. 2.11. Schematic of viscoelastic flow through an abrupt contraction [7]

Fig. 2.12. Experimentally observed vortices in LDPE flowing through an abrupt contraction [30].

some fluid in axisymmetric contractions while not in planar contractions. White et. al. also noted that much of the work in this area has been performed using the so called Boger fluids, which may not exhibit flow behavior common to most viscoelastic fluids. It was suggested that more experiments should be performed using polymer melts.

McKinley et. al. [32] have studied the flow of Boger fluids through an axisymmetric contraction using laser dopplerimetry. The advantage of laser dopplerimetry over particle tracing and flow birefringence is the acquisition of quantitative data from complex flows. Birefringence only results in quantitative data when the optical retardation is known [33]. The retardation is rarely determined in complex flows. The most important result of their work was that at De of about 0.8, all three of the velocity components exhibited time dependent oscillations. In addition the velocities showed behavior characteristic of chaotic dynamics, such as period doubling. This behavior may be only representative of Boger fluids. Boger fluids have been shown to exhibit secondary flows in cone and plate rheometer after an initial period of steady flow [34]. In contrast, polyethylene has been shown to exhibit stable flow in a cone and plate rheometers for more than 200 hours after which the experiment was terminated [35].

2.4.2 The Periodically Constricted Tube (PCT)

Another flow geometry which may be related to flow between cylinders is the periodically constricted tube, or undulating tube [36] shown in Fig. 2.13. Most numerical simulations involving this type of geometry were performed using Oldroyd type models and examined the effects of fluid elasticity on flow resistance [37-41]. No increase in flow resistance has been calculated. Deiber and Schowalter performed

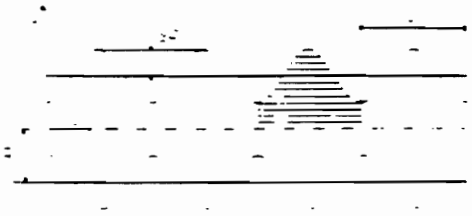

Fig. 2.13. Flow geometry of the periodically constricted tube. The shaded area shows the computational domain.

experiments in this geometry with solutions of aqueous polyacrylamide [36]. An increase in flow resistance was observed. However, the experiments were performed under inertial flow conditions so the source of the increased flow resistance is uncertain. Pilitsis et. al. [84] simulated the periodically constricted tube using the PTT model without a shear thinning viscosity, the MPTT, and compared their results with the experiments performed by Dieber and Schowalter [78]. The flow resistance was severely under predicted but was closer to the experimental data than the simulations using the Oldroid type fluid performed by other investigators.

2.4.3 Flow Past a Single Cylinder

Flow of a viscoelastic fluid transverse to a single cylinder has received relatively little attention. The research that has been performed on this problem has generally been focused on one of two problems. The first is the issue of whether the streamlines shift upstream or downstream as elasticity of the fluid is increased as is shown schematically in Fig. 2.14. The second area of focus is the experimental observations of anomalous heat transfer and mass transfer when a dilute polymer solution flows past a heated cylinder. All of the analyses performed to date have utilized polymer solutions. The flow of polymer melts past a cylinder has not been analyzed. These topics will be reviewed in this section in addition to theoretical analyses which have attempted to explain the anomalous transport properties encountered when viscoelastic fluids flow past a cylinder.

The investigations of the flow of viscoelastic fluids past a cylinder generally utilize a geometry shown in Fig. 2.15. Ultman and Denn analyzed the flow of a 1.7% solution of CMC-7H in water past a cylinder [43]. The streamlines were visualized by

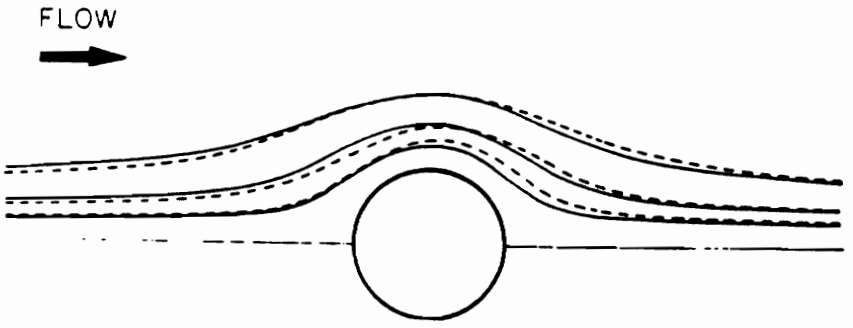

(a)

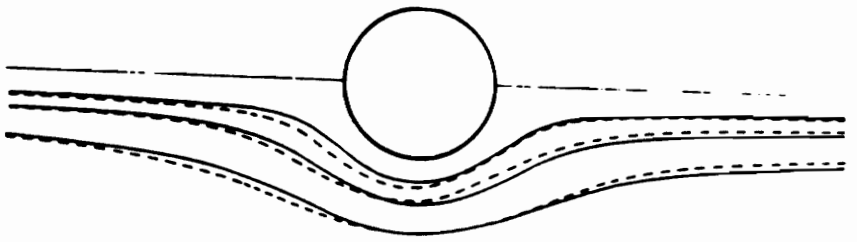

(b)

Fig. 2.14. Schematic of streamlines shifting upstream and downstream for flow past a cylinder: (a) De<1; (b) De>1.

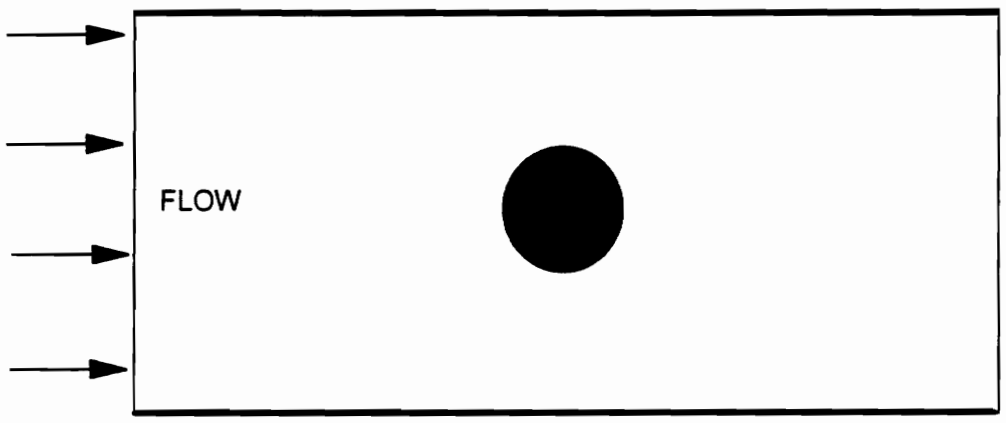

Fig. 2.15. Schematic of typical experimental geometry used for determining streamlines for the flow of a fluid past a cylinder.

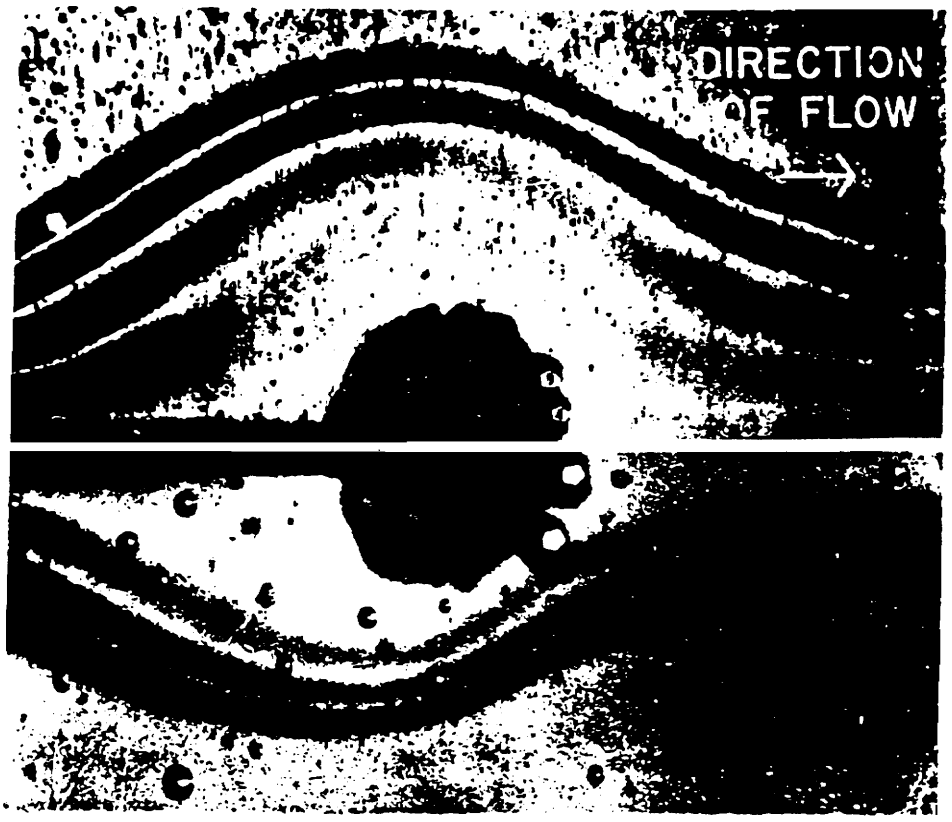

Fig. 2.16. Experimental streamlines for a Newtonain fluid (corn syrup, top) and a polymer solution (CMC-7H, bottom) [43].

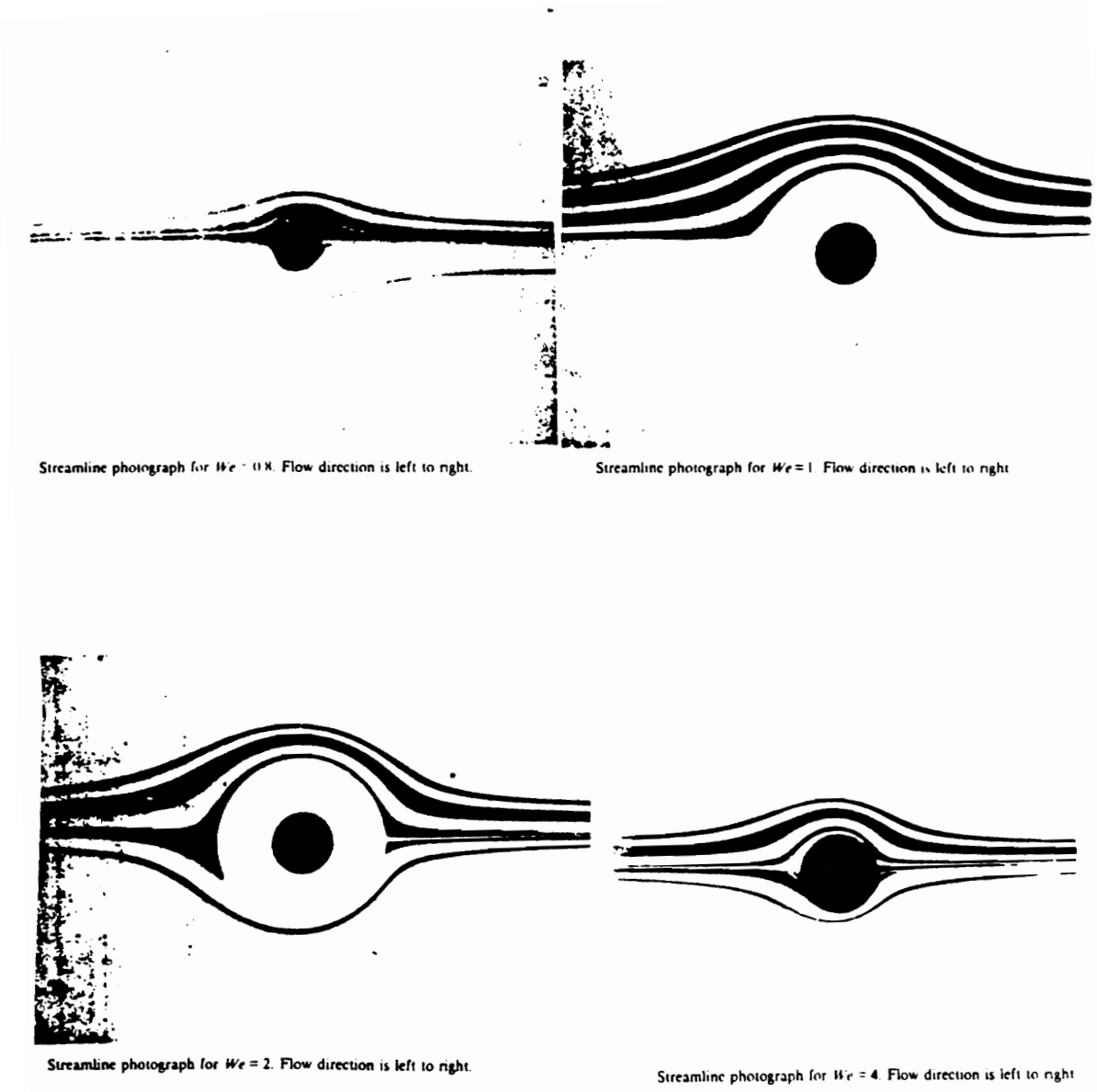

Streamline photograph for $We = 0.8$. Flow direction is left to right.

Streamline photograph for $We = 1$. Flow direction is left to right

Streamline photograph for $We = 2$. Flow direction is left to right.

Streamline photograph for $We = 4$. Flow direction is left to right

Fig. 2.17. Streamline photographs of the flow of solutions of separan in water [44].

photographing die streaks. The observed upstream shift in the streamlines is shown in Fig. 2.16. The ustream shift in the streamlines is compared to the streamlines observed for a Newtonian fluid, which exhibits no shift in the streamlines. Ultman and Denn did not give an estimated Reynolds number or an elasticity number for the photograph shown in Fig. 2.16. Manero and Mena analyzed the flow of a 0.5% solution of separan in water and solutions of 0.25% and 0.5% separan in a 50-50 mixture of glycerol and water [44]. The results of Manero et al.'s experiments indicate that the streamlines may shift upstream or downstream, depending on the We number. Fig. 2.17 shows that for We less than 1, the streamlines shifted downstream of the cylinder and for We greater than 1, the streamlines shifted upstream of the cylinder. The flow corresponding to We~1 show no shift upstream or downstream.

Dhahir and Walters have examined that flow of a Newtonian fluid which was a mixture of water and maltose syrup, a Boger fluid, an aqueous solution of polyacrylamide, and an aqueous solution of xanthan gum past a cylider in confined flow [45]. Dhahir and Walters obtained both vizualization of the streamlines and force measurements on the cylinder in addition to the direction of rotation of the cylinder when it was allowed to rotate freely. The cylinder could be moved in the vertical direction as shown in Fig. 2.18 to examine the effect of asymmetry of the cylinder in the channel. The effect of extensional viscosity was analyzed by Dhahir and Walters by comparing the flow behavior of the Boger fluids and polyacrylamide solution, which are tension thickening, to the flow behavior of the aqueous xanthan gum solutions, which are tension thinning. A schematic of the experimental apparatus used by Dhahir and Walters is shown in Fig. 2.18 with the observed direction of rotation of the cylinder when viscoelastic fluids flow past the cylinder. The flow patterns given in Ref. 45 are shown in Fig. 2.19. The streamlines of the Newtonian fluid in Fig. 2.19 exhibit

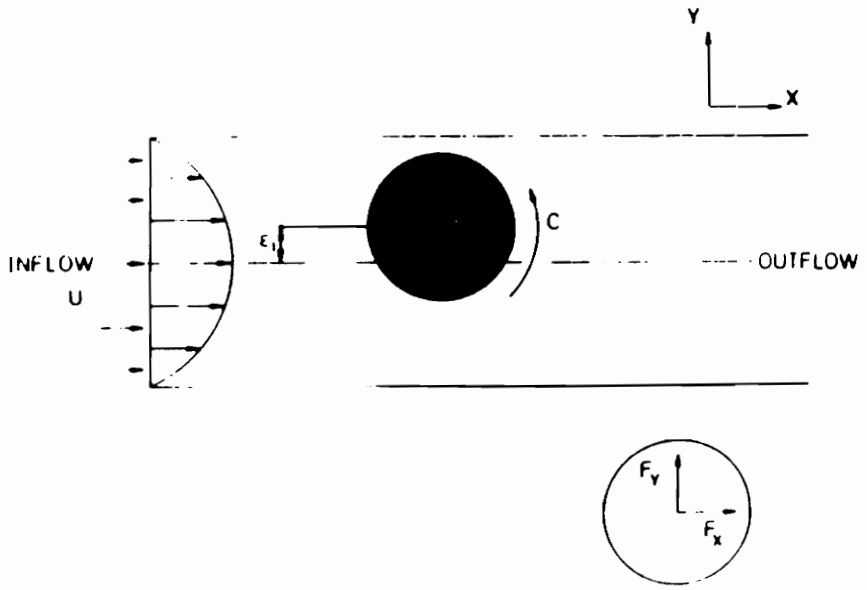

Fig. 2.18. Schematic of experimental apparatus of Dhahir and Walters [45].

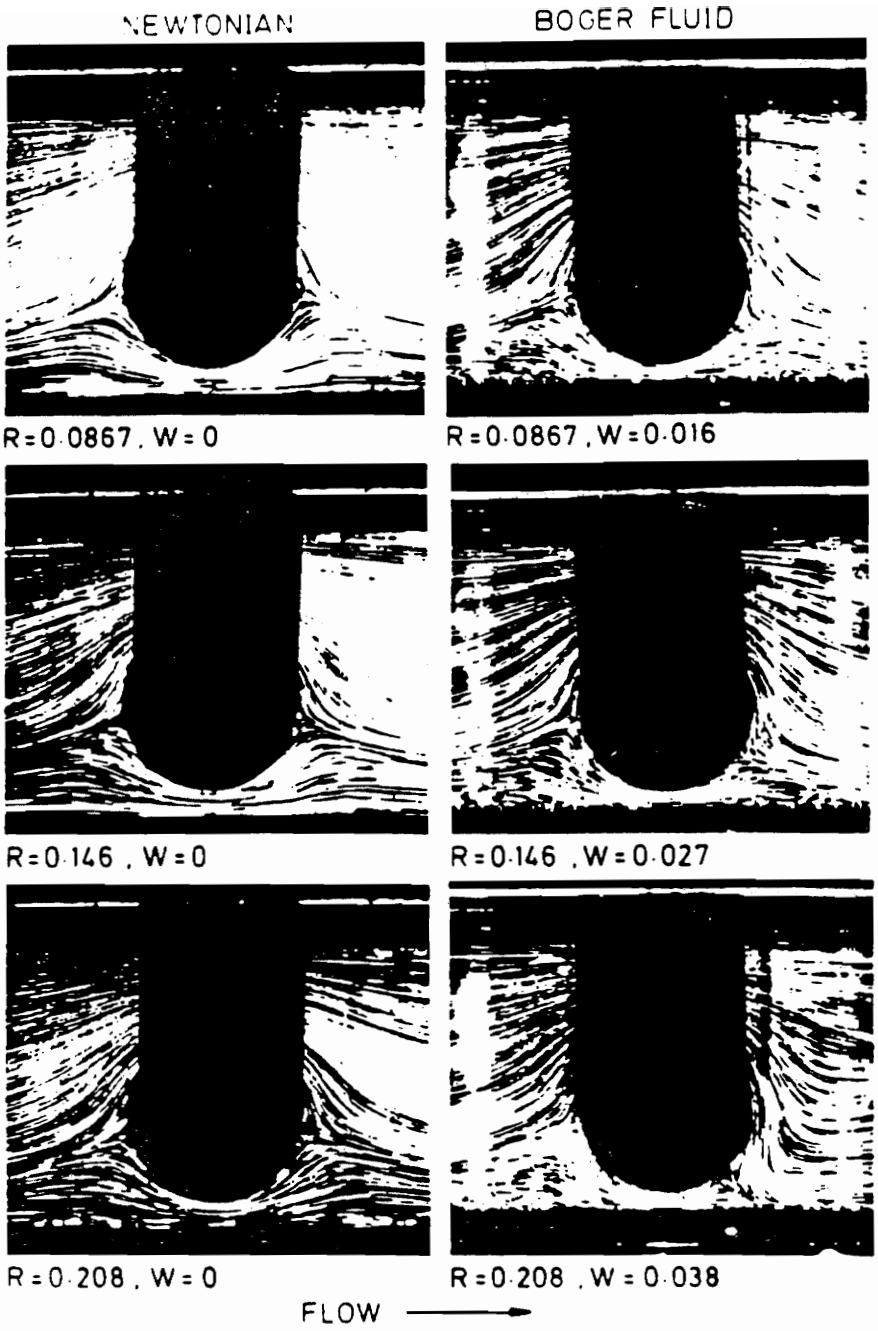

Fig. 2.19. Experimental streamlines for a Newtonian and Boger fluid measured by Dhahir and Walters [45].

virtually no change at Reynolds numbers between 0.0867 and 0.208. The streamlines of the Boger fluid with the same viscosity as the Newtonian fluid in the figure change drastically as We is increased from 0.016 to 0.038. An important finding of their work is that the maximum force on the cylinder for any of the fluids analyzed occurs when the cylinder is at the center of the channel. The force on the fluid decreased as the cylinder was moved away from the centerline. The investigation of Dhahir and Walters examined the flow of viscoelastic fluids at small We, so the upstream shift in streamlines observed by Ultman and Denn [43] and Manero and Mena [44] could not be verified, or the effect of extensional behavior determined.

The characteristics of heat transfer, mass transfer, and the drag coefficient on a cylinder have been shown to become independent of Reynolds number at some critical flow velocity, U_C, when dilute solutions of polyox in water flow past a cylinder. James and Acosta have examined the effect of polyox concentration and Reynolds number on the drag coeffient, C_D [46]. The drag coefficient is a decreasing function of Re for a Newtonian fluid as shown in Fig. 2.20. James and Acosta concluded that the drag coefficients for the polyox solutions become independent of Re at some critical velocity, U_C. James and Gupta have investigated the effect of polyox concentration and the Re of the flow of a polyox solution on the heat transfer from a cylinder [47]. The Nusselt number is

$$Nu = \frac{hd}{k}, \tag{2.17}$$

where d is the diameter of the cylinder, k is the thermal conductivity of the fluid, and h is the average heat transfer coefficient which is defined to be

$$h = \frac{Q}{T_0 - T_\infty}, \tag{2.18}$$

where T_0 is the average temperature of the cylinder, T_∞ is the temperature of the fluid far from the cylinder, and Q is the measured heat flux. Nu was found to be independent of the average fluid velocity at some critical velocity as shown in Fig. 2.21(a). James and Acosta also showed that the critical velocity seemed to be independent of cylinder diamter, d, as shown in Fig. 2.21(b). The heat transfer experiments may be compared to mass transfer experiments of Ambari, Deslouis, and Tribollet [48] which indicates a nearly identical U_c as shown in Fig. 2.22.

Koniuta, Adler, and Piau used laser-doppler anemometry to measure the velocity field of an aqueous polyox solution flowing past a 0.0206cm wire [49]. Their results, replotted by Joseph as dimensionless velocity upstream from the wire versus dimensionless distance from the wire are shown in Fig. 2.23. All of the data except that associated with the smallest flow rate indicate the presence of a stagnant region near the cylinder. The presence of a stagnant region would be consistant with the anomalous heat and mass transport properties.

Theoretical treatments of viscoelastic flow past cylinders have focused on the change of type of the vorticity equation from elliptic to hyperbolic when the fluid velocity exceeds the viscoelastic "mach" number, M, which is defined to be

$$M = \frac{U}{c}, \tag{2.19}$$

where U is the fluid velocity and c is the velocity of vorticity waves in the fluid. Due to the complex nature of viscoelastic constitutive equations, theoretical treatments have only been performed on the Maxwell model. Following the treatment of Joseph [50], the Maxwell model and vorticity equation may be written as

$$\frac{\partial \underline{\underline{\tau}}}{\partial x} + \frac{1}{We}\underline{\underline{\tau}} = A[u(x)] \text{ and} \tag{2.20}$$

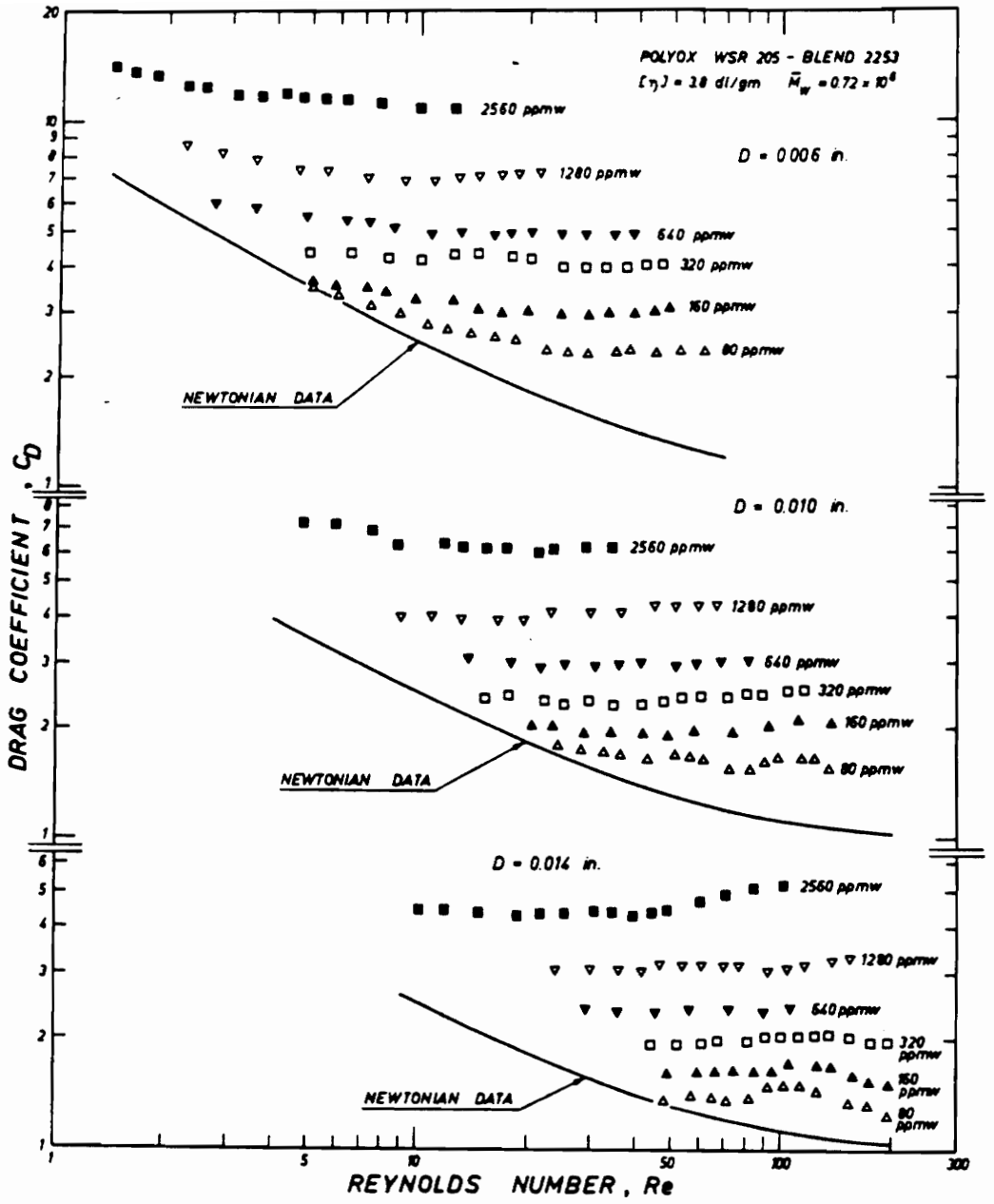

Fig. 2.20. Drag coefficient for various concentrations of polyox in water as a function of Re measured by James and Gupta [47].

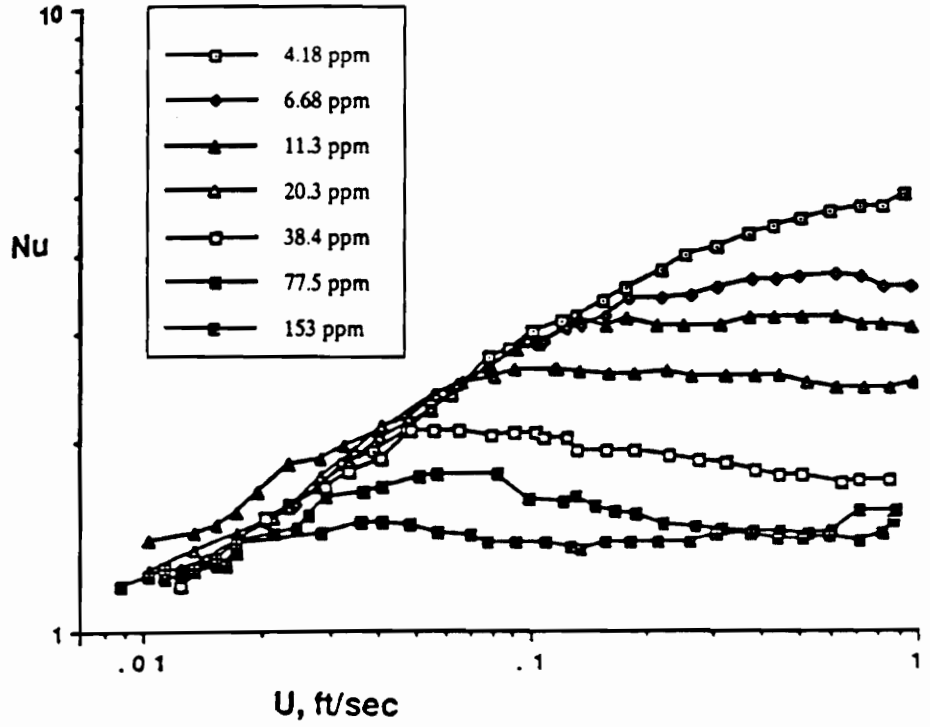

Fig. 2.21. Nu as a function of Re for polyox solutions as measured by James and Acosta [46].

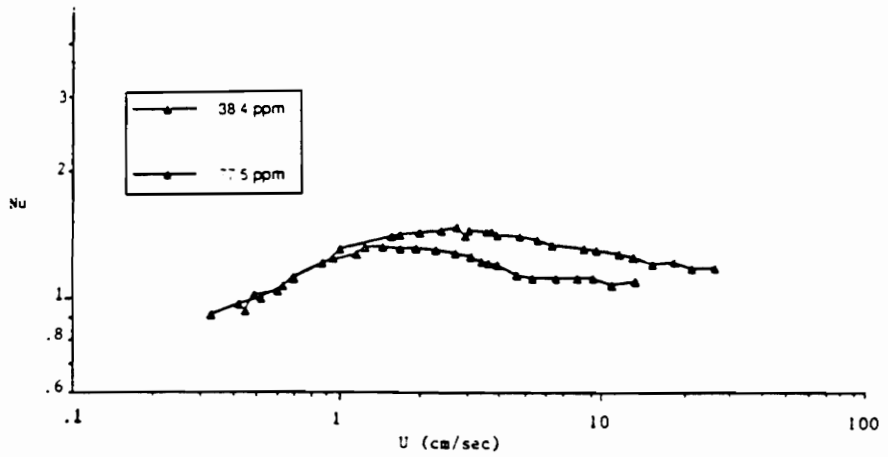

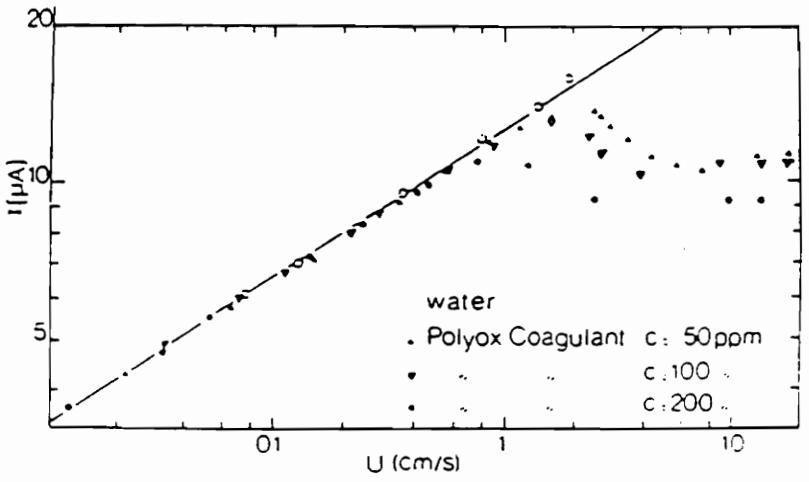

Fig 2.22. Comparison of heat transfer data of James and Acosta [46] to the mass transfer data of Ambari et. al. [48] for a polyox solution [50].

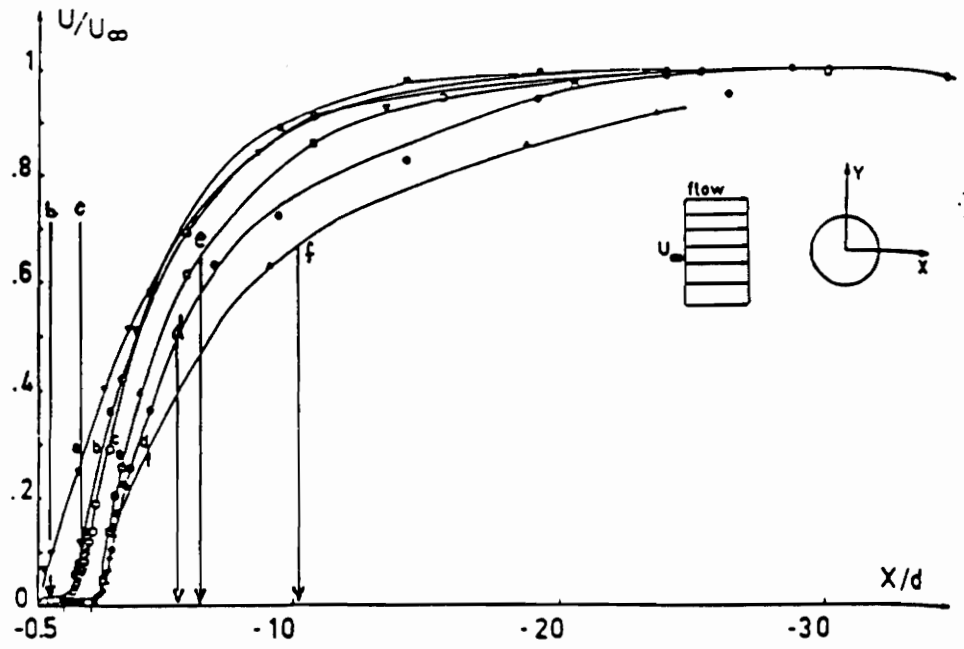

(after Koniuta, Adler, and Piau, 1980). Upstream velocity as a function of the distance from the cylinder center. Data are for a 1000 wppm solution. The vertical bars give λU/d. The different curves correspond to the different Reynolds numbers: a(0.4), b(1.1), c(2.5), d(7.0), e(7.9), and f(12.7).

Fig. 2.23. Normalized upstream velocity as a function of distance from cylinder center. The data is from Koniuta et. al. [49] and is replotted by Joseph [50].

$$\frac{\partial^2 \zeta}{\partial x^2}\left(1-\frac{1}{M^2}\right)+\frac{1}{We}\frac{\partial \zeta}{\partial x}=\frac{1}{M^2}\nabla^2\zeta \qquad (2.21)$$

where ζ is the vorticity. The vorticity is elliptic when M<1 and hyperbollic when M>1. It is also important to note that $M^2 = \mathrm{Re}\cdot We$. Thus the creeping flow assumption of Re=0 usually assumed in viscoelastic flow computations would not produce the behavior which results from a change of type of the vorticity. Joseph has proposed a possible distribution of the vorticity in the case of uniform flow over a cylinder in the supercritical (M>1) case which is shown in Fig. 2.24.

Delvaux and Crochet [51] and Hu and Joseph [52] have performed numerical simulations of a Maxwell fluid flowing past a cylinder at low but finite Reynolds number. The inclusion of convective terms in the momentum equation allows the change of type of the vorticity from elliptic to hyperbollic when the vorticity wave speed is exceeded. Delvaux and Crochet used the finite element technique described in Marchal and Crochet [26] which consisted of streamline upwinding and 4x4 bilinear subelements for stresses. The finite element domain of computation is shown in Fig. 2.25. The streamlines and vorticity contours are shown in Figs. 2.26(a) and 2.26(b). The streamlines shift downstream for all cases shown accept for Re=0. Thus the downstream shift of the streamlines was attributed to the change of type of the vorticity and not solely on elasticity or inertia. Delvaux and Crochet also performed these computations with the energy equation and examined the effect of elasticity and Re on Nu. The results shown in fig. 27 show that Nu does become nearly independent of Re at a critical Re, or velocity. The drag coefficient calculated by Delvaux and Crochet is also shown in fig. 27 and C_D is shown to become independent of Re as the critical velocity is exceeded. Hu and Joseph used a finite difference method to simulate the flow of a Maxwell fluid at low but finite Re on the computational domain shown in

fig. 28 [i]. Hu and Joseph obtained streamline patterns similar to that of Delvaux and Crochet and are shown in fig. 29(a). The vorticity contours are shown in fig. 29(b) and are similar to that of Delvaux and Crochet although more detail is shown. The results Hu and Joseph obtained for the drag coefficient and Nu are shown in figs. 30(a) and 30(b). The computed drag coefficients differ from that obtained by Delvaux and Crochet in that a rising drag coefficient is computed beyond a minimum. The computed Nu of Hu and Joseph are very similar to that obtained by Delvaux and Crochet. Hu and Joseph compared their numerical results to the experiments of James and Acosta [46]. The comparison between the computed C_D and Nu of Hu and Joseph and experimental C_D and Nu measured by James and Acosta is shown if fig. 31. The agreement is at best qualitative but a plot critical velocity versus polymer concentration, ϕ, appears to agree somewhat well with the experiments of James and Acosta.

In summary, there appears to be a critical fluid velocity at which anomalous transport behavior occurs in polymer solutions. It has been suggested that this critical velocity at which the anomalous behavior occurs corresponds to the vorticity wave speed of that fluid. To date, no experiments or numerical simulations have been performed with polymer melts, or constitutive equations which realistically represent polymer melts.

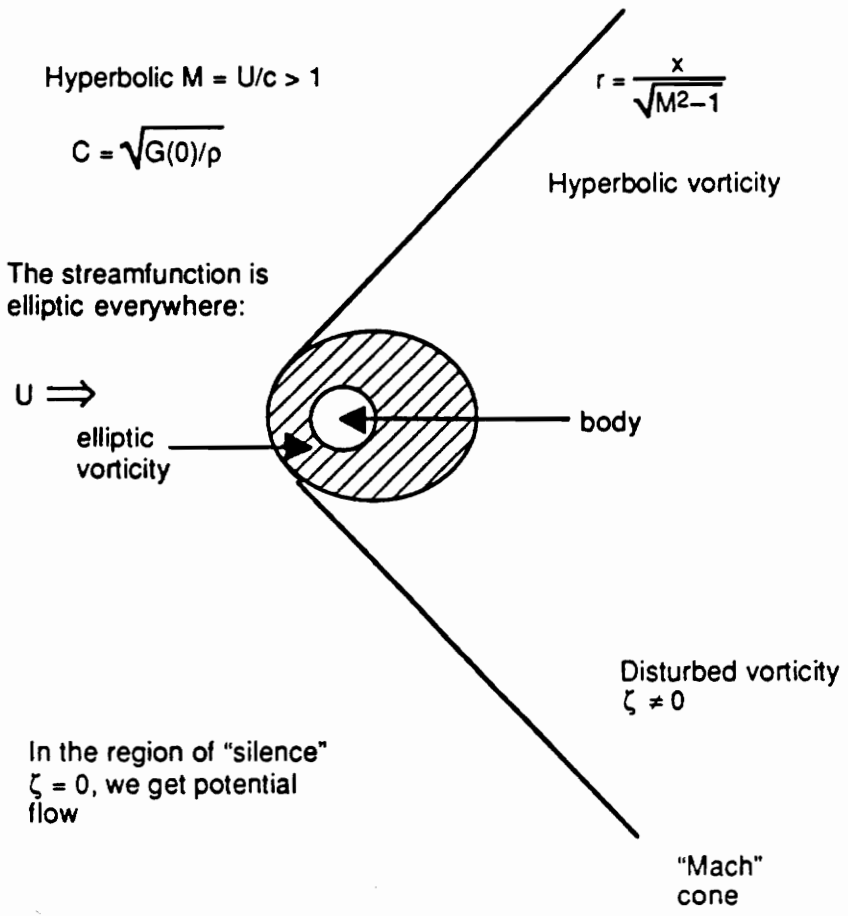

Fig. 2.24. Vorticity distribution proposed by Joseph for the supercritical (M>1) flow of a viscoelastic fluid past a cylinder [50].

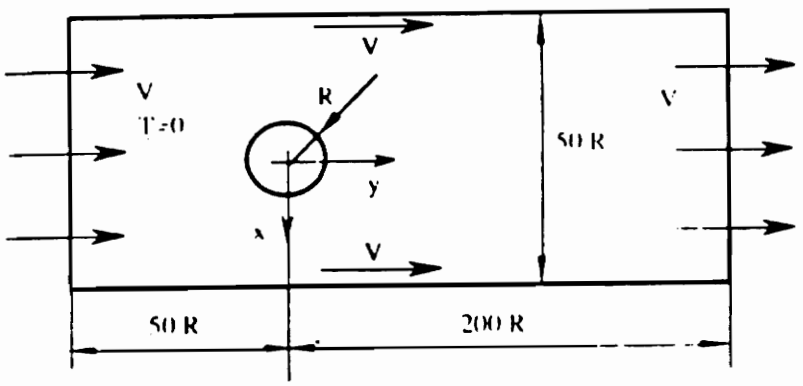

Fig. 2.25. Schematic of geometry and boundary conditions of finite element compuations performed by Delvaux and Crochet [51].

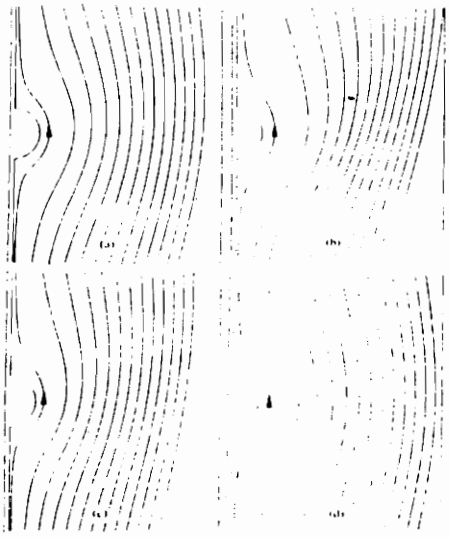

Streamlines in the neighbourhood of the cylinder in the following situations: (a) $E = 2.08$, $M = 0.5$; (b) $E = 2.08$, $M = 2.08$; (c) $We = 0$, $Re = 1.44$; (d) $We = 3$, $Re = 0$. The streamlines correspond to streamtubes with the same flow rate.

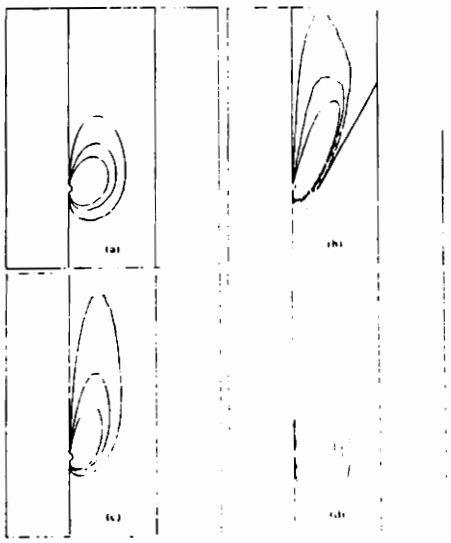

Vorticity contours for the same situations as in Fig. 7; the isovorticity values $\omega R/1$ are given by 0.01, 0.03 and 0.05.

Fig. 2.26. Streamlines and vorticity contours of finite element compuations performed by Delvaux and Crochet [51].

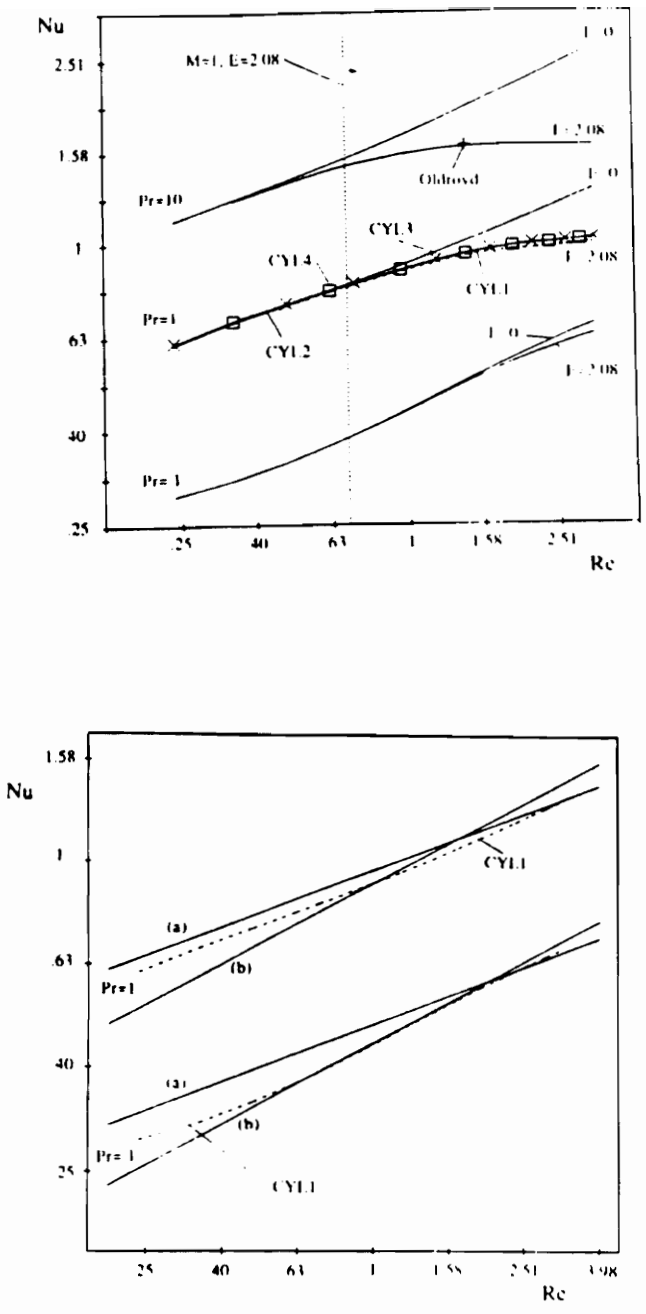

Fig. 2.27. Nu and C_D computed by Delvaux and Crochet as a function of Re [51].

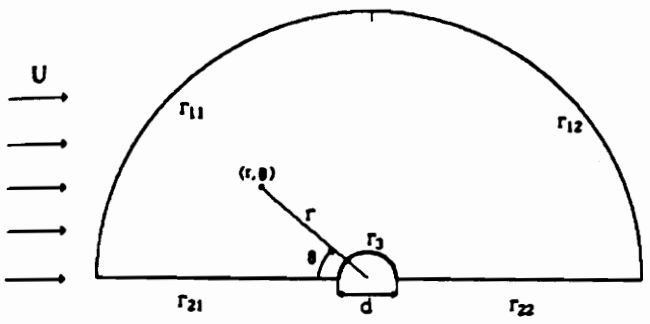

Fig. 2.28. Computational domain of Hu and Joseph with boundary conditions [52].

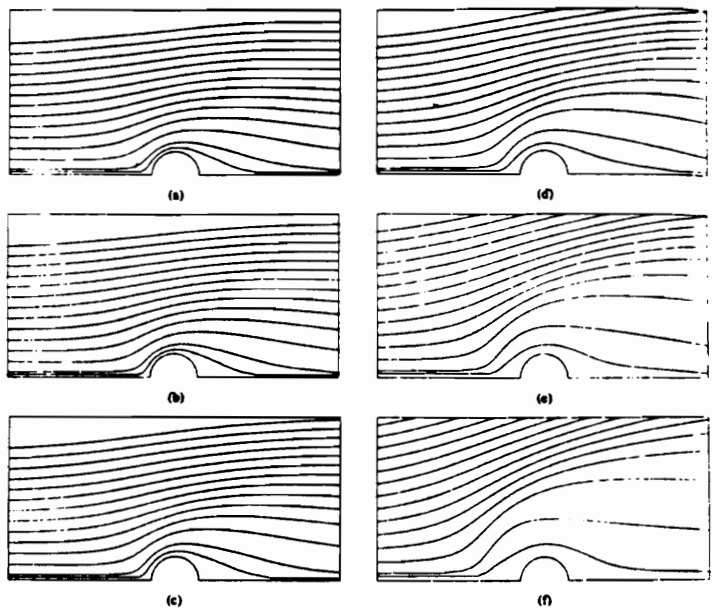

Streamlines on the neighborhood of the cylinder for the flow of the same Reynolds number $\mathscr{R} = 10$ and different elasticity numbers E. (a) $E = 0$ ($M = 0$). (b) $E = 0.01$ ($M = 1.0$). (c) $E = 0.1$ ($M = 3.16$). (d) $E = 0.25$ ($M = 5.0$). (e) $E = 0.5$ ($M = 7.07$). (f) $E = 1.0$ ($M = 10$). In the figures the values of the incoming streamlines, starting from the bottom, are 0.01, 0.05, 0.2, 0.4, 0.6, 0.8, 1.0, 1.2, 1.4, 1.6, 1.8, 2.0, 2.2 and 2.4.

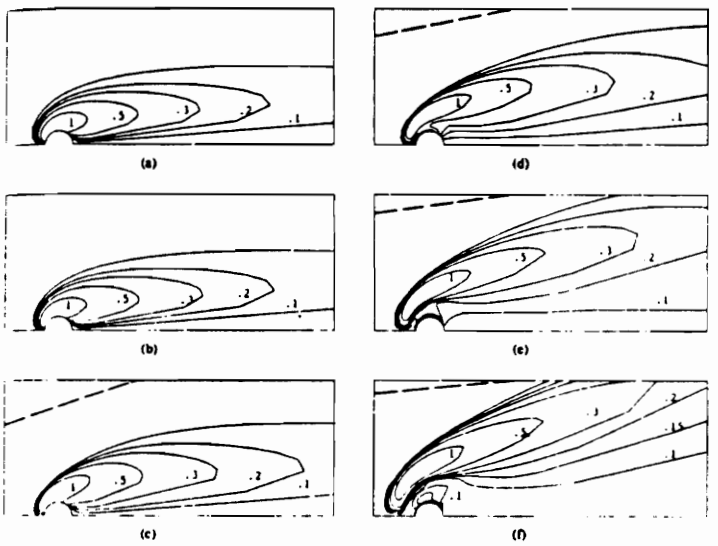

. Isovorticity lines for the flow of the same Reynolds number $\mathscr{R} = 10$ and different elasticity numbers E. (a) $E = 0$ ($M = 0$). (b) $E = 0.01$ ($M = 1.0$). (c) $E = 0.1$ ($M = 3.16$). (d) $E = 0.25$ ($M = 5.0$). (e) $E = 0.5$ ($M = 7.07$). (f) $E = 1.0$ ($M = 10$). — — —, angle of the vorticity shocks predicted in the linearized theory.

Fig. 2.29. Computed streamlines and vorticity contours of Hu and Joseph [52].

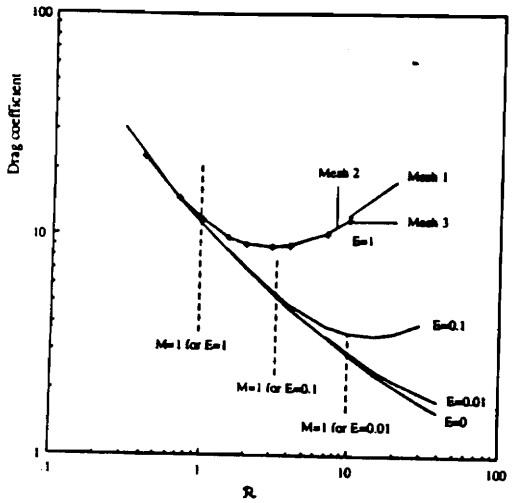

Drag coefficient C_D vs. Reynolds number $\mathscr{R}$ for elasticity numbers $E = 0$ (Newtonian), 0.01, 0.1 and 1.0. ——, results obtained using mesh 2; for $E = 1$, the results obtained by the other two meshes are also plotted. — — —, values of the Reynolds number at which the viscoelastic Mach number $M = 1$.

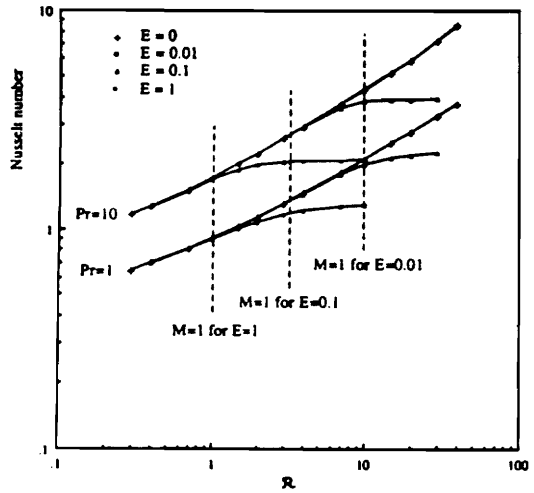

Nusselt number Nu vs. Reynolds number $\mathscr{R}$ for different elasticity numbers $E = 0$ (Newtonian), 0.01, 0.1, 1.0, and at Prandtl numbers $Pr = 1$ and 10. — — —, values of the Reynolds number at which the viscoelastic Mach number $M = 1$.

Fig. 2.30. Drag coefficient and Nu computed by Hu and Joseph [52].

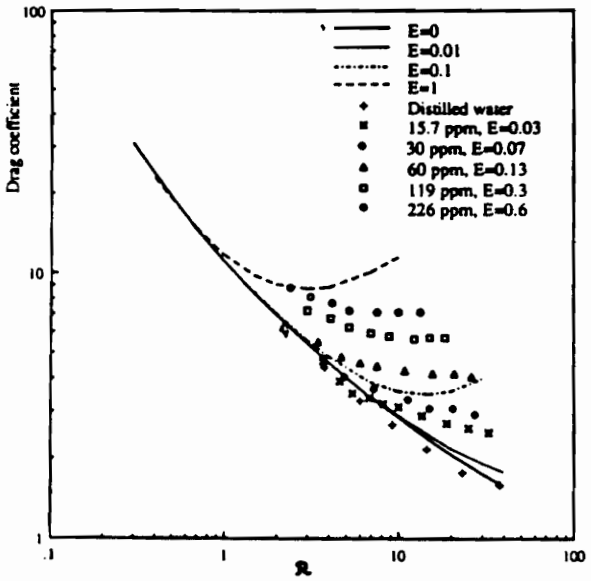

Comparison of the drag coefficients obtained by the present computation (lines) with those measured in experiments of James and Acosta [6] (dots). The elasticity numbers for the experimental data are estimated using the shear wave speed as described.

Fig. 2.31. Comparison of experimental measurements of James and Acosta with numerical simulations of Hu and Joseph [52].

2.5 Summary

In summary, there are several unresolved issues relating to viscoelastic flow through banks of cylinders, transverse to a single cylinder, and in complex geometries in general. Nearly all recent experimental work in this area has focused on polymer solutions, which add many complexities to the problem such as stress induced phase separation, inertia due to low viscosities in common flow situations, and experimental difficulties in measuring extensional viscosity. To date, there has been no investigations which have used polymer melts, which are much more representative of viscoelastic flow. Numerical simulations have failed to capture the important flow characteristics of viscoelastic flow through banks of cylinders, principally the pressure drop. Calculation of the pressure drop is the most important goal of these calculations.

2.6 Research Objectives

The proposed research may be divided into three areas. The first consists of measuring pressure drops of LDPE and LLDPE flowing through a square array of cylinders. The second area is concerned with the effect of fluid memory of flow over cylinders in a channel and involves the geometry shown in Fig. 2.32 (shown with one cylinder). The third area involves calculations which attempt to predict the behavior observed in banks of cylinders and flow around single cylinders. The fluids chosen allow analysis of important flow properties such as fluid memory and extensional viscosity, which have been discussed previously in this chapter. LDPE is an extensional strain hardening fluid and has an extensional viscosity greater than the Trouton value. LLDPE has an extensional viscosity which is much lower than LDPE. The differences in extensional behavior of these two fluids enables flow characteristics which are caused by extensional behavior of the fluid to be analysed.

2.6.1 Flow of LDPE and LLDPE through Square Arrays of Cylinders

A flow cell, which is shown in Fig. 2.32, has been constructed. This cell allows a permeability cell to be inserted. Pressure drops of a fluid flowing through this array may then be measured. Experiments of this type are performed at 170^{o}C with LDPE (NPE-953) and LLDPE (NTA-101). Permeability cells contain 1/16 inch OD cylinders and have a solid fraction of 0.60.

2.6.2 Effect of Fluid Memory on Flow over Cylinders in a Slit Die

Quartz viewing windows with one, two, and three blank 1/16 inch ID holes have been fabricated for use in a previously constructed slit die. Flow birefringence experiments consist of recording the isochromatic birefringence patterns resulting from the flow field. A quantitative stress field may then be constructed from these patterns, although the direction of the principle stress difference will not be known. Two types of flow conditions will be examined for each type of fluid: De>1 and De<1.

2.6.3 Numerical Simulations

All numerical simulations are performed using Polyflow. This software package enables the Phan Thien-Tanner model and Integral model of Papanastasiou to be used in conjunction with finite element methods utilizing SU and SUPG intgration schemes (see Lit. Rev. for details). With parameters for each of these models obtained from fits to experimental data, simulations are performed for the following geometries: 1. flow between two cylinders; 2. flow between one cylinder and a flat surface; 3. extension of no. 2 to three cylinders in series. The computed stress fields are compared to birefringence measurements by use of the linear stress-optical law. In addition to comparing the computed results to the experiments, the SUPG and SU methods will be compared in order to determine the accuracy of SU methods in the flow problems of interest in this research.

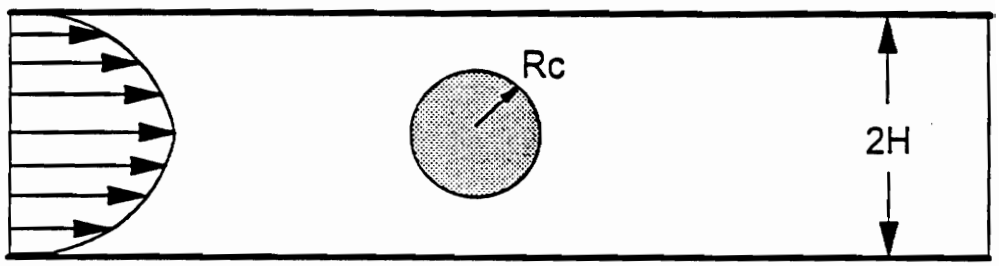

Fig. 2.32. Schematic of geometry for flow past a cylinder in a channel.

2.7 References

1. H. Darcy, Les fontaines publiques de la ville de Dijon Paris:Delmont.
2. R.B. Bird, Stewart, and Lightfoot, Transport Phenomena, chap. 7.
3. L. Skartsis, J.L. Kardos, B. Khomami, Poly. Eng. Sci., 32(4), 221 (1992).
4. L. Skartsis, B. Khomami, J.L. Kardos, J. Rheol., 36, 92(1992).
5. C. Chmielewski, K. Jayaraman, J. Rheol., 36, 121 (1992).
7. K. Talwar, B. Khomami, J. Rheol., 36, 1377(1992).
8. A. Souvaliotis, A.N. Beris, J. Rheol. 36, 417(1992).
10. A. Scheidegger, The physics of Flow through Porous Media, 3rd Ed.
11. S. Ergun, Chem. Eng. Progress, 40, 89 (1932).
12. P.C. Carmen, 15, 150(1974).
13. P.C. Carmen, J. Soc. Chem. Ind. Trans., 57, 225(1938).
14. J. M. Coulson, Trans. Inst. Chem. Eng., 27, 237(1949).
15. Z. Kemblowski, M. Michniewicz, Rheol. Acta., 18, 730(1979).
16. J. A. Guin, D.P. Kessler, R.A. Greencorn, Chem Eng. Sci., 26, 1475(1971).
17. L. Skartsis, J.L. Kardos, B. Khomami, Poly. Eng. Sci., 32(4), 221 (1992).
18. L. Skartsis, B. Khomami, J.L. Kardos, J. Rheol., 36, 92(1992).
19. R. J. Marshal, A.B. Metzner, Ind. Eng. Chem. Fund., 6, 393(1967).
20. D.F. James, D.R. McLaren, J. Fluid Mech., 70, 733(1975).
21. F. Durst, R. Haas, W. Interthal, J. Non-Newt. Fluid Mech., 22, 169(1987).
22. P. N. Dunlap, L.G. Leal, J. Non-Newt. Fluid Mech., 23, 5(1987).
23. G. Marrucci, G. Astarita, AIChE J., 13, 93(1967).
24. R.B. Bird, R.C. Armstrong, and O. Hassager, Dynamics of Polymeric Liquids, Vol. 1.
25. D.D. Joseph, M. Renardy, J. Saut, Arch. Ration. Mech. Anal., 87, 213(1985).
26. J. M. Marchal, M.J. Crochet, J. Non-Newt. Fluid Mech., 22, 219(1987).
27. A. Brooks, T. Hughs, Comp. J. Meth. Appl. Mech. Eng., 32, 199(1982).
28. R.I. Tanner, H. Jin, J. Non-Newt. Fluid Mech., 41, 171(1991).
29. G. Georgiou, S. Momani, M.J. Crochet, K.Walters, J. Non-Newt. Fluid Mech., 40, 231(1991).
30. S.A. White, A.T. Gotsis, D.G. Baird, J. Non-Newt. Fluid Mech., 24, 121(1987).
32. G.H. McKinley, W. Raiford, R.A. Brown, R.C. Armstrong, J. Fluid Mech., 223, 411(1991).
33. G.G. Fuller, Ann. Rev. Fluid Mech., 22, 387(1991).
35. H. Janeschitz-Kriegl, Polymer Melt Rheology and Flow Birefringence.
36. J. A. Deiber, W.R. Schowater, AIChE J., 27, 912(1981).
37. S. Pilitsis, A.N. Beris, J. Non-Newt. Fluid Mech., 31, 231(1989).
38. S.R. Burdetted, P.J. Coates, R.C. Armstrong, R.A. Brown, J. Non-Newt. Fluid Mech., 35, 405(1990).
39. D.F. Janes, N. Phan-Thien, M.K. Khan, A.N. Beris, J. Non-Newt Fluid Mech., 35, 405(1990).
40. M.J. Crochet, J.V. Delvaux, J. M. Marchal, J. Non-Newt. Fluid Mech., 34, 261(1990).

41. R. N. Zheng., N. Phan-Thien, R.I. Tanner, M.B. Bush, J. Rheol., 34, 79(1990).
42. S. Pilitsis, A. Souvalioti., A.N. Beris, J. Rheol, 33, 605(1991).
43. J.S. Ultman, M.M. Denn, Chem. Eng. J., 2, 81(1971).
44. O. Manero, B. Mena, J. Non-Newt. Fluid Mech., 9, 387(1981).
45. S.A. Dhahir, K. Walters, J. Rheol., 33(6), 781(1989).
46. D.F. James, A.J. Acosta, J. Fluid Mech., 42, 269(1970).
47. D.F. James, O.P. Gupta, Chem. Eng Prog. Symp. Series, 67(111), 62(1971).
48. A. Ambari, C. Deslouis, B. Tribollet, Chem. Eng. Commun., 29, 63(1984).
49. A. Koniuta, P.M. Adler, and J.M. Piau, J. Non-Newt. Fluid Mech., 7, 101(1980).
50. D.D. Joseph, Fluid Dynamics of Viscoelastic Liquids.
51. V. Delvaux, M.J. Crochet, J. Non-Newt. Fluid Mech., 37, 297(1990).
52. H.H. Hu, D.D. Joseph, J. Non-Newt. Fluid Mech., 37, 347(1990).

3.0 THE FLOW OF VISCOELASTIC FLUIDS THROUGH BANKS OF CYLINDERS[1]

Preface

In this chapter it is attempted to determine whether the pressure drop for a polymer melt flowing transversely through a square array of cylinders can be predicted using purely viscous models or whether a viscoelastic constitutive equation is required. To predict these pressure drops, finite element calculations were performed using the generalized Newtonian fluid (GNF) model with the Bird-Carreau viscosity function, as well as two viscoelastic constitutive equations, the Phan-Thien/Tanner (PTT) model and the Rivlin-Sawyers (RS) model with the Papanastasiou, Scriven, and Macosko (PSM) damping function. The constitutive equations were fit to the steady shear viscosity of a LLDPE melt and a LDPE melt. The PTT and RS models were also fit to uniaxial extensional stress growth data for each melt. The predictions of the pressure drop by means of the finite element calculations and a capillary model based on Darcy's Law were compared to pressure drops from experiments performed with the two polymer melts. The agreement between experimental data and theoretical predictions was best for the calculations using the PTT model. The calculations using the PTT model as the constitutive equation indicate that time dependent fluid properties and extensional rheology must be correctly predicted by the constitutive equation used if accurate pressure drops of viscoelastic fluids flowing through banks of cylinders are to be calculated.

[1]This paper is being submitted to the AIChE Journal.

3.1 Introduction

The flow of viscoelastic fluids through banks of cylinders is of practical interest in several processing operations. For example, the impregnation of thermoplastic composites involves squeezing a polymer melt through a bundle of fibers in an attempt to wet the fibers with the polymer melt. In the formation of electrical connection devices polymer melts are injected into cavities containing many pins. The polymer melt is required to flow in and around the cylinders. Finally, the filtration of polymer solutions used in the wet spinning of fibers can involve the flow of viscoelastic fluids through fibrous filters. Hence, there are a number of practical situations involving the flow of viscoelastic fluids through banks of cylinders.

The flow through banks of cylinders represents a form of porous media flow. Approaches to modeling of the flow of viscoelastic fluids through porous media have traditionally begun with Darcy's Law [1,2] which is adequate for most problems involving Newtonian fluids. Darcy found that the flow rate of a Newtonian fluid passing through a bed of spheres was directly proportional to the pressure drop per unit length. The proportionality constant was termed the permeability, and it incorporated the specific character of the porous media and the rheology of the fluid. Nutting [3] introduced the idea of the specific permeability, which decouples the porous media characteristics from the fluid rheology. This idea was used extensively by Wyckoff [4] and may be represented as

$$\underline{v}_o = \frac{k}{\mu}\underline{\nabla}P, \tag{3.1}$$

where v_o is the superficial velocity, k is the specific permeability, μ is the viscosity, and P is the pressure. The specific permeability, k, is generally assumed to have a constant value

which may be determined from experimental measurements. However, if the pressure drop is to be predicted a priori, a theoretical expression for k is necessary.

The successive treatments of Blake, Kozeny, and Carmen (BKC) resulted in a semi-empirical equation for the permeability that applies to the flow of Newtonian fluids at low Reynolds number and is referred to as a capillary model [2]. The BKC equation and slight modifications of it are the most widely used methods of modeling flow through porous media. Although the original model was theoretically derived, an empirical factor was required for the model predictions to match experimental data. This empirical factor is often called the tortuosity [2,5].

To account for the shear thinning rheology of many non-Newtonian fluids, Sadowski and Bird [6] and Christopher and Middleman [7] modified the BKC equation by using the Ellis model and power law model viscosity functions, respectively. The resulting modification of Darcy's Law derived by Christopher and Middleman for the case of a power law viscosity function is given as

$$v_o = K'\left(\frac{\Delta P}{2mL}\right)^{\frac{1}{n}}, \tag{3.2}$$

where v_o is the superficial velocity, m is the consistency, L is the length of the porous media, n is the power law index, and K' is the permeability which was calculated to be

$$K' = \frac{\varepsilon n}{3n-1}\left(\frac{D_p \varepsilon}{3(1-\varepsilon)}\right)^{\frac{n+1}{n}}\left(\frac{12}{25}\right)^{\frac{1}{n}}. \tag{3.3}$$

D_p is the mean particle diameter based on the specific surface area and porosity of the porous media [2], ε is the porosity, and the factor of 25/12 is an empirical modification necessary for Eqs. (2.2) and (2.3) to match experimental data for Newtonian fluids. Eqs.

(3.2) and (3.3) are commonly cast in terms of a friction factor (f) and a Reynolds number (Re) which are given as

$$f = \frac{\Delta P}{\rho v_o^2}\frac{D_p}{L}\frac{\varepsilon^3}{1-\varepsilon} \quad \text{and} \tag{3.4}$$

$$Re = \frac{v_o^{2-n} D_p \rho}{150(1-\varepsilon)H}, \tag{3.5}$$

where H is expressed as

$$H = \frac{m}{12}\left(9+\frac{3}{n}\right)^n (150k\varepsilon)^{\frac{(1-n)}{2}}, \tag{3.6}$$

and the product fRe, is a constant. By incorporating a shear thinning viscosity function into the porous media model, any purely viscous non-Newtonian effects should be accounted for.

The models developed by Sadowski and Bird [6] and Christopher and Middleman [7] were found to be inadequate for predicting friction factors of some viscoelastic fluids flowing through porous media [8,9]. Friction factors which deviated from those predicted by the modified BKC equation were attributed to elastic effects (which were not specifically defined), as it was believed that differences due to shear thinning were properly accounted for. In an attempt to account for fluid elasticity Sheffield and Metzner [9] used an empirical modification of a theoretical expression derived by Wissler [10]. Wissler used a perturbation analysis of the flow of a Maxwell fluid in a converging and diverging planar channel. Sheffield and Metzner [9] accounted for fluid elasticity by proposing that the flow resistance was a function of the Deborah number (De),

$$f\,Re = 1.0 + A \cdot De, \tag{3.7}$$

where A is an experimentally determined constant and De is defined as the ratio of the relaxation time of the fluid (based on shear properties) to the residence time of the fluid in

the porous media. They compared their model predictions to the experimental data of Sadowski and Bird [18] and found that the predicted friction factors deviated from the experimental friction factors by less than 6.8%. However, Sheffield and Metzner also calculated that a deviation of friction factors by 6.8% amounts to nearly a 30% error in the predicted flow rate for a given pressure drop, indicating that further developments are required to accurately predict pressure drops of viscoelastic fluids flowing through porous media. Also, it should be noted that correlating f to De is purely empirical and does not reflect which viscoelastic behavior is important other than transient behavior as reflected in De.

Possible reasons for the disagreement between experimental data and the predictions of capillary models for viscoelastic fluids flowing through porous media have been discussed by Durst et al. [11]. They suggested that models based on Darcy's Law simply could not capture the converging and diverging nature of the flow kinematics that occur in porous media. Durst et al. observed that the finitely extensible nonlinear elastic (FENE) dumbbell model for dilute polymer solutions [12] predicted an extensional viscosity versus extension rate curve which was qualitatively similar to experimental values of Eq. (3.7) versus De. They concluded that extensional rheology had to be modeled correctly if accurate predictions of the pressure drop were to be calculated and suggested incorporating the FENE model into porous media models.

Several experimental studies have been carried out using periodic arrays of cylinders. Chmielewski and Jayaraman [13] constructed an apparatus which enabled them to measure the pressure drop of a fluid flowing transversely to periodic arrays of cylinders with a void fraction of 0.70. They chose three Boger-type fluids (polyisobutylene in polybutene) [14] of different molecular weight and a shear thinning polymer solution of polyisobutylene in decalin. The extensional flow behavior of each solution was

characterized in a fiber spinning apparatus and the flow resistance of each fluid was related to its extensional viscosity. Experiments with each of the fluids resulted in a drastic increase of the product fRe, at a critical De, indicating an increasing resistance to flow. The magnitude of the product fRe scaled with extensional viscosity indicating that extensional rheology had an impact on the flow resistance, as Durst et al. predicted [11]. It was observed that the flow became unsteady at a critical value of De. The downstream pressure fluctuated about an average value for De>1.2. Based on these results Chmielewski and Jayaraman [13] concluded that the assumption of a steady two dimensional flow field close to Stokes flow was not appropriate for viscoelastic fluids in such geometries due to purely elastic instabilities. Skartsis et al. [15] performed experiments similar to Chmielewski and Jayaraman using an aqueous polyacrylamide solution, two Boger fluids of different concentration (polyacrylamide, corn syrup, and water), and an aqueous solution of xanthan gum flowing through a square array of cylinders with a void fraction of 0.455. They also found that the product fRe, increased drastically at a critical De, although the critical De was different from that reported by Chmielewski and Jayaraman [13]. No unsteady flows were reported by Skartsis et al. [15].

An important aspect of the experiments of Chmielewski and Jayaraman [13] and Skartsis et al. [15] is worthy of mention. Both research groups used a pressurized tank as a device to pump the polymer solutions through the banks of cylinders. Sadowski and Bird [18] performed experiments similar to those of Chmielewski and Jayaraman [13] and Skartsis et al. [15] and found that a constant pressure flow delivery system resulted in unsteady flows through a bed of spheres while a constant flow rate system, provided by a gear pump, resulted in steady flows for a solution of carbopol (a cellulose derivative) in water. Sadowski and Bird concluded that gel formation, which is caused by loss of solubility, was a likely cause of these observations.

The presence of unsteady flows of polymer solutions when the temperature is within a few degrees of the theta temperature, which is the case for Boger-type fluids at room temperature, suggests that flow induced phase separation may be present [19]. Recent research performed by van Egmond and Fuller [20] indicated that polymer solutions in extensional flow fields were more prone to stress induced phase separation than in shear flows at the same temperature. Shear flows of polymer solutions have been shown to reduce the cloud point temperature, which is usually a few degrees below the theta temperature by as much as 30^{o}C [19]. The possibility of phase separation being responsible for the drastic increases in flow resistance observed for polymer solutions flowing through banks of cylinders as opposed to purely elastic effects must be carefully examined before one can attribute the unsteady flows observed by Chmielewski and Jayaraman [13,21] to a purely elastic instability.

Banks of cylinders arranged in periodic arrays may represent an ideal geometry for numerical calculations because the domain of the calculation may consist of only one period, such as the area shown in Fig. 3.1. In addition, we can describe the geometry of flow channels. Several researchers have attempted to predict the pressure drops of polymer solutions flowing through periodic arrays of cylinders by performing finite element computations on a single period of the array, such as the domain shown in Fig. 3.1 and then summing the pressure contributions [16,17]. These computations involve solving discretized forms of the equations of conservation of mass and momentum coupled with a constitutive equation. Talwar and Khomami [16] have implemented higher order finite element analysis, or p-elements, to perform simulations of viscoelastic flow through a square array of cylinders in an attempt to simulate the experiments of Skartsis et al. [15]. To model the viscoelastic behavior of the polymer solutions which were used in the experiments, Talwar and Khomami [16] used the Maxwell model and Oldroyd-B models

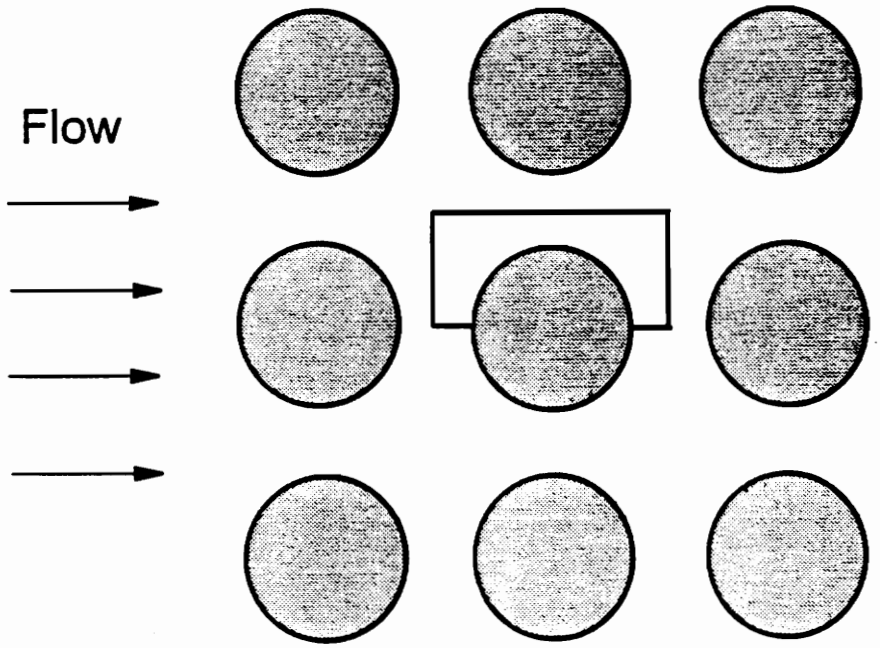

Fig. 3.1. Schematic representation of a square array of cylinders. The enclosed region is used for finite element calculations.

for the constitutive equations. They found that their numerical predictions always resulted in a decreasing flow resistance, as determined by the product fRe, as De increased whereas the experiments resulted in an increase of the product fRe as De for increased. Souvaliotis and Beris [17] performed numerical simulations on the same geometry using domain decomposition spectral techniques. They also chose the Maxwell and Oldroyd-B constitutive equations. Their calculations agreed with the results of Talwar and Khomami in that a decreasing product fRe versus De was always predicted. In addition, converged solutions could not be obtained by Talwar and Khomami [19] or Souvaliotis and Beris [17] for De>1.2. Talwar and Khomami [19] and Souvaliotis and Beris [17] both concluded that the discrepancy between their numerically predicted product fRe and experiments was due to time dependent flow instabilities caused by fluid elasticity which resulted in pressure drops higher than those calculated assuming steady state flows.

In summary, the issue of whether all viscoelastic fluids flowing through banks of cylinders will experience a drastic increase in flow resistance at a critical De has not been resolved. The cause of the observed increase in flow resistance has been attributed to a purely elastic flow instability, although stress induced phase separation has not been adequately addressed as a possible cause of the instability. Finite element calculations that have been performed with the Maxwell and Oldroyd-B constitutive equations predict a decreasing flow resistance as De is increased, contrary to experimental evidence for Boger-type fluids.

The purpose of this paper is to determine whether a purely viscous model is adequate for predicting the pressure drop of two polymer melts flowing through banks of cylinders or whether a viscoelastic constitutive equation is necessary. Pressure drop predictions based on finite element calculations will be compared to experimental data for two polymer melts flowing through a square array of cylinders with a void fraction of

0.40. By using a well defined geometry which can be modeled by finite element methods, the geometry is eliminated as an unknown so that the fluid behavior may be examined. Polymer melts are used in this study in order to eliminate the possible complexity of stress induced phase separation. Two polymer melts, LLDPE and LDPE, are used because of their similarities in shear rheology and differences in time dependent and extensional rheology. Time dependent extensional properties are more easily measured for highly viscous polymer melts than polymer solutions. Finite element calculations are performed with three rheological constitutive equations: one purely viscous model which predicts shear thinning viscosity and two viscoelastic models which can predict the shear behavior as well as the differences in time dependent shear and extensional rheology of the two polymer melts. The viscoelastic constitutive equations used in this work enable the time dependent shear rheological properties and extensional viscosity to be varied almost independently so that their effects may be analyzed.

3.2 Experimental Apparatus and Materials

3.2.1 Materials

Two polymer melts were used in this study: a linear low density polyethylene (LLDPE), NTA-101, supplied by Mobil and a low density polyethylene (LDPE), NPE-953, supplied by Quantum. LLDPE has a molecular topology consisting of a linear backbone with short, low molecular weight side-chain branches. NTA-101 has a weight average molecular weight (M_W) of 110,000 and a polydispersity index of 4.0. LDPE is a highly branched polymer with long side chain branches. NPE-953 has a M_W of 116,000 and a polydispersity index of 9.1.

3.2.2 Rheological Characterization

Rheological characterization of LLDPE and LDPE was performed in both shear and extensional flow. Shear rheological measurements were performed using a Rheometrics Mechanical Spectrometer (Model RMS-800) and an Instron Capillary Rheometer (ICR Model 3211). Extensional rheological measurements were performed using a Rheometrics Extensional Rheometer (Model RER 9000).

For both polymer melts the steady shear viscosity (η) was measured for shear rates from 0.01 to 4.641 s^{-1} at 170 C in a nitrogen environment using the RMS-800 with a cone and plate geometry. The cone angle was 0.1 rad and the plate diameter was 2.54×10^{-2}m for all tests using the RMS-800. Beyond this range of shear rates,

steady shear flow measurements were not possible due to loss of melt from between the cone and plate.

To obtain the shear viscosity for higher shear rates the Instron Capillary Rheometer was used. Three capillaries with a diameter of 6.86×10^{-4}m and L/D ratios of 12.5, 37.1, and 75.1 were used for measurements performed at a temperature of 170°C. Using the Rabinowitsch correction to calculate the wall shear rate and the Bagley correction for entrance pressure losses, the shear viscosity as a function of shear rate was calculated from pressure drop and flow rate data [24]. Shear rates up to 100 s^{-1} are reported here.

Transient shear flow measurements were carried out using the cone and plate geometry at a temperature of 170 C. Dynamic oscillatory measurements were carried out to obtain the complex viscosity (η^*), storage modulus (G'), and loss modulus (G"). Measurements were carried out for angular frequencies (ω) ranging from 0.1-100.0 rad/s. Shear stress growth $\left(\tau^+\right)$ measurements upon inception of steady shear flow and shear stress relaxation $\left(\tau^-\right)$ measurements upon cessation of steady shear flow were carried out for shear rates ranging from 0.02154 to 2.154 s^{-1}. Finally, jump strain measurements were carried out for strains ranging from 0.10 to 4.0.

Uniaxial extensional stress growth measurements were carried out using a Rheometrics Extensional Rheometer (Model RER 9000) which is based on the Munstedt design [22]. In this rheometer, a molded cylinder of polymer is suspended in a heated oil bath between a fixed arm and a mobile arm. The density of the oil (Dow Corning Type 710) and the polymer are matched at the test temperature of 170°C so that there are no buoyancy effects. The polymer sample is then deformed at a constant extension rate and the force measured by a transducer. Extensional stress growth data was obtained for extension rates ranging from $0.020s^{-1}$ to $0.20s^{-1}$. Calculation of the

extensional stress $\left(\sigma_E^+\right)$ and viscosity $\left(\eta_E\right)$ were carried out by well known procedures [21]. The maximum extensional Hencky strain attained for these tests was approximately 2.5. A steady value of the extensional stress was obtained for LLDPE but not for LDPE.

3.2.3 Permeability Cell Apparatus

In order to study the flow of polymer melts through a bank of cylinders, a permeability cell was constructed consisting of seventy 1.587×10^{-3}m (1/16 in.) diameter steel cylinders arranged in a square packing with a void fraction of 0.40. The permeability cell was mounted in a slit die geometry as shown in Fig. 2. The bank of cylinders was held together by supports placed in slots in the die channel. The cross-sectional area of the die channel was 6.36×10^{-2}m by 1.81×10^{-2}m (.25 in. by 0.715 in.).

Pressure transducers were mounted flush to the die walls upstream and downstream of the bank of cylinders. A Dynisco pressure transducer (model PT422A) was placed 1.27×10^{-2}m upstream of the permeability cell with a range of 0-20.68 MPa (0-3000 psi) and 1.27×10^{-2}m downstream of the cell with a range of 0-3.447 MPa (0-500 psi). Heating of the die was accomplished by using three control zones, each with its own thermocouple, heating strip, and proportional-integral (PI) controller. The polymer was fed to the die by means of a Zenith Gear Pump (Zenith Model HPB-5556) which was fed by a Killion extruder (0.0254 m diameter). By using the gear pump flow and pressure oscillations were minimized.

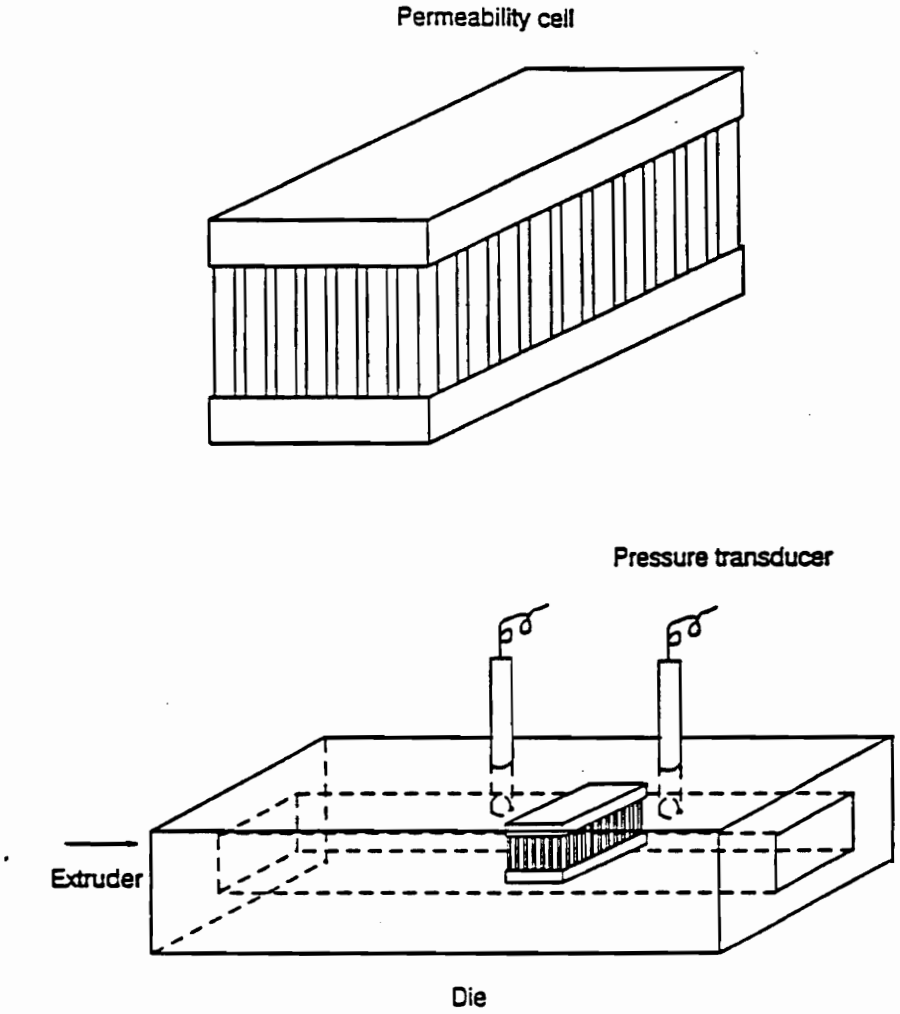

Fig. 3.2. Experimental geometry used to measure the pressure drop of polymer melts flowing through a bank of cylinders.

3.3 Rheological Constitutive Equations

The predictions of three constitutive equations and their fit to rheological data obtained in simple well defined flows will be discussed in this section. In order to accurately model the flow of a non-Newtonian fluid it is important to use a constitutive equation that accurately predicts the behavior of the fluid in homogeneous, steady and time dependent shear and extensional flows (flows of known kinematics). Also, in more complex flows, such as flow through a bank of cylinders in which fluid elements pass through a series of contractions and expansions, time dependent and extensional rheological properties of the fluid may have an effect on the flow behavior. The effects of time dependent rheological properties and extensional viscosity behavior of polymer melts flowing through a contraction have been discussed by White et al. [23]. It is clear from their results that time dependent properties and extensional flow behavior must be predicted correctly by the constitutive equation if one is to obtain accurate numerical predictions of polymer melt flow in complex geometries.

The generalized Newtonian fluid (GNF) constitutive equation with a Bird-Carreau (BC) viscosity function [24,25], the Phan-Thien and Tanner (PTT) constitutive equation [26,27], and the Rivlin-Sawyers (RS) constitutive equation with the Papanastasiou, Scriven, and Macosko (PSM) damping function [28] were used in this paper. The GNF constitutive equation has been widely used for engineering calculations involving non-Newtonian fluids [24]. The GNF constitutive equation predicts a shear viscosity that is dependent on the shear rate. However, it does not predict any time dependent properties, and the extensional viscosity is predicted to be $3\eta(\dot{\gamma})$ which may not be realistic for many polymer melts [24]. The PTT model and

RS model with the PSM damping function were chosen because of their realistic predictions of extensional viscosity and time dependent rheological properties such as stress growth upon startup of shear flow and stress relaxation upon cessation of shear flow.

The following sections will consider how the GNF, PTT, and RS constitutive equations were formulated, as well as their predictions of shear viscosity and extensional stress growth behavior. In addition, the fit of each constitutive equation to the steady shear viscosity and extensional stress growth behavior for LLDPE and LDPE at 170^{o}C will be presented.

3.3.1 Generalized Newtonian Fluid Constitutive Equation

The generalized Newtonian fluid (GNF) constitutive equation is an extension of the Newtonian constitutive equation where the viscosity is replaced with a viscosity function, $\eta(\dot{\gamma})$, and is expressed as

$$\underline{\underline{\tau}} = \eta(\dot{\gamma})\,\underline{\underline{\dot{\gamma}}}, \tag{3.9}$$

where a tensile stress is defined to be positive. The rate of deformation tensor, $\underline{\underline{\dot{\gamma}}}$, is defined as

$$\underline{\underline{\dot{\gamma}}} = \underline{\nabla}\underline{\mathbf{v}} + (\underline{\nabla}\underline{\mathbf{v}})^{\mathbf{t}}, \tag{3.10}$$

and the magnitude of the rate of deformation tensor, $\dot{\gamma}$, is

$$\dot{\gamma} = \sqrt{\frac{1}{2}\underline{\underline{\dot{\gamma}}}:\underline{\underline{\dot{\gamma}}}}\,. \tag{3.11}$$

Although there are many choices for $\eta(\dot{\gamma})$, we use the Bird-Carreau model given below as

$$\frac{\eta-\eta_\infty}{\eta_o-\eta_\infty}=\left(1+(\lambda\dot{\gamma})^2\right)^{\frac{n-1}{2}}, \tag{3.12}$$

where η_0 is the zero shear viscosity, η_∞ is the viscosity at infinite shear rate, λ is a time constant, and n is a parameter that determines the degree of shear thinning. The Bird-Carreau model was chosen because of its ability to correctly predict the shear thinning viscosity behavior of many polymer melts and solutions. It does not, however, predict time dependent behavior or the appropriate extensional behavior.

The values of the parameters in the BC viscosity function are obtained by fitting Eq. (3.12) to steady shear viscosity data after taking $\eta_\infty=0$, which is acceptable for most polymer melts. The nonlinear least squares routine RNLIN (IMSL) is used to obtain the best fits.

3.3.2 Phan-Thien and Tanner Constitutive Equation

The Phan-Thien and Tanner (PTT) constitutive equation was derived from molecular considerations and was based on the ideas of non-affine network theories [26,27]. Defining a tensile stress as positive, the PTT model with one relaxation mode may be expressed as

$$\exp\left(\frac{\lambda\varepsilon}{\eta_1}\mathrm{tr}(\tau_1)\right)\underline{\underline{\tau}}_1+\lambda\,\underline{\underline{\tau}}_{1(1)}+\frac{\lambda\xi}{2}\left(\underline{\underline{\dot{\gamma}}}\cdot\underline{\underline{\tau}}_1+\underline{\underline{\tau}}_1\cdot\underline{\underline{\dot{\gamma}}}\right)-\eta_1\underline{\underline{\dot{\gamma}}}=0, \tag{3.13}$$

where λ, ξ, η_1, and ε are adjustable parameters, and $\underline{\underline{\tau}}_{1(1)}$ is the upper convected derivative. The parameter λ is a relaxation time, ξ is related to the non-affineness of the network, η_1 is related to the viscosity, and ε represents the rate of destruction of the temporary network junctions. In this form Eq. (3.13) predicts a maximum in the shear stress as a function of shear rate. Therefore, the stress is expressed as

$$\underline{\underline{\tau}} = \underline{\underline{\tau}}_1 + \underline{\underline{\tau}}_2 \tag{3.14}$$

where $\underline{\underline{\tau}}_1$ is the viscoelastic extra stress given by Eq. (3.13) and $\underline{\underline{\tau}}_2$ is a purely viscous contribution expressed as

$$\underline{\underline{\tau}}_2 = \eta_2 \underline{\underline{\dot{\gamma}}}, \tag{3.15}$$

where η_2 is a parameter with the units of viscosity. The addition of the viscous stress to the total stress tensor prevents a maximum in shear stress versus shear rate from occurring. It has been found that to keep the stress a monotonically increasing function of shear rate, η_2 must be chosen so that $\eta_1 \leq 8\eta_2$.

The predictions of the PTT model in simple shear flow are

$$\eta = \frac{\eta_1}{\left[1+\xi(2-\xi)\lambda^2\dot{\gamma}_{12}^2\right]} + \eta_2, \tag{3.16}$$

$$N_1 = \frac{2\eta_1\lambda\dot{\gamma}_{12}^2}{\left[1+\xi(2-\xi)\lambda^2\dot{\gamma}_{12}^2\right]}, \text{ and} \tag{3.17}$$

$$N_2 = -\frac{\xi}{2}N_1, \tag{3.18}$$

where N_1 and N_2 are the first and second normal stress differences, respectively. The values of the parameters λ, ξ, and η_1 are determined by setting $\eta_2 = (1/8)\eta_1$ and performing a nonlinear least squares fit of Eq. (3.16) to shear viscosity data.

The PTT model has an adjustable parameter which primarily affects the extensional viscosity predictions. The PTT model predicts an extensional viscosity versus extension rate curve for which the extensional viscosity begins at the Trouton value of $3\eta_o$ at low extension rates and then increases through a maximum. The magnitude of the maximum relative to the Trouton value is determined by the value of the parameter ε. The shape of the extensional viscosity-strain rate curve predicted by the PTT model has been found to be in agreement with experimental data for some polymers, including LDPE [22].

3.3.3 Rivlin-Sawyers Model

The Rivlin-Sawyers (RS) constitutive equation with the Papanastasiou, Scriven, and Macosko (PSM) damping function is used because of its ability to fit both shear and extensional data. The general form of the Rivlin-Sawyers constitutive equation is

$$\underline{\underline{\tau}}(t) = \int_{-\infty}^{t} M(t-t')\left[\phi_1(I_1,I_2)\,\underline{\underline{C}}^{-1} + \phi_2(I_1,I_2)\,\underline{\underline{C}}\right] dt', \tag{3.19}$$

where the relative finite strain tensors, $\underline{\underline{C}}^{-1}$ and $\underline{\underline{C}}$, are the Finger and Cauchy strain tensors, respectively [24]. M(t-t') is the viscoelastic memory function which is expressed as

$$M(t-t') = \sum_{i=1}^{N} \frac{\eta_i}{\lambda_i^2} \exp\left[-\frac{t-t'}{\lambda_i}\right], \tag{3.20}$$

where η_i and λ_i are adjustable parameters related to the relaxation spectrum. The ϕ_i's are the nonlinear damping functions. Several different forms of the nonlinear damping function have been proposed by various researchers [24,25]. The form of the function ϕ_1 proposed by Papanastasiou, Scriven, and Macosko [28] is used here because of its excellent ability to fit the steady and transient material functions for LLDPE and LDPE. Papanastasiou, Scriven, and Macosko observed that data suggested a sigmoidal form of the damping function, ϕ_1, versus strain curve. The result for ϕ_1 is

$$\phi_1 = \frac{\alpha}{(\alpha-3)+\beta I_1+(1-\beta)I_2} \tag{3.21}$$

where α and β are adjustable parameters, with β only affecting extensional flow predictions. The scalar invariants, I_1 and I_2, are defined to be

$$I_1 = \mathrm{tr}\left(\underline{\underline{C}}^{-1}\right) \quad \text{and} \tag{3.22}$$

$$I_2 = \mathrm{tr}\left(\underline{\underline{C}}\right). \tag{3.23}$$

ϕ_2 is taken to be zero.

In order to determine the values of the adjustable parameters contained in the memory function, η_i and λ_i, the predictions of the linear viscoelastic storage modulus (G') and the linear viscoelastic loss modulus (G") as a function of ω must be fit to experimental values. The values of η_i are determined by performing a simultaneous nonlinear least squares fit of the following equations to experimental data

$$G'(\omega) = \sum_{k=1}^{N} \frac{\eta_k \lambda_k \omega^2}{1+(\lambda_k \omega)^2} \quad \text{and} \tag{3.24}$$

$$G''(\omega) = \sum_{k=1}^{N} \frac{\eta_k \omega_j}{1+(\lambda_k \omega_j)^2}, \tag{3.25}$$

where ω is the frequency. The selection of the λ_k's is taken to be at decade intervals where the longest relaxation time is chosen so that $\lambda_1\omega_{min}>1$ and $\lambda_{min}\omega_{max}<1$, where ω_{min} and ω_{max} are the lowest and highest frequencies for which data are available.

The value of the parameter α is determined by fitting Eq. (3.21) to experimental values of the damping function. In shear flow Eq. (3.21) reduces to

$$\phi_1 = \frac{\alpha}{\alpha + \gamma^2}, \tag{3.26}$$

where γ is the applied shear strain. Experimental values of the damping function are calculated using the relation

$$\phi_1 = \frac{G(t,\gamma)}{G(t)}, \tag{3.27}$$

where γ is the applied step strain, $G(t,\gamma)$ is the nonlinear relaxation modulus, and $G(t)$ is the linear viscoelastic relaxation modulus. Details of the measurements are given in Appendix B.

Once the values of the η_i's, λ_i's, and α have been determined from shear flow data, the value of the parameter β may be determined. Estimation of the value of the parameter β is accomplished by fitting the extensional stress growth prediction of Eq. (3.19) to extensional stress growth data. The effect of the value of β on the extensional viscosity predictions of the RS model with the PSM damping function is similar to the effect of ε on the same predictions of the PTT model.

3.3.4 Fits of the Constitutive Equations to Rheological Data

In this section fits of the GNF model with a BC viscosity function, the PTT model, and the RS model with the PSM damping function are compared to steady shear viscosity and extensional stress growth data for LLDPE and LDPE at 170°C. The values of the model parameters for each of the constitutive equations used in this study are based on the methods discussed previously and are listed in Table 3.1.

3.3.4.1 Fit of Shear Properties

The fits of the GNF model with the BC viscosity function, the PTT model, and the RS model with the PSM damping function to steady shear viscosity data for LLDPE and LDPE melts at 170°C are presented in Figs. 3.3 and 3.4. The GNF model with the BC viscosity function and the RS model with the PSM damping function both provide excellent fits to the viscosity data for shear rates between 0.01-100.0 (s^{-1}). The fit of the PTT model to the shear viscosity of LLDPE is not exact between the shear rates 0.01-100.0 (s^{-1}), as the viscosity is slightly overpredicted for shear rates between 0.10 and 20 (s^{-1}). For LDPE, as a result of η_2 the viscosity levels off at $\dot{\gamma} > 10$, whereas the data still shows shear thinning behavior.

3.3.4.2 Fit of Extensional Properties

For LLDPE, fits of the PTT and RS model with the PSM damping function to extensional stress growth data are shown in Fig. 3.5. For LDPE, fits of the PTT and RS model with the PSM damping function to extensional stress growth data are shown

in Fig. 3.6. The fits of both the PTT model and RS model with the PSM damping function to extensional stress growth data for LLDPE and LDPE are good.

Table 3.1. Values of the parameters of the rheological models to fit simple shear and uniaxial extensional behavior of LLDPE and LDPE at 170 C.

coefficient	value	
Power Law model	LLDPE	LDPE
m	13800	5400
n	0.858	0.490
Bird-Carreau model		
η_o	12300	14300
λ	1.1	5.3
n	0.65	0.51
PTT model		
η_1	11830	15745
η_2	1479	1967
λ	0.46	4.1
ξ	0.01	0.09
ε	0.10	0.01
PSM model		
$\eta_1(\lambda_1=10^{-3})$	450	85.0
$\eta_2,(\lambda_2=10^{-2})$	2200	550
$\eta_3,(\lambda_3=10^{-1})$	4400	2100
$\eta_4(\lambda_4=10^{0})$	6100	7900
$\eta_5(\lambda_5=10^{1})$	3400	12000
$\eta_6(\lambda_6=10^{2})$	120	7600
$\eta_7(\lambda_7=10^{3})$	25.0	0.20
α	2.14	10.9
β	0.10	0.021

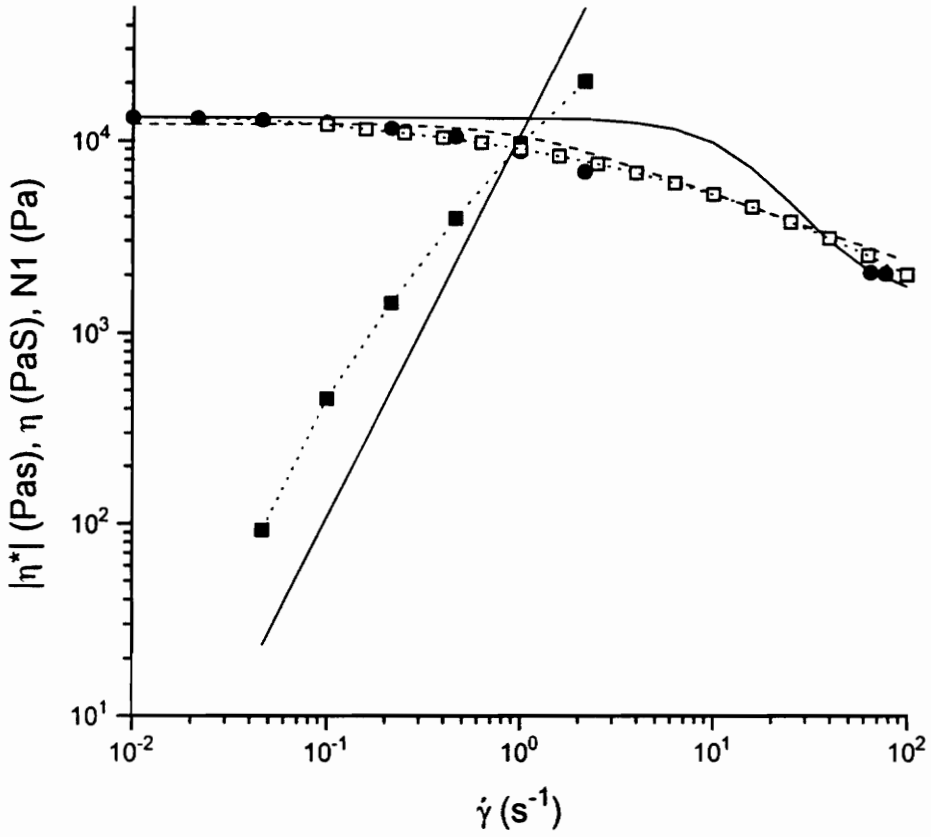

Fig. 3.3. Viscosity and first normal stress difference versus shear rate for LLDPE at 170°C, $|\eta^*|$ (□); η (●); N_1 (■); GNF model with BC viscosity function (- - - - -); PTT model (———); RS model with PSM damping function (·····).

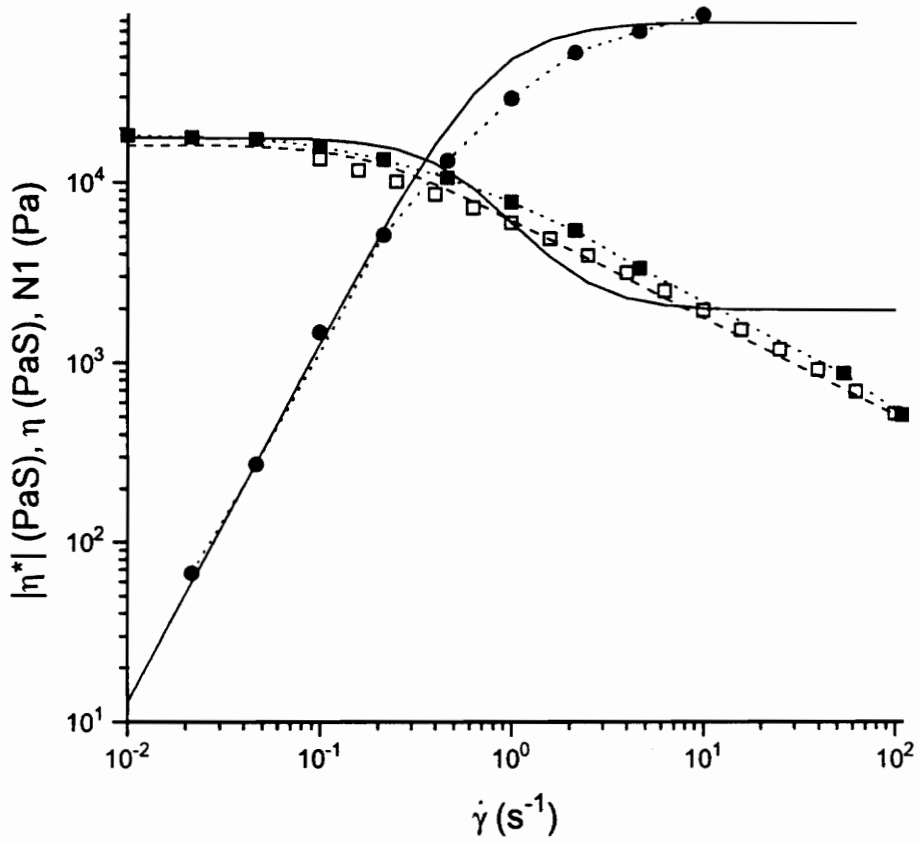

Fig. 3.4. Viscosity and first normal stress difference versus shear rate for LDPE at 170°C, $|\eta^*|$ (□); η (■); N_1 (●); GNF model with BC viscosity function (- - - - -); PTT model (———); RS model with PSM damping function (·····).

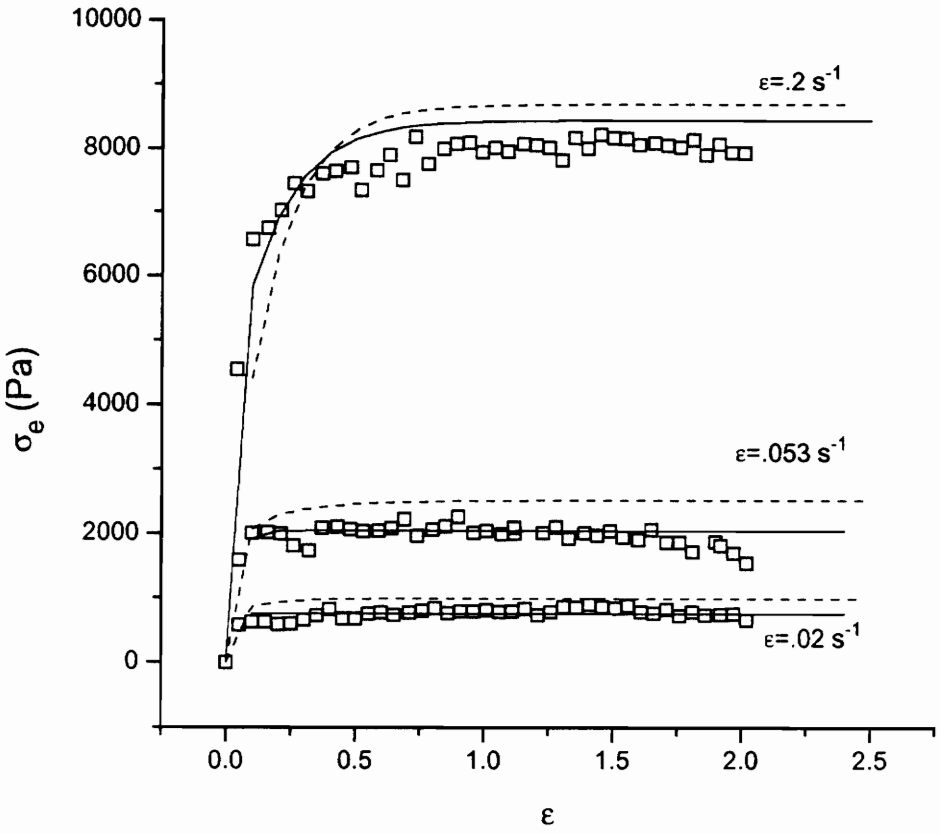

Fig. 3.5. Uniaxial extensional stress versus strain for LLDPE at 170°C, experimental (□); RS model with PSM damping function (———); PTT model (- - - - -).

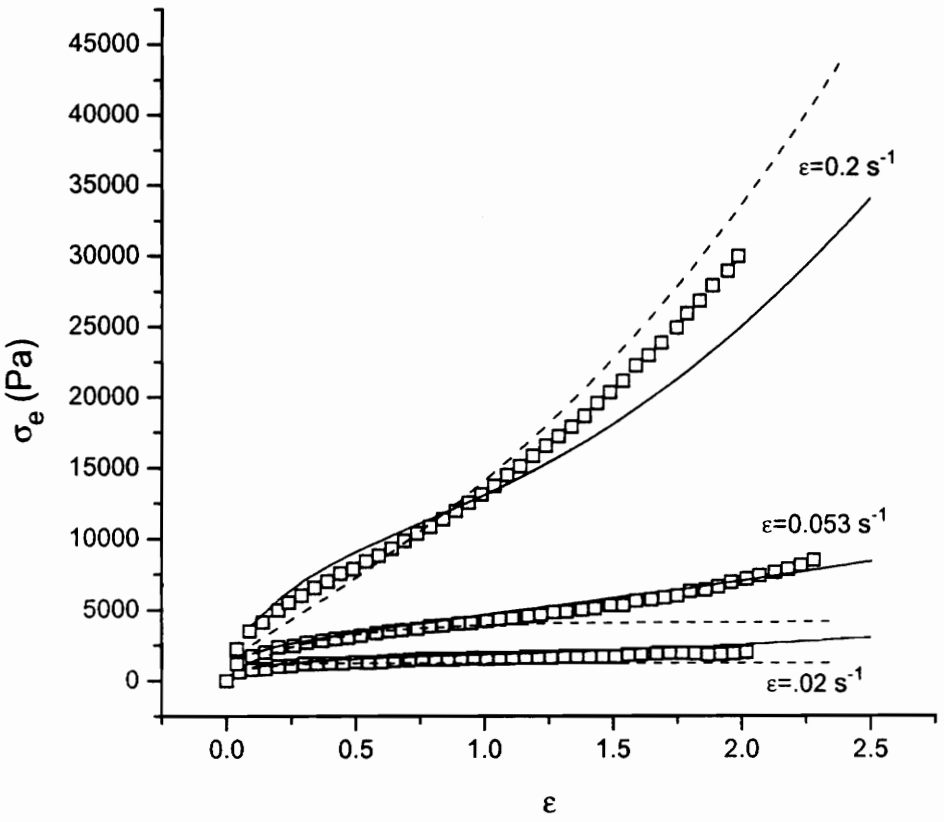

Fig. 3.6. Uniaxial extensional stress versus strain for LDPE at 170°C, experimental (□); RS model with PSM damping function (———); PTT model (- - - - -).

3.4 Finite Element Method

The equations that describe the isothermal, inertialess flow of incompressible viscoelastic fluids are the equation of conservation of mass, equations of conservation of momentum, and the constitutive equation which are given below, respectively

$$v_{i,i} = 0, \tag{3.27}$$

$$\tau_{ij,j} - P_{,i} = 0, \text{ and} \tag{3.28}$$

$$h\left(\tau_{ij}, \dot{\gamma}_{ij}, v_i, t, \ldots\right) = 0, \tag{3.29}$$

where v_i are components of the velocity vector, τ_{ij} are components of the extra stress tensor, P is the isotropic pressure, $\dot{\gamma}_{ij}$ are components of the rate of deformation tensor, t is the time, and h is a differential or integral operator. In this case, the Einstein notation is used and a tensile stress is taken as positive.

In this study the finite element program Polyflow (Polyflow s.a., ver. 3.1.1) was used to solve Eqs. (3.27)-(3.29). The Galerkin velocity-pressure formulation was used to solve the system of equations where the GNF constitutive equation was used. For finite element calculations using the PTT constitutive equation, the 4x4SU method developed by Marchal and Crochet [31] was used to obtain converged solutions. In the 4x4SU method, Marchal and Crochet have applied streamline upwinding to the convective terms in the constitutive equation. The 4x4 refers to the division of each finite element into 16 subelements on which the stresses are approximated using bilinear basis functions. The ability of this method to produce realistic predictions of the flow of LLDPE and LDPE past cylinders in a planar channel is addressed in chapter 4 [34]. The technique developed by Dupont et al. is used to solve the system of equations where the RS constitutive equation is used [36]. In this technique the RS constitutive equation is decoupled from the equations of continuity and momentum.

From an initial or iterated velocity field the stresses are calculated using the RS equation. Using these newly calculated stresses, the equations of continuity and momentum are then solved by the finite element method using the Galerkin velocity-pressure formulation resulting in new velocity and pressure fields. This procedure is repeated until convergence of the velocity and pressure fields is reached.

In order to calculate the pressure drop of a fluid flowing through a periodic array of cylinders, it is initially assumed here that the pressure drop calculated for flow past a single cylinder (or between two cylinders) is additive. A schematic of the geometry for flow past a single cylinder is shown in Fig. 3.7(a) and the finite element mesh used in the simulation of this flow is shown in Fig. 3.7(b). To calculate the total pressure drop of a fluid flowing through the array of cylinders used in the experiments, which contains seven cylinders in the flow direction, the calculated pressure drop per cylinder must be multiplied by seven.

To test the assumption that the pressure drop calculated for flow between two cylinders could be applied additively to an array of cylinders, the flow geometry shown in Fig. 3.8(a) and finite element mesh in Fig. 3.8(b) are used. In the geometry in Fig. 3.8(a) flow between two cylinders is modeled and the calculated pressure drop per pair of cylinders may be compared to the pressure drop per cylinder calculated using the geometry in Fig. 3.7(a), which models one cylinder. Similarly, flow between three pairs of cylinders may be used to determine if the pressure drop per cylinder pair calculated when two pairs of cylinders are modeled may be applied additively to the array of cylinders. In this way the effect of fluid memory on the pressure drop per pair of cylinders may determined and the appropriate number of cylinders included in the pressure drop calculations.

The boundary conditions that are used for the flow problems discussed previously are shown in Fig. 3.9. The volumetric flow rate per unit width is specified along the inflow (Polyflow computes the velocity components from the flow rate and the velocity vector is actually the boundary condition), a zero traction vector at the outflow for the GNF model and RS model, the no slip condition along the cylinder wall(s), and a vanishing normal component of the velocity and shear stress along the planes of symmetry. The finite element calculations using the PTT model require additional boundary conditions which consist of the extra stresses at the inflow and the velocity profile at the outflow, instead of a zero traction vector. The inflow and outflow boundaries are placed ten cylinder diameters upstream and downstream of a cylinder so that the imposition of the velocity profiles at these boundaries does not affect the numerical solution near the cylinder.

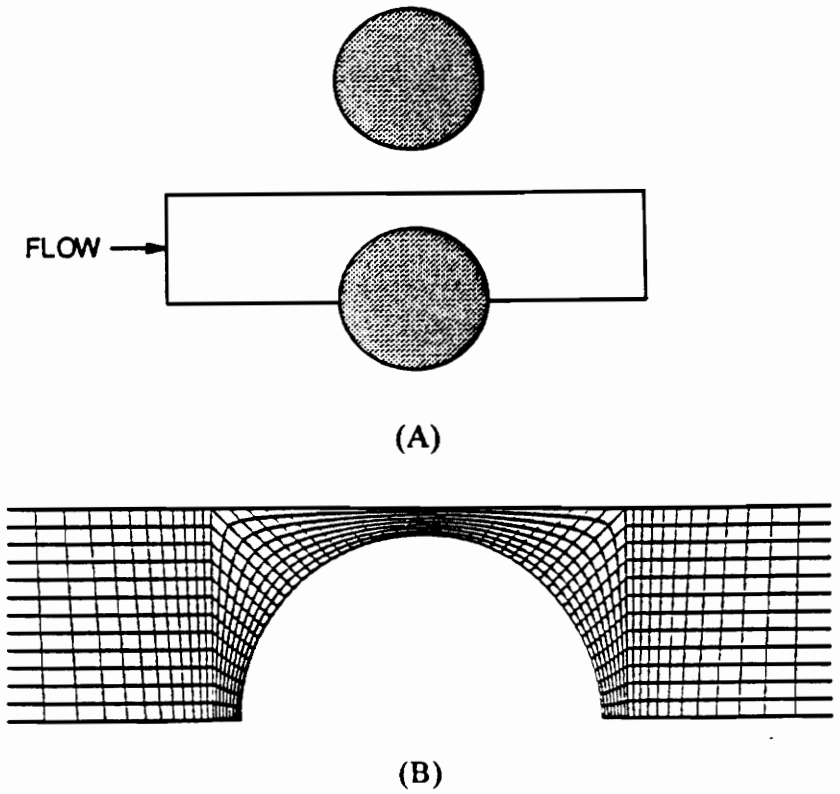

Fig. 3.7. Geometry used to model flow between a pair of cylinders in a periodic array of cylinders (A) schematic; (B) finite element mesh 1052 nodes.

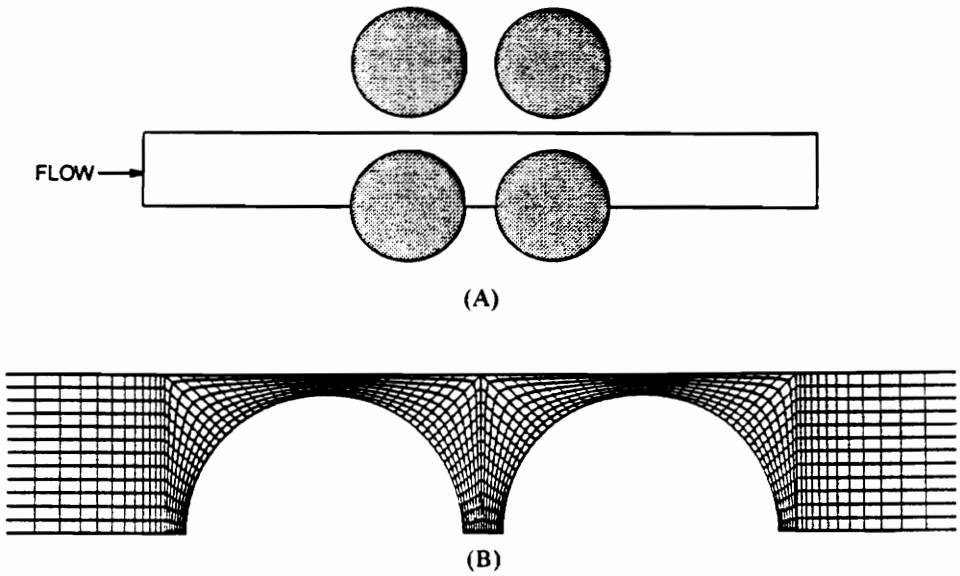

Fig. 3.8. Geometry used to model flow between two pairs of cylinders in a periodic array of cylinders (A) schematic; (B) finite element mesh 2305 nodes.

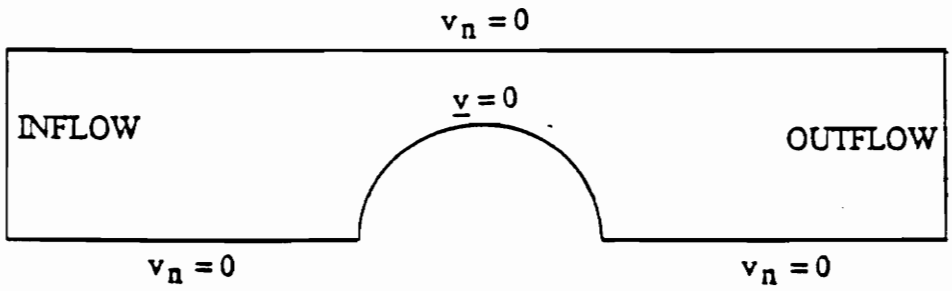

Fig. 3.9. Boundary conditions for flow between a pair of cylinders.

3.5 Results and Discussion

3.5.1 Predictions of Constitutive Equations in Simple Flows

3.5.1.1 Time Dependent Shear Flows

In order to be able to accurately simulate the flow of a viscoelastic fluid in a complex geometry using a given constitutive equation a basic requirement is that the material functions used to obtain the material parameters fit the experimental data well. At the same time because the flow between cylinders represents a series of accelerations and decelerations, the constitutive equation must reflect well the transient response of the fluid. In particular, based on the material parameters obtained from steady simple shear flow and the startup of uniaxial extensional flow the constitutive equation should be able to predict well the stress growth and stress relaxation behavior of the fluid.

In the flow through a periodic array of cylinders, fluid elements pass through a series of contractions and expansions where periodic increases and decreases in both extensional and shear deformation rates occur. Shear stress growth upon inception of steady shear flow $\left(\tau^{+}\right)$ and shear stress relaxation upon cessation of steady shear flow $\left(\tau^{-}\right)$ are used here to compare the time dependent rheological properties predicted by the PTT model and RS model with the PSM damping function to experimental data for LLDPE and LDPE. The predictions of the GNF model will not be discussed because this model predicts that the shear stress will instantaneously reach a steady value upon inception of steady shear flow and instantaneously reach zero upon cessation of steady shear flow.

In this section the predictions of the PTT model and RS model with the PSM damping function will be examined in time dependent shear flows. Representative stress growth and stress relaxation data for LLDPE and LDPE for De~0.85 will be shown ($De = \lambda\dot{\gamma}$ for simple shear flow). Additional data is presented in Appendix C.

τ^+ and τ^- at De=0.85 for LLDPE at 170°C are shown in Fig. 3.10 along with the predictions of the PTT model and RS model with the PSM damping function. The predictions of both constitutive equations agree qualitatively with the data in that τ^+ passes through a maximum and then attains a steady value. τ^- relaxes to zero within about 30s when the shear flow is stopped. The magnitude of τ^+ is overpredicted by the PTT model which is a consequence of the fit of η shown in Fig. 3.3. Further, the PTT model predicts that τ^- relaxes to zero faster than the data shown in Fig. 3.10.

The τ^+ and τ^- at De=0.83 for LDPE at 170°C are shown in Fig. 3.11 along with the predictions of the PTT model and RS model with the PSM damping function. As was the case for LLDPE, the predictions of both constitutive equations agree qualitatively with the data in that τ^+ passes through a maximum and then attains a steady value. τ^- relaxes to zero when the shear flow is stopped more slowly than predicted by both the PTT model and the RS model although both models correctly predict that stress relaxation occurs more slowly for LDPE than LLDPE at this De. The PTT model predicts a smaller stress overshoot than actually occurs and also overpredicts the steady value of the stress.

In comparing the predictions of the PTT model and RS model to stress growth and stress relaxation data, it can be seen that qualitative agreement is good but is not quantitatively exact. However, both the PTT model and the RS model correctly predict that LDPE has a larger stress overshoot than LLDPE for De=0.85 and that the stress relaxes to zero more slowly for LDPE than LLDPE. In the experiments

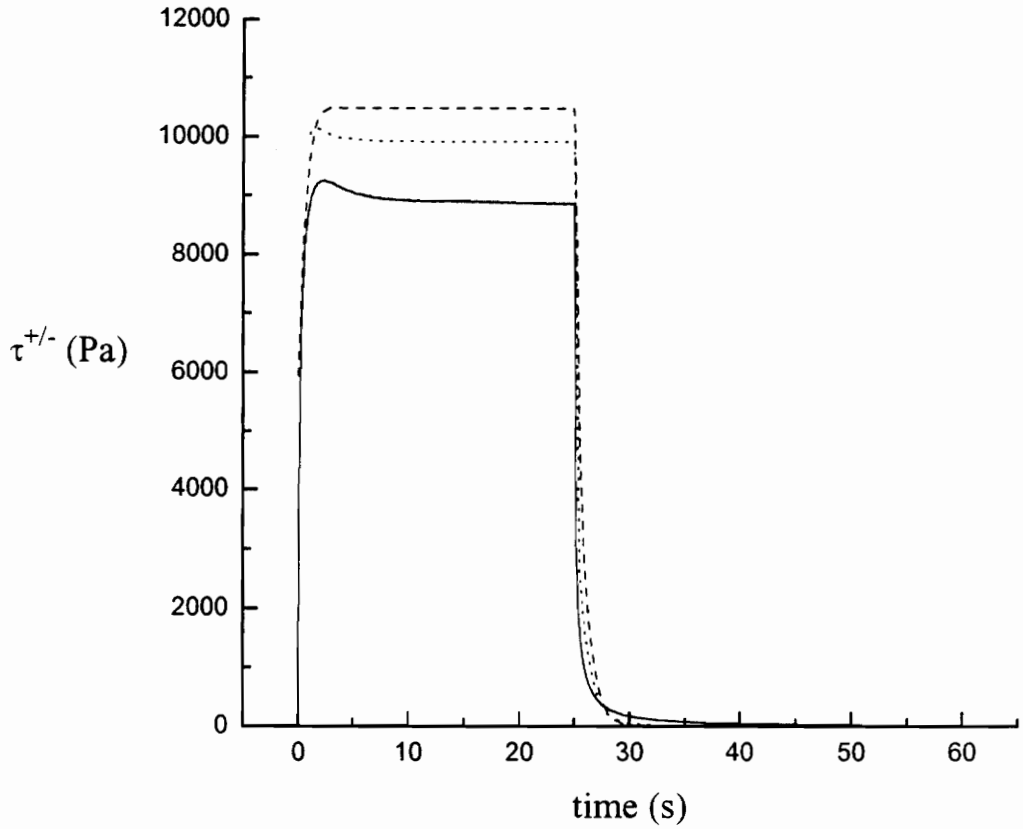

Fig. 3.10. Shear stress growth upon inception of steady shear flow and shear stress relaxation upon cessation of steady shear flow for LLDPE at 170°C and a shear rate of 1.0 s^{-1}: experimental (———); predictions of RS model with PSM damping function (·····); predictions of PTT model (- - - -); De=0.88.

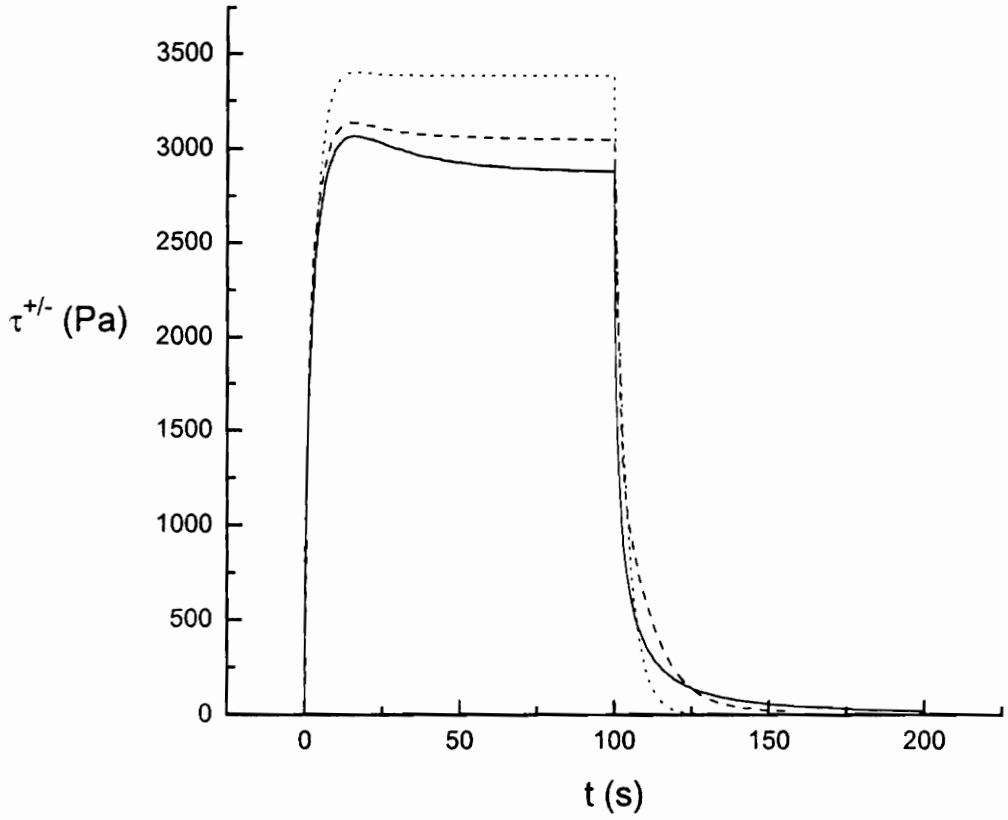

Fig. 3.11. Shear stress growth upon inception of steady shear flow and stress relaxation upon cessation of steady shear flow for LDPE at 170°C and a shear rate of 0.2154 s^{-1}: experimental (———); RS model with PSM damping function (- - - - -); PTT model (·····).

involving flow of LLDPE and LDPE through the bank of cylinders, shear rates larger than those shown in Figs. 3.10 and 3.11 typically occur (on the order of $25s^{-1}$). The stress overshoot is then also expected to be higher [24]. The PTT and RS models correctly predict that the stress overshoot increases with increasing shear rate. However, experimental data could not be attained for shear rates above about $5s^{-1}$ in our instrument due to force transducer range limitations.

3.5.1.2 Steady State Extensional Viscosity

The uniaxial extensional viscosity (η_E) versus extension rate $(\dot{\varepsilon})$ for LLDPE at 170°C along with predictions of the PTT model and RS model are shown in Fig. 3.12. The predictions of both constitutive equations are in agreement with the experimental data for the range over which data is available. However, for higher extension rates where experimental data is not available, the PTT model predicts a maximum in η_E versus $\dot{\varepsilon}$ whereas the RS model with the PSM damping function predicts an extension rate thinning extensional viscosity. The predictions of η_E are based on parameters determined from steady shear and uniaxial extensional stress growth experiments.

The instantaneous uniaxial extensional viscosity at a strain of ε=2.5 versus extension rate for LDPE at 170°C is shown along with predictions of the steady state extensional viscosity by the PTT model and RS model with the PSM damping function in Fig. 3.13. Experimental values of the steady state extensional viscosity could not be obtained for LDPE because the extensional viscosity was still increasing when the maximum strain that could be obtained in the extensional rheometer was reached. However, the instantaneous values provide some basis for comparison to the predictions of the constitutive equations. The instantaneous values of the uniaxial

extensional viscosity are somewhat in agreement with the steady state values predicted by the PTT model and RS model, but do not agree quantitatively.

There are two major differences between the extensional viscosity predictions of the PTT model and RS model with the PSM damping function shown in Fig. 3.12 for LLDPE and Fig. 3.13 for LDPE. The first is the magnitude of the maximum value of $(\eta_E / 3\eta_o)$ predicted for each polymer melt. The maximum value of $(\eta_E / 3\eta_o)$ predicted for LLDPE is 2.6 while that predicted for LDPE is more than 10.0. The second difference is the extension rate at which the maximum in $(\eta_E / 3\eta_o)$ is predicted to occur. For LLDPE the PTT model predicts the maximum to occur at $\dot{\varepsilon} \cong$ 2.8 s^{-1}, and the RS model with the PSM damping function does not predict a maximum. For LDPE both the PTT model and the RS model with the PSM damping function predict that the maximum occurs at $\dot{\varepsilon} \cong 0.24\ s^{-1}$.

The time dependent rheological behavior and steady state extensional rheological behavior discussed in this section are expected to have an effect on the accuracy of the numerical simulation of a polymer melt flowing through a periodic array of cylinders. It has been shown that the PTT model and the RS model with PSM damping function predict at least qualitatively the differences in time dependent rheological behavior and extensional viscosity behavior that are observed to occur for LLDPE and LDPE.

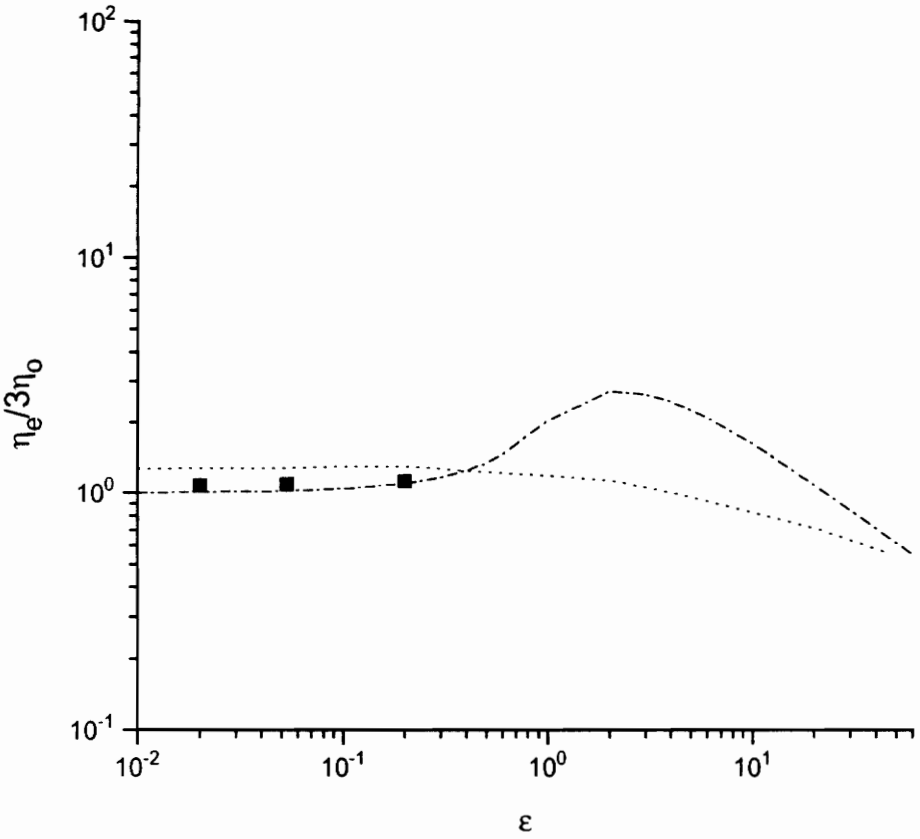

Fig. 3.12. Uniaxial extensional viscosity versus strain rate for LLDPE at 170°C. Symbols represent experimental values and the lines represent predictions of the PTT model (-·-·-·-), and RS model with PSM damping function (·····).

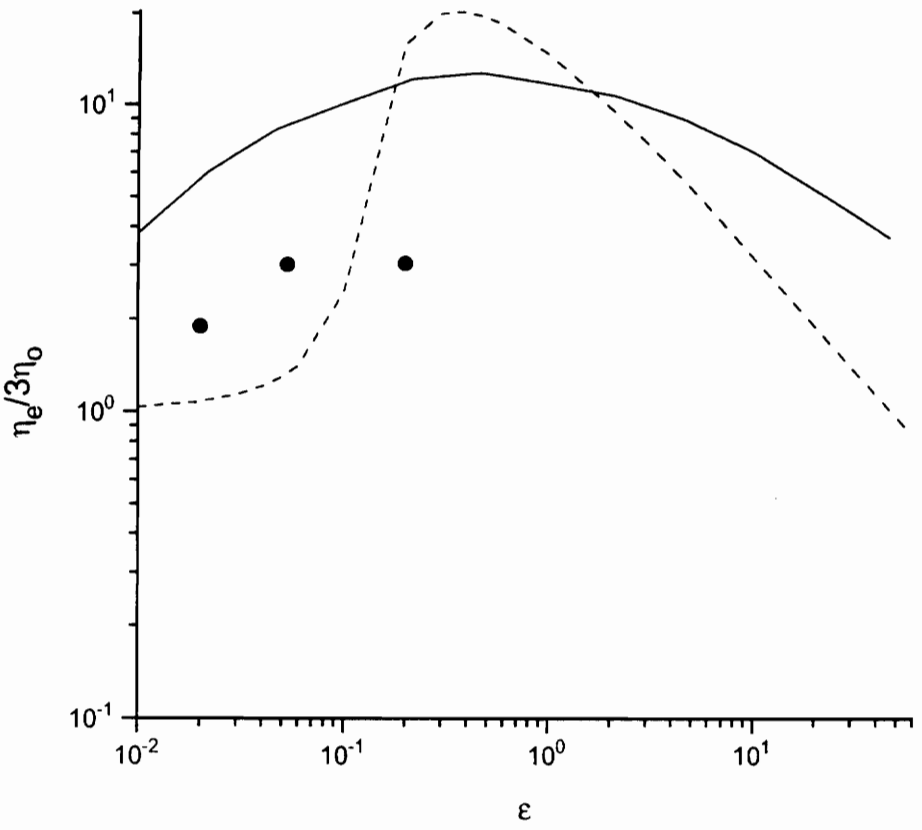

Fig. 3.13. Uniaxial extensional viscosity versus strain rate for LDPE at 170°C. Symbols represent instantanious values at ε=2.5 and the lines represent predictions of the PTT model (- - - - -), and RS model with PSM damping function (———).

3.5.2 Predictions of the Capillary Model

The pressure drop for a viscoelastic fluid flowing through a periodic array of cylinders is commonly defined in terms of the friction factor predicted by a capillary model. The capillary model derived by Christopher and Middleman (CM), given in Eqs. (3.4) and (3.5), is used here as a framework for presenting experimental data. The friction factors calculated for LLDPE and LDPE flowing through a bank of cylinders are presented with predictions of the CM model in Fig. 3.14. The capillary model predictions are in agreement with the data for LLDPE at the lowest Re for which data is presented. As Re increases the model begins to overpredict the friction factor. Although the deviation does not appear to be great in Fig. 3.14, one must keep in mind that it is a log-log scale and small errors in the friction factor translate into large errors in the predicted pressure drop. The largest error in the friction factor predicted by the CM model for LLDPE is 21%, but the error in predicted pressure drop is 48%. For LDPE, the friction factors predicted by the CM model underpredict the experimental data as shown in Fig. 3.14. The error between the predictions and experimental data is largest for the low Re and decreases slightly as Re is increased. However, this deviation is in no way related to inertial forces as $Re<<1$.

The magnitude of the error between predicted and experimental friction factors is much larger for LDPE than for LLDPE. In addition, there is a negative deviation of the LLDPE data from predicted friction factors and a positive deviation of the LDPE data from predicted friction factors. The differences in the shear viscosity behavior of LLDPE and LDPE, such as the magnitude of η and the degree of shear thinning, are fit well by the power law viscosity function incorporated into the capillary model developed by Christopher and Middleman. The deviations of the experimental data

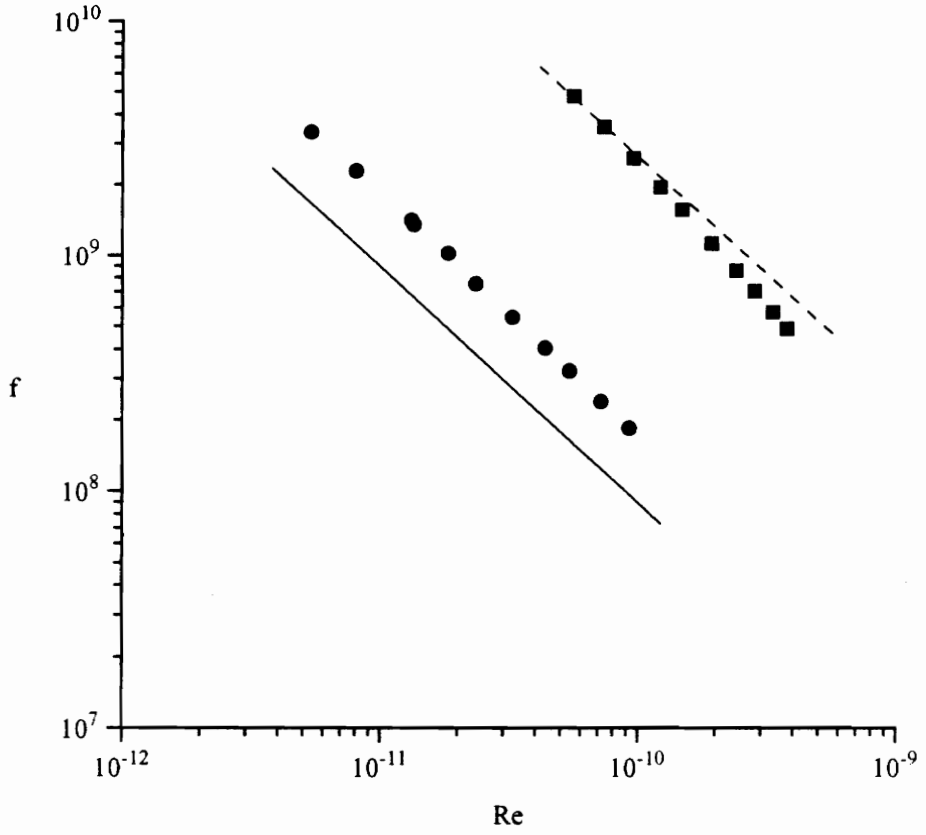

Fig. 3.14. Friction factor vs Reynolds number for LDPE and LLDPE flowing through a square array of cylinders. Symbols represent experimental data: LDPE (●); LLDPE (■). Lines represent predictions of capillary model of Christopher and Middleman: LDPE (——); LLDPE (- - - -).

shown in Fig. 3.14 from the capillary model predictions cannot be explained solely in terms of steady shear rheology, which is the only rheological property incorporated into the CM model.

The deviation of the predicted friction factors from experimental data shown in Fig. 3.14 is not systematic in that there is a negative deviation of the data from the predicted friction factor for LLDPE, and a positive deviation of the data from the predicted friction factors for LDPE. Thus, it seems clear that there are rheological properties in addition to the steady shear viscosity which must be incorporated into modeling of flow of viscoelastic fluids through periodic arrays of cylinders.

3.5.3 Predictions of Finite Element Calculations

In this section, the results of finite element calculations using the GNF constitutive equation with the BC viscosity function, the PTT model, and the RS model with the PSM damping function will be presented. The predictions of the pressure drop versus Deborah number (De) for LLDPE flowing through a bank of cylinders calculated using the finite element method (FEM) for the GNF model with the BC viscosity function and PTT model are shown in Fig. 3.15. In this case De is defined to be

$$De = \frac{\lambda v_\infty}{D}, \qquad (3.30)$$

where λ is the longest relaxation time of the fluid, v_∞ is the average superficial velocity of the fluid, and D is the diameter of a cylinder. In this form De represents the ratio of the longest relaxation time of the fluid to the average time that the fluid spends

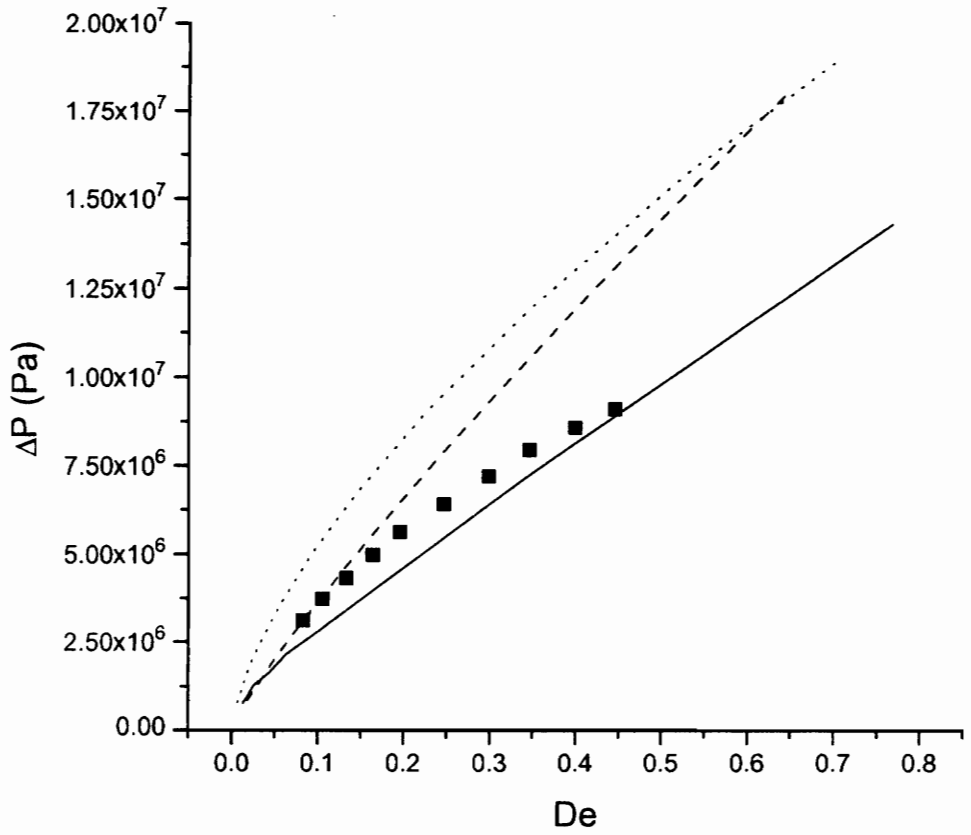

Fig. 3.15. Pressure drop versus De for LLDPE flowing through a bank of cylinders at 170°C. Symbols represent experimental data. Lines represent predictions of: capillary model (- - - - -); GNF model with BC viscosity function (·····); PTT model (——).

flowing past a single cylinder. The FEM calculations for the flow of LLDPE between cylinders were carried out using the mesh and boundary conditions discussed in section 3.4. The pressure drop that is calculated for the flow between a single pair of cylinders is assumed to apply additively to each cylinder pair encountered by the fluid in the flow direction. The validity of this assumption was verified by comparing the computed pressure drop through the bank of cylinders when flow between two pairs of cylinders was simulated to the pressure drop calculated when flow past a single cylinder was simulated. The calculated pressure drops when flow between a single pair of cylinders was simulated varied by less than 2% from the pressure drop calculated when flow between two pairs of cylinders was simulated, thus verifying the assumption for calculations involving LLDPE.

The pressure drop predicted by the GNF model with the BC viscosity function overpredicts the experimental data for LLDPE as shown in Fig. 3.15. This result is qualitatively similar to that of the CM model predictions which are also shown in Fig. 3.15. A converged solution to the flow problem for LLDPE using the RS model with the PSM damping function was not obtained and, hence, a comparison of the predictions to data is not available. The predictions of the PTT model provide the best agreement with the data shown in Fig. 3.15, although the predicted pressure drop is increasing more rapidly as a function of De for the highest De for which there is experimental data.

One possible cause of the difference in dependence of the computed pressure drop on De with increasing De for LLDPE may be attributed to the extensional viscosity predictions of the PTT model for LLDPE. The PTT model predictions of the extensional viscosity for LLDPE, shown in Fig. 3.12 exhibit a maximum at an extension rate of $2.5s^{-1}$, which occurs in the finite element calculations for De=0.34.

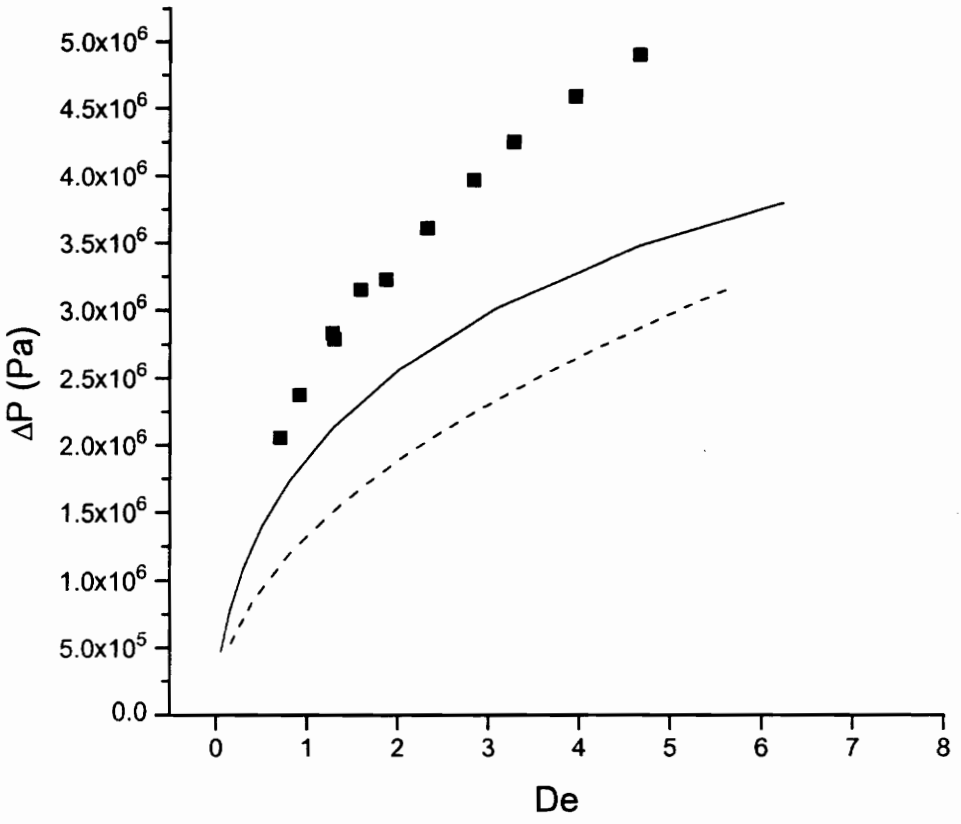

Fig. 3.16. Pressure drop versus De for LDPE flowing through a bank of cylinders at 170°C. Symbols represent experimental data. Lines represent predictions of: capillary model (- - - - -); GNF model with BC viscosity function (———).

Without experimental data at higher strain rates, it is not known whether LLDPE exhibits the strain rate hardening behavior predicted by the PTT model.

In summary, for LLDPE flowing through a periodic array of cylinders purely viscous models such as the CM capillary model and the GNF model both overpredict the pressure drop as a function of De. The pressure drop predictions of the PTT model are in agreement with the experimental data although the pressure drop is slightly underpredicted at low De, and the dependence of the pressure drop on De differs from the data for the higher flow rates (i.e. the predicted pressure drop is increasing faster than the experimental versus De). An explanation for the overprediction of the pressure drop by the GNF model and the basically correct predictions of the pressure drop by the PTT model will be discussed below after the results for LDPE flowing through a periodic array of cylinders have been presented.

The pressure drop versus De for LDPE predicted by finite element calculations using the GNF model with the BC viscosity function is shown in Fig. 3.16. The calculated pressure drop when flow between a single pair of cylinders was simulated varied by less than 2% from the pressure drop calculated when flow between two pairs of cylinders was simulated using the GNF model. The pressure drop predicted for LDPE using the GNF model with the BC viscosity function was lower than the experimental data, and qualitatively follows the same trend as the capillary model predictions, as was the case for LLDPE. Hence, one must consider the viscoelastic nature of the fluid.

The pressure drop versus De predicted by finite element calculations using the PTT and RS constitutive equations are shown in Fig. 3.17. The pressure drops calculated using the PTT model when flow between one pair and two pairs of cylinders were simulated are both shown in Fig. 3.17. For LDPE it was found that the

FEM calculations of the pressure drop using the PTT model for flow between one pair and two pair of cylinders were different. The pressure drop calculated for flow between a single pair cylinders is greater than that for flow between two pairs cylinders, indicating that fluid memory has an effect on the pressure drop in calculations for LDPE using the PTT model. The pressure drop calculated for flow between three pairs of cylinders was nearly identical to the pressure drop calculated for flow past two cylinders. Even when the effect of fluid memory is accounted for, the PTT model overpredicts the pressure drop of LDPE.

The pressure drop for LDPE calculated using the RS model with the PSM damping function, also shown in Fig. 3.17, underpredicts the experimental data and is qualitatively similar to the predictions by the GNF model with the BC viscosity function. This was an unexpected result because of the excellent fits obtained for the RS constitutive equation to the shear viscosity and extensional stress growth data for LDPE as well as predictions of transient shear behavior. The disagreement between the predicted pressure drop and experimental data despite the excellent fit of the rheological properties may be a result of the numerical technique used to solve the governing equations of the flow problem. As mentioned previously, the equations of continuity and momentum are decoupled from the constitutive equation in the numerical technique used here. Convergence of the solution is based on the difference of iterations of the velocity field. Because the viscoelastic extra stresses are very sensitive to the velocity field, small changes in the velocity may result in large changes in the extra stress. Thus the computed velocity field may only be a small perturbation from the initial velocity field, which is based on a purely viscous model.

Satisfactory agreement between numerical predictions of the pressure drop of LDPE flowing through a periodic array of cylinders and experimental data was not

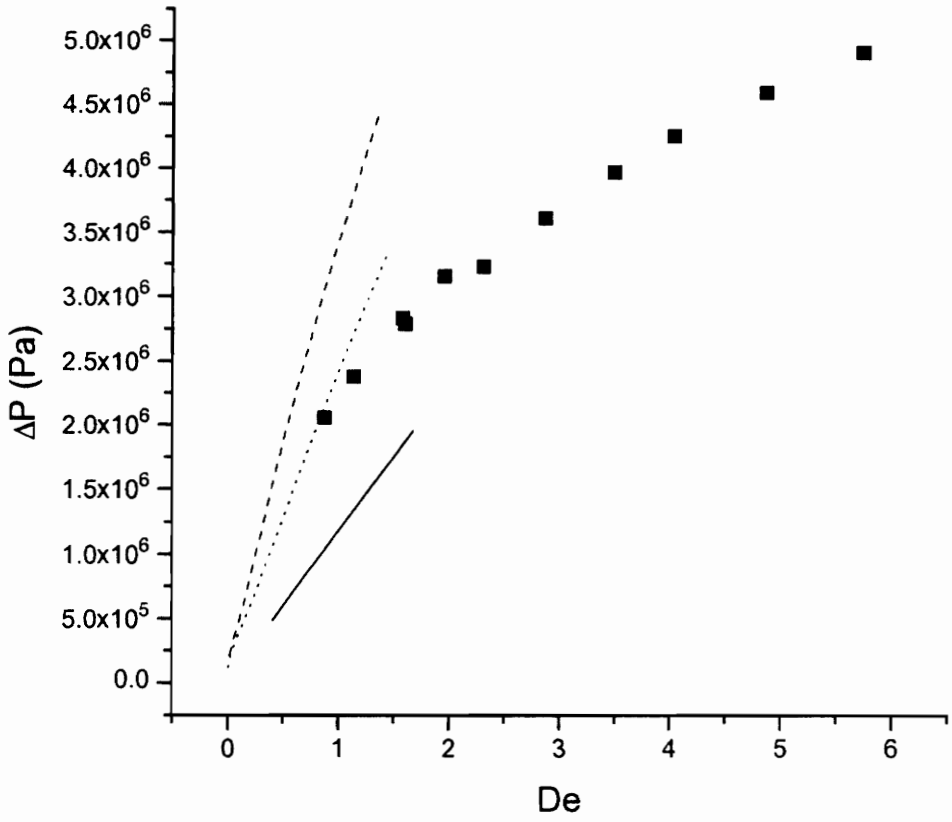

Fig. 3.17. Pressure drop vs De for LDPE flowing througha bank of cylinders at 170°C. The symbols represent experimental data. The lines represent predictions for: PTT model, one cylinder pair (- - - -); PTT model, two cylinder pair (·····); RS model with the PSM damping function (———).

obtained. There are three possible sources for the lack of agreement which will be discussed here: the fit of the constitutive equation to rheological data; the numerical technique; and the constitutive equation predictions in flow where deformation history has an effect on the rheology. The fit of the RS model to rheological data is very good so this is not expected to be a source of disagreement between predictions and data. The fit of the PTT model to rheological data is not as exact and is, therefore, investigated. In Fig. 3.18, the effect of λ and ε on the pressure drop for De=1.21 are shown. It can be seen that ε does not have a large impact on the predicted pressure drop, less than 20% for typical values of λ used for LDPE (4.1s in this paper). The dependence of the pressure drop on λ is practically negligible for typical values of λ used for LDPE for De=1.21. The parameter ξ has negligible effect on the predicted pressure drop (for $0<\xi<0.25$). Hence, the values of the parameters of the PTT model adjusted to fit rheological data are not a likely source of the disagreement between predicted pressure drops and experimental data for LDPE.

As mentioned above, the numerical technique used to obtain a solution to the governing equations is a possible source of error. The numerical technique used with the PTT model has also been used to simulate the flow of LLDPE and LDPE past a cylinder in a planar channel [34]. It was found that numerical predictions of the stress field using the PTT model in conjunction with the 4x4SU method were similar to experimental data. Errors resulting from the numerical technique cannot be ruled at this time but the results of Ref. 34 suggest that the numerical techniques used here may not be the primary reason for the disagreement between the predicted pressure drop and experimental data for LDPE.

The overprediction of the pressure drop for LDPE using the PTT model may be due to deformation history effects which are not correctly predicted by the

constitutive equation. It has been shown that the flow behavior of LDPE changes as it flows past cylinders in a channel, indicating that the deformation history imposed on the fluid by a cylinder may have an effect on the flow past a cylinder further downstream [34]. As mentioned previously, LDPE consists of highly branched polymer molecules. The high degree of branching may result in a reentanglement time which is much longer than the relaxation times used for the PTT model. This phenomenon is discussed in chapter 4 [34].

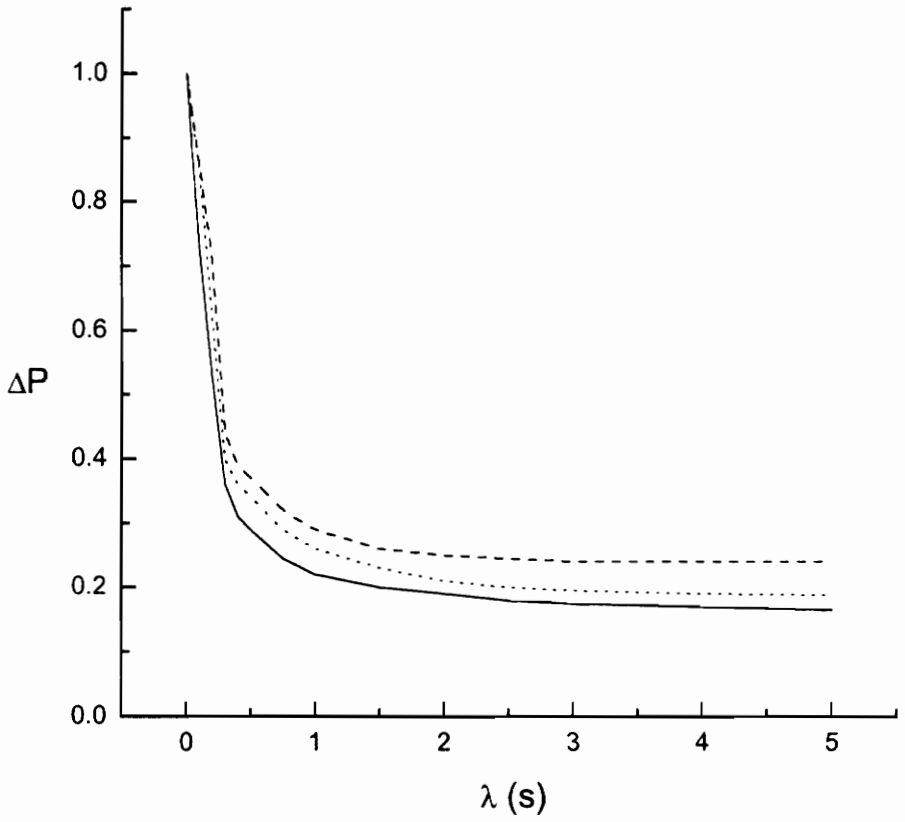

Fig. 3.18. Normalized pressure drop versus λ predicted by the PTT model for flow through a bank of cylinders for De=1.41: (- - - - -) ε=0.01; (·····) ε=0.10; (———) ε=1.0.

3.5.4 Stress Predictions

The predictions for the pressure drop versus De calculated using the FEM for both viscous and viscoelastic constitutive equations have been presented. In this section, kinematics and stresses calculated using the FEM will be discussed in order to determine the rheological properties which, at least in part, cause the pressure drop to be overpredicted for LLDPE and underpredicted for LDPE by purely viscous constitutive equations (i.e. GNF model), and more accurately predicted by the PTT constitutive equation.

The flow along the plane of symmetry between cylinders, designated as line AB in Fig. 3.8(a), is a planar extensional flow [24]. The computed flows are steady in the Eularian sense in that the velocity and stresses are constant with respect to time. However, the flow is unsteady in the Lagrangian sense. Fluid elements traveling along the line AB experience extension and compression as they pass through contractions and expansions and stresses vary with time following a fluid element. Finite element calculations using purely viscous constitutive equations and viscoelastic constitutive equations would be expected to predict different stresses and kinematics along the line AB due to the differences in predicted time dependent rheological behavior and extensional viscosity behavior. It would be expected that a constitutive equation such as the PTT model that correctly predicts stress growth and stress relaxation behavior would predict the stress behavior along line AB better than a purely viscous model.

The extension rate ($\dot{\gamma}_{11}$) and extensional stress (τ_{11}), normalized by their maximum calculated values, predicted for the flow of LLDPE at De=0.34 using the GNF model with BC viscosity function are shown in Fig. 3.19. This plot is typical of all simulations using the GNF model in this paper. The stress predicted by the GNF

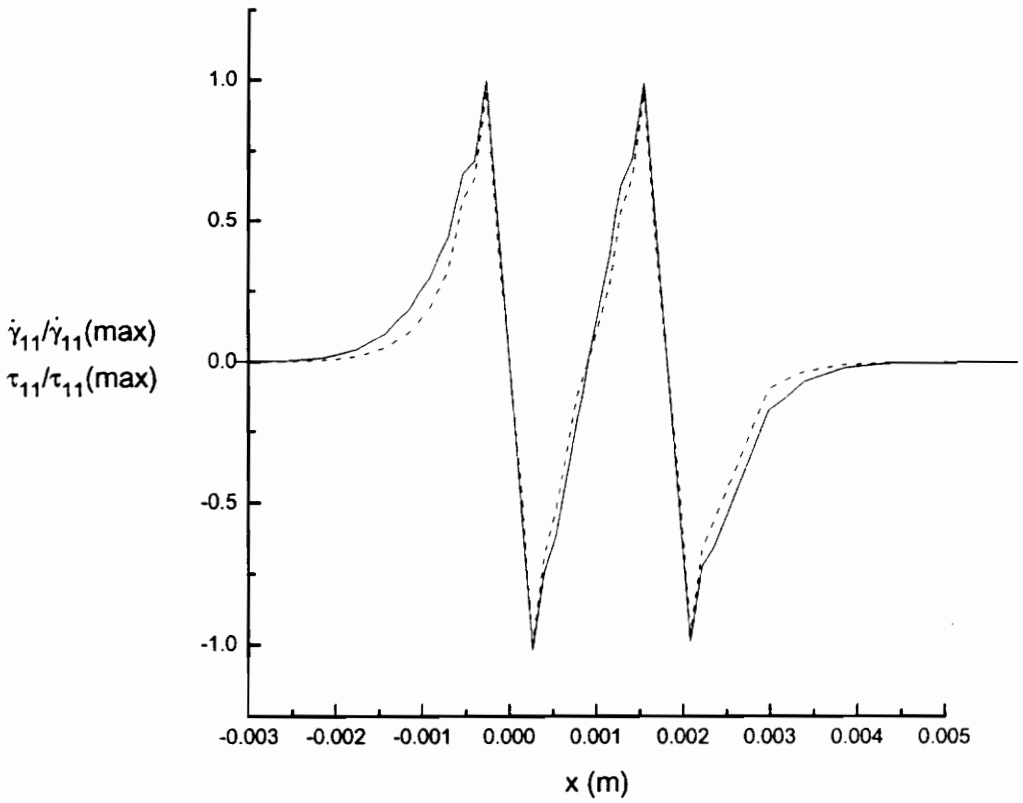

Fig. 3.19. Normalized planar extension rate, $\dot{\gamma}_{11}$ (———), and stress, τ_{11} (- - - - -), along the centerline bewteen cylinders (line AB in Fig. 8a) calculated using GNF model with Bird-Carreau viscosity function for De=0.85. Cylinder centers located at x=0.0 and x=1.36×10^{-3}m.

model is always proportional to the instantaneous value of the deformation rate. Thus τ_{11} is always proportional to the instantaneous value of $\dot{\gamma}_{11}$ at the point on line AB being examined. If the flow along line AB is taken to be periodic, with two periods shown in Fig. 3.19, then it is seen that τ_{11} is in phase with $\dot{\gamma}_{11}$ along line AB.

The extension rate and extensional stress predicted by the PTT model for LLDPE along the plane of symmetry (line AB in Fig. 3.8(a)) are shown in Fig. 3.20. The extensional stress predicted by finite element calculations, τ_{11}, is normalized by the steady state value of τ_{11} calculated by the PTT model using the instantaneous value of $\dot{\gamma}_{11}$. There are two major differences between the behavior of τ_{11} predicted by the GNF constitutive equation and the PTT constitutive equation along the plane of symmetry. The first difference is the magnitude of τ_{11} calculated by the PTT model relative to the steady state value. The extensional stress calculated using the PTT model does not reach its steady state value. The second difference is the "lag" of the stress behind the strain rate. The maxima in the stress occur after the maxima of the strain rate. This may suggest that the time dependent rheology predicted by the PTT constitutive equation for LLDPE serves to decrease the calculated pressure drop relative to a purely viscous constitutive equation (i.e. GNF model), which does not predict time dependent behavior.

The extensional stress and extension rate predicted by the PTT model for LDPE are shown in Fig. 3.21 and are normalized in the same method used previously for LLDPE. The two observations discussed for LLDPE, the maximum extensional stress relative to the steady state value and the lag of stress behind the strain rate, are more pronounced with LDPE, probably due to the longer relaxation time used in the PTT constitutive equation for LDPE. The ratio of the maximum predicted value of τ_{11} to the maximum steady state value of τ_{11} for LDPE is 0.18, while the same ratio of

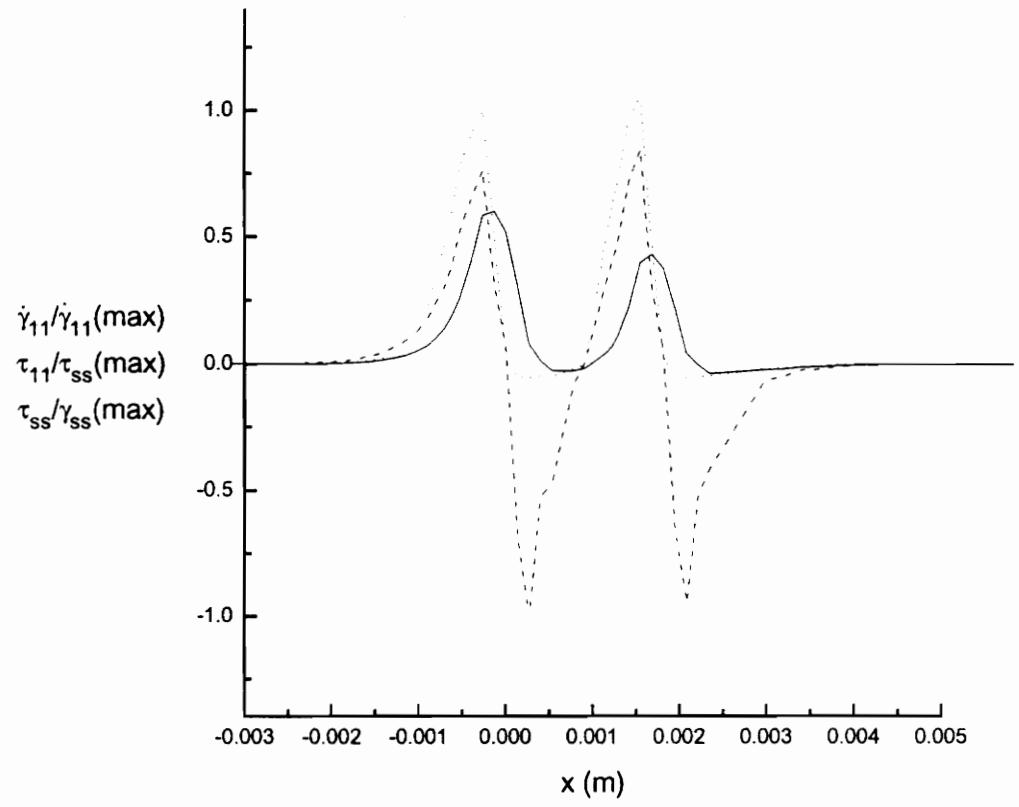

Fig. 3.20. Normalized planar extension rate $\dot{\gamma}_{11}$ (- - - -), stress τ_{11} (———), and steady state stress τ_{ss} ( ) predictions for LLDPE along the centerline between the cylinders (line AB in Fig. 8a) using the PTT model for De=.47. Cylinder centers are located at x=0.0 and x=1.36x10^{-3}m.

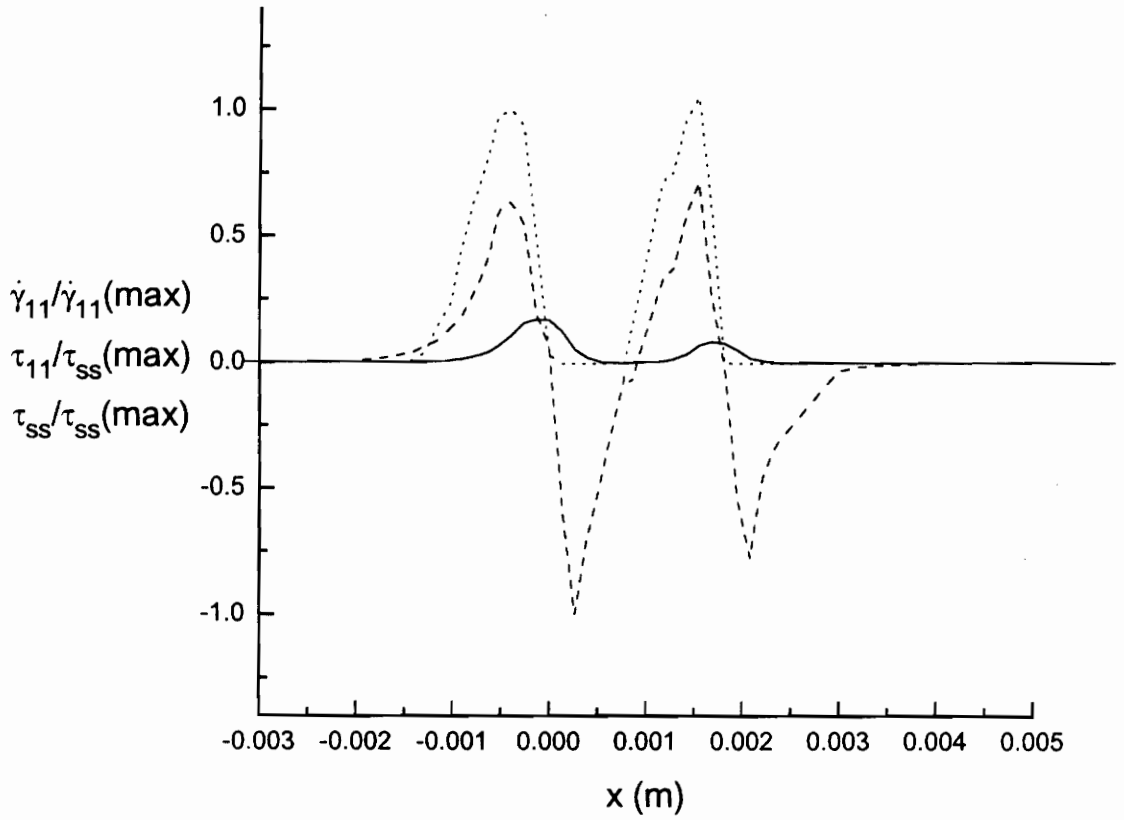

Fig. 3.21. Normalized planar extension rate $\dot{\gamma}_{11}$ (·····), stress τ_{11} (———), and steady state stress τ_{11} (- - - -) predictions for LDPE along the centerline between the cylinders (line AB in Fig. 8a) using the PTT model for De=4.2. Cylinder centers are located at x=0.0 and x=$1.36\text{x}10^{-3}$m.

the stresses for LLDPE was 0.60 at the same flow rate, which on first inspection seems to indicate that large extensional stresses are not predicted to occur for LDPE. However, by examining the absolute value of stresses, quantitative differences in the flow behavior along the plane of symmetry predicted by the PTT constitutive equation for LLDPE and LDPE may be seen more clearly. Despite the smaller ratio of the predicted extensional stress to the steady state value calculated for LDPE, the magnitude of the predicted stress is quite large compared to that predicted for LLDPE for the same flow rate. A plot of the instantaneous value of the extensional stress τ_{11} is shown in Fig. 3.22 for LLDPE and LDPE at the same flow rate. It can be seen in Fig. 3.22 that the large degree of strain rate hardening behavior predicted for LDPE by the PTT constitutive equation results in large values of τ_{11}, even though the time dependent properties tend to decrease the stress relative to the steady state value as shown in Fig. 3.21. Hence, despite the longer relaxation time associated with LDPE, large extensional stresses still develop as a result of the extensional strain rate hardening behavior of LDPE.

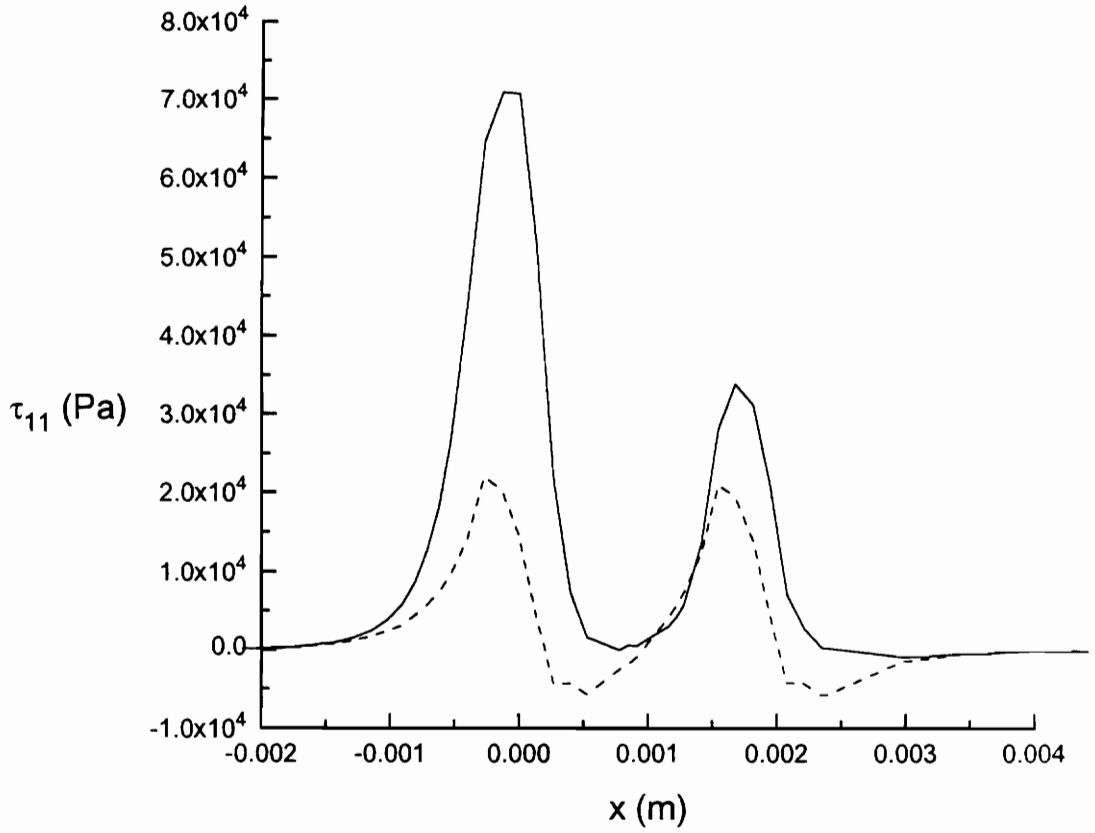

Fig. 3.22. τ_{11} versus x along the line AB in Fig. 8(a) for LLDPE (- - - - -) and LDPE (———) at the same flow rate.

3.6 Conclusions

In this chapter measurements of the pressure drops of a LLDPE and a LDPE polymer melt flowing through a periodic array of cylinders have been compared to numerical predictions. The numerical predictions consisted of finite element calculations which incorporated the generalized Newtonian fluid constitutive equation with the Bird-Carreau viscosity function, the Phan-Thien and Tanner constitutive equation, and the Rivlin-Sawyers constitutive equation with the Papanastasiou, Scriven, and Macosko damping function. The results indicate that purely viscous models are not adequate for predicting the pressure drop of LLDPE or LDPE polymer melts flowing through a bank of cylinders.

It has been shown in this chapter that for flow through a periodic array of cylinders, time dependent rheological behavior and extensional viscosity behavior must be described well by the constitutive equation used if numerical predictions of the pressure drop are to agree with experimental data. The PTT constitutive equation and the RS constitutive equation with the PSM damping function were shown to describe the time dependent rheological behavior well in simple flows. Purely viscous models generally are only able to describe the steady shear viscosity of a fluid well. The agreement between numerical predictions of the pressure drop and experimental data was best for the finite element calculations using the PTT model.

The pressure drops predicted by finite element calculations using the GNF constitutive equation with the Bird-Carreau viscosity function were qualitatively in agreement with the predictions of the capillary model of Christopher and Middleman in that both overpredicted the measured pressure drops for LLDPE. The predictions of the finite element calculations using the PTT constitutive equation were in agreement

with the measured pressure drops for LLDPE. The reason that the agreement between the predicted pressure drops of the finite element calculations using the PTT constitutive equation and experimental data was best appears to be related to time dependent rheological behavior.

The pressure drops predicted by finite element calculations using the GNF constitutive equation with the Bird-Carreau viscosity function were in agreement with the predictions of the capillary model of Christopher and Middleman in that both underpredicted the measured pressure drops for LDPE. The predictions of the finite element calculations using the PTT constitutive equation were in better agreement with the measured pressure drops for LDPE than purely viscous models, but overpredicted the pressure drop. For LDPE it was found that the pressure drop over two cylinders was required for calculating the pressure drop over the bank of cylinders whereas for LLDPE only calculations over one cylinder was required. This was attributed to the longer relaxation time for LDPE.

The finite element calculations using the RS constitutive equation did not provide adequate predictions for LLDPE or LDPE flowing though a periodic array of cylinders. Converged solutions were not obtained for the finite element calculations using the RS constitutive equation to simulate the flow of LLDPE despite mesh refinement. This is likely due to the short relaxation time of LLDPE, which in contrast to finite element calculations using differential constitutive equations, makes the calculations more difficult. In the numerical scheme used, the stresses are calculated by integration of the kinematics along streamlines, and if the stresses along a streamline relax on a scale finer than the finite element mesh used, errors may result and converged solutions not be obtained. The predictions of finite element calculations using the RS constitutive equation for the pressure drop for LDPE were

qualitatively similar to the purely viscous model simulations. This is a somewhat surprising result because of the excellent fit of the RS model to the rheological properties. This result may be due to the decoupled numerical scheme employed to solve flow problems using integral constitutive equations.

In order to improve the predictions of the pressure drop of LDPE flowing through a bank of cylinders, a constitutive equation which correctly predicts the dependence of the fluid rheology on deformation history is needed. In addition, use of the PTT model with a spectrum of relaxation times will result in a better fit of the rheological properties, and possibly better predictions of the pressure drop. Incorporation of multiple relaxation times into computations involving a differential constitutive equation are very computationally intensive because in general there are 3n+3 unknowns for n relaxation times (for a 2D flow). However, with faster computers becoming available, this may be a possibility in the future.

Literature Cited

1. H. Darcy, Les fontaines publiques de la ville de Dijon Paris:Delmont, 1856.
2. Bird, R.B., W.E. Stewart, and E.N. Lightfoot, *Transport Phenomena*, Wiley, N.Y. (1960).
3. Nutting, P.G., "Flow Through Inhomogeneous Media," *Bull. Amer. Ass. Petrol. Geol.*, **14**, 1337 (1930).
4. Wyckoff, R.D., "Ideas Concerning Flow Through Granular Beds," *Rev. Sci. Instr.*, **4**, 394 (1933).
5. Carmen, P.C., "The Determination of the Specific Surface of Powders," *J. Soc. Chem. Ind. Trans.*, **57**, 225 (1938).
6. Sadowski, T.J., and R.B. Bird, "Non-Newtonian Flow Through Porous Media. I. Theoretical," *Trans. Soc. Rheol.*, **9**, 243 (1965).
7. Christopher, R.H., and S. Middleman, "Power law flow through a packed tube," *Ind. Eng. Chem. Fund.*, **4**, 422 (1965).
8. Kemblowski, Z., and M. Michniewicz, "A new look at laminar flow of power law fluids through granular beds," *Rheol. Acta.*, **18**, 730 (1979).
9. Sheffield, R.A., and A.B. Metzner, "Flow of Nonlinear Fluids Through Porous Media," *AIChE J.*, **22**, 736 (1976).
10. Wissler, E.H., "Viscoelastic Effects in the Flow of Non-Newtonian Fluids Through a Porous Medium," *I. & E.C. Fund.*, **10**, 411 (1971).
11. Durst, F., R. Haas, and W. Interthal, "The Nature of Flows Through Porous media," *J. Non-Newt. Fluid Mech.*, **22**, 169 (1987).
12. Bird, R.B., C.F. Curtiss, R.C. Armstrong, and O. Hassager, *Dynamics of Polymeric Liquids, Vol. 2*, Wiley, N.Y. (1987).
13. Chmielewski, C., and K. Jayaraman, "The effect of polymer extensibility on crossflow of polymer solutions through cylinder arrays," *J. Rheol.*, **36**, 1105 (1992).
14. Boger, D.V., "A highly elastic constant-viscosity fluid," *J. Non-Newt. Fluid Mech.*, **3**, 87 (1977).
15. Skartsis, L., J.L. Kardos, and B. Khomami, "Viscoelastic Flow in Porous Media," *Poly. Eng. Sci.*, **32**(4), 221 (1992).
16. Talwar, K., and B. Khomami, "Applications of higher order finite element methods to viscoelastic flow in porous media," *J. Rheol.*, **36**, 1377 (1992).
17. Souvaliotis, A., and A.N. Beris, "Applications of domain decomposition spectral methods to viscoelastic flow in porous media," *J. Rheol.*, **36**, 417 (1992).
18. Sadowski, T.J., and R.B. Bird, "Non-Newtonian Flow Thorugh Porous Media. II. Experimental," *Trans. Soc. Rheol.*, **9**, 251 (1965).
19. Larson, R.G., "Flow-induced mixing, demixing, and phase transitions in polymeric fluids," *Rheol. Acta*, **31**, 497 (1992).
20. van Egmond, J.W., and G.G. Fuller, "Concentration Fluctuation Enhancement in Polymer Solutions by Extensional Flow," *Macromolecules*, **26**, 7182 (1993).

21. Chmielewski, C., and K. Jayaraman, "Elastic Instability in crossflow of polymer solutions through periodic arrays of cylinders," *J. Rheol.*, **36**, 301 (1993).
22. Munstedt, H, "New Universal Extensional Rheometer for Polymer Melts," *Trans. Soc. Rheol.*, **23**, 421 (1979).
23. White, S.A., A.T. Gotsis, and D.G. Baird, "Review of the Entry Flow Problem," *J. Non-Newt. Fl. Mech.*, **24**,121 (1987).
24. Bird, R.B., R.C. Armstrong, and O. Hassager, *Dynamics of Polymeric Liquids, Vol. 1*, Wiley, N.Y. (1987).
25. Larson, R.G., *Constitutive Equations for Polymer Melts and Solutions*, Butterworth, Boston (1988).
26. Phan-Thien, N., and R.I. Tanner, "A new constitutive equation derived from network theory," *J. Non-Newt. Fluid Mech.*, **2**, 353 (1977).
27. Phan-Thien, N., "A Nonlinear Network Viscoelastic Model," *J. Rheol.*, **22**, 259 (1978).
28. Papanastasiou, A.C., L.E. Scriven, and C.W. Macosko, An Integral Constitutive Equation for Mixed Flows: Viscoelastic Characterization," *J. Rheol.*, **27**, 387 (1983).
29. Orbey, N., and J.M. Dealy, Determination of relaxation spectrum from oscillatory shear data," *J. Rheol.*, **35**(6), 1035 (1991).
30. Babuska, B., *Numer. Meth.*, **16**, 322 (1971).
31. Marchal, J.M., and M.J. Crochet, "A New Mixed Finite Element for Calculating Viscoelastic Flow," *J. Non-Newt. Fluid Mech.*, **26**, 77 (1987).
32. R.I. Tanner, H. Jin, *J. Non-Newt. Fluid Mech.*, **41**, 171 (1991).
33. Legat, V., and J.M. Marchal, On the stability and accuracy of fully coupled finite element techniques used to simulate the flow of differential viscoelastic fluids," *J. Rheol.*, **36**, 1325 (1992).
34. Hartt, W.H., "Flow of Viscoelastic Fluids through Periodic Arrays of Cylinders: An Experimental and Numerical Investigation," Ph.D. Diss., Virginia Polytechnic Institute and State University (1995).
35. Dupont, S., J.M. Marchal, and M.J. Crochet, "Finite element simulation of viscoelastic fluids of the integral type," *J. Non-Newt. Fluid Mech.*, **29**, 81 (1988).

4.0 The Confined Flow of Viscoelastic Fluids Past a Cylinder in a Planar Channel[1]

Preface

This paper is concerned with the comparison of the results of numerical simulation of confined flow past a cylinder to birefringence data for two polymer melts. The Phan-Thien and Tanner (PTT) constitutive equation and the Rivlin-Sawyers constitutive equation with the Papanastasiou, Scriven, and Macosko (PSM) damping function were each fit to the shear viscosity and extensional viscosity data of both linear low-density polyethylene (LLDPE) and low-density polyethylene (LDPE) melts to determine the values of the model parameters. Finite element calculations were carried out using the 4x4SUPG and 4x4SU methods for the PTT model and the method developed by Dupont et al. for the RS model. Isochromatic birefringence patterns calculated from the predicted stress field and the stress-optic law were compared to birefringence data. Agreement was found between the birefringence data and the numerical predictions, except in the immediate vicinity of the cylinder surface. Large extensional stresses were observed and predicted along the centerline downstream of the cylinder for LDPE. This behavior was not observed or predicted for LLDPE. Stress fields obtained from birefringence measurements for LDPE flowing past three cylinders in a channel indicate an effect of deformation history on the flow behavior of LDPE. It is shown that the PTT model does not correctly predict the rheological behavior of LDPE as a function of shear history because the time scale of structural recovery is much longer than the relaxation time associated with viscoelasticity.

[1] This chapter is being submitted to *The Journal of Non-Newtonian Fluid Mechanics*.

4.1 Introduction

Flow past a cylinder in a plane channel has been designated as a benchmark problem for numerical computations of viscoelastic flows [1,2,3]. A schematic of the geometry associated with the flow past a cylinder in a plane channel is shown in Fig. 4.1. The flow past a cylinder in a planar channel provides a more convenient geometry for flow visualization and birefringence measurements due to the fact that it is a 2D flow while the sphere-in-a-tube benchmark is a 3D flow.

Early studies of the flow of viscoelastic fluids past a cylinder focused on the measurement of the streamlines and the drag on the cylinder. In addition, the early studies focused on geometries where the cylinder radius was small relative to the channel height. Ultman and Denn [4] observed that the streamlines for an aqueous solution of polyacrylamide flowing past a cylinder in a channel were shifted upstream relative to the Newtonian case, where the streamlines are symmetric about the cylinder. Manero and Mena [5] and Dhahir and Walters [6] observed that for low Deborah numbers (De), the streamlines for several polymer solutions flowing past a cylinder in a channel shifted downstream as De increased [5]. Manero and Mena also observed that for De~1, the streamlines began to shift upstream with increasing De relative to the Newtonian case [5]. The results of Manero and Mena suggest that the non-Newtonian streamlines presented by Ultman and Denn correspond to De>1, although details were not given by Ultman and Denn.

The upstream shift of the streamlines and a corresponding increase in the drag on the cylinder have been associated with a mathematical change of type in the governing equations that occurs in moderate Reynolds number (Re) flows when fluid elasticity is present [4,7,8]. McKinley et al. [22] performed laser Doppler velocimetry

(LDV) measurements on a Boger fluid flowing past a cylinder in a planar channel with R/H=0.5. They observed that the streamlines shifted downstream with increasing De until De≥1.3, where a transition to a steady three-dimensional flow was observed to occur. The transition to three-dimensional flow observed by McKinley et al. occurred at low Re and thus was not attributed to a change of type in the governing equations.

Baaijens et al. [19] studied the flow of a solution of polyisobutylene (PIB) in polybutene (C14) past a cylinder in a plane channel with R/H=0.5. Using LDV measurements and flow birefringence, Baaijens et al. compared the flow of the PIB/C14 solution at De=0.216 to numerical simulations using the Phan-Thien and Tanner (PTT) constitutive equation. The values of the adjustable parameters in the PTT model were determined by a fit of the model to the steady shear viscosity and dynamic viscosity. Transient material functions and extensional viscosity behavior was not considered. Good agreement between the measured and numerically predicted velocity data was obtained. However, the agreement between the measured stresses in the wake of the cylinder and numerically predicted stresses was not good.

The first objective of this paper is to assess the role played by the constitutive equation in the numerical simulation of flow past a cylinder in a planar channel. In particular it is desired to know whether the flow past a cylinder of polymer melts with significantly different relaxation times and extensional viscosity behavior can be accurately predicted. To accomplish this objective two constitutive equations are considered: the Phan-Thien and Tanner (PTT) constitutive equation and Rivlin-Sawyers (RS) constitutive equation with the Papanastasiou, Scriven, and Macosko (PSM) damping function. The PTT constitutive equation and the RS constitutive equation with the PSM damping function have been shown to describe well the

rheological behavior of LLDPE and LDPE in steady shear flows, transient shear flows, and transient extensional flows [9].

The second objective of this paper is to determine the stress field for two different viscoelastic fluids with different rheological properties flowing past a cylinder in a planar channel at 170 C. LLDPE and LDPE were chosen because these two polymer melts have similar zero-shear viscosities. However, the onset of shear thinning occurs at a lower shear rate for LDPE than for LLDPE, suggesting that LDPE has a longer relaxation time. Furthermore, LDPE exhibits extensional strain hardening behavior while LLDPE does not. Comparison of numerical predictions to experimental data is necessary because no analytical solution to the flow problem considered here is available. To analyze LLDPE and LDPE flowing past a cylinder in a planar channel, flow birefringence measurements are carried out to determine the stress field, except in the immediate vicinity of the cylinder wall where the fringes are too close together to be measured by full-field optical techniques.

Numerical simulations are carried out using the finite element program Polyflow (Polyflow s.a. ver. 3.1.1). The 4x4SUPG (streamline upwinding/Petrov Galerkin) and 4x4SU (streamline upwinding) methods [10] are used to simulate the flow with the PTT constitutive equation and the numerical technique developed by Dupont et al. is used to simulate the flow with the RS constitutive equation with the PSM damping function [11]. It has been shown that for the case of additive diffusion, which arises in the SU method, smooth solutions can be computed but may not approximate well the fine structure of stress and velocity fields in boundary layers and near singularities [12,13]. Further, it is not known how these local numerical approximations affect the solution far away from boundary layers and singularities. The results of calculations using the 4x4SUPG method will be used in this work as a

comparison for results using the 4x4SU method in an attempt to assess the accuracy of the 4x4SU method.

Finally, the effect of fluid memory on the flow of LDPE past three cylinders placed in a series along the centerline of a planar channel is investigated using flow birefringence. This is accomplished by spacing the cylinders in the channel so that the average residence time of fluid elements between cylinders is longer than the longest relaxation time of LDPE at low flow rates. For higher flow rates, the average residence time between cylinders is shorter than the longest relaxation time of LDPE. Thus by varying the flow rate, or De, the effect of fluid memory on the flow downstream of the first cylinder could be investigated.

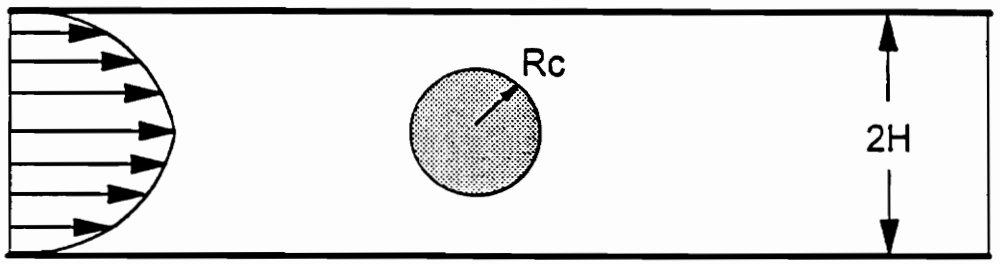

Fig. 4.1. Schematic of flow past a cylinder in a planar channel.

4.2 Experimental Methods

4.2.1 Materials and Rheological Characterization

LLDPE (NTA-101) supplied by Mobil and LDPE (NPE-953) supplied by Quantum Chemical were the polymers used in this study. LLDPE has a molecular topology consisting of a linear backbone with short, low molecular weight side-chain branches. NTA-101 has a weight average molecular weight (M_W) of 110,000 and a polydispersity index of 4.0. LDPE is a highly branched polymer with long, high molecular weight side-chain branches. NPE-953 has a M_W of 116,000 and a polydispersity index of 9.1.

For both polymer melts the shear viscosity (η) was measured for shear rates ranging from 0.01 to 4.641 s^{-1} in a nitrogen environment using the RMS-800 with a cone and plate geometry. The cone angle was 0.1 rad and the plate diameter was 2.54 cm. For shear rates above approximately 5.0s^{-1}, steady shear flow measurements were not possible due to loss of melt from between the cone and plate. Further characterization of the shear properties in the cone and plate geometry was obtained using dynamic oscillatory measurements. The complex viscosity (η^*), storage modulus (G'), and the loss modulus (G") were measured for angular frequencies (ω) ranging from 0.1 to 100 rad/s.

To obtain the shear viscosity for higher shear rates the Instron Capillary Rheomter was used. Three capillaries with a diameter of 6.86×10^{-4}m and L/D ratios of 12.5, 37.1, and 75.1 were used for measurements performed at a temperature of 170^{o}C. Using the Rabinowitsch correction to calculate the wall shear rate from the apparent shear rate and the Bagley correction for entrance pressure losses, the shear

viscosity as a function of shear rate was calculated from pressure drop and flow rate data by well known methods [15]. Shear rates up to 100 s^{-1} are reported here.

Jump strain tests were carried out using the RMS-800 with the cone and plate geometry, also at a temperature of 170°C. Step strains ranging from 0.1 to 40 percent were used. Stress measurements were taken from 0.01s after the strain was imposed until the stress decayed to less than 1% of the maximum value.

Double step shear rate tests were carried out using the RMS-800 with the cone and plate geometry in a nitrogen environment, also at a temperature of 170°C. In this type of experiment, a sample was sheared at a constant rate, $\dot{\gamma}_0$, for time, t_s, after which shear was stopped for a rest time, t_r, and then the sample was sheared again at a constant rate, $\dot{\gamma}_0$. The magnitude of the stress overshoot before and after the rest time was the quantity of primary interest.

Uniaxial stress growth measurements were carried out using a Rheometrics Extensional Rheometer (Model RER 9000) which is based on the Munstedt design [22]. In this rheometer, a molded cylinder of polymer is suspended in a heated oil bath between a fixed arm and a mobile arm. The density of the oil (Dow Corning Type 710) and the polymer are matched at the test temperature of 170°C so that there are no buoyancy effects. The polymer sample is then deformed at a constant extension rate and the force measured by a transducer. Extensional stress growth data was obtained for extension rates ranging from 0.020 to 0.20 s^{-1} at 170°C. Calculations of the extensional stress and viscosity were carried out by well known procedures [21].

4.2.2 Flow System

The polymer was fed to a slit die by means of an extruder-gear pump arrangement. The polymer was plasticated in a Killion 25.4 mm diameter extruder and

then fed to a gear pump (Zenith Model HPB-5556) from which it was metered to the slit die. The gear pump was utilized in order to minimize pressure and flow rate oscillations.

The slit die consisted of two symmetrical halves which, when bolted together, formed a channel 25.4 mm wide and 2.54 mm high, resulting in an aspect ratio of 10.0. It has been shown that the ratio of slit width to height should be at least 10.0 for the flow in a slit to be essentially two-dimensional [14].

A cylinder was placed in holes machined in quartz viewing windows placed on both sides of the slit. The diameter of the cylinder placed in the slit was 1.5875mm (1/16") and the ratio of the cylinder radius (R_c) to the slit height (2H) was 0.625. The ratio of 0.625 was used because it is similar to the spacing of cylinders encountered in our studies performed using a periodic array of cylinders [9]. For the experiments performed with three cylinders placed along the centerline of the slit, the spacing between cylinders was 3.175mm (1/8") from center to center.

4.2.3 Flow Birefringence

In this study, birefringence methods were used to determine the first principle stress difference $(\sigma_1 - \sigma_2)$ in the polymer melt flowing past a cylinder. In the stress-optic law, birefringence measurements are related to the first principle stress difference by the relation

$$N = \frac{WC}{\lambda'}(\sigma_1 - \sigma_2), \qquad (4.1)$$

where N is the fringe order, W is the slit width, λ' is the wavelength of the light used, and C is the stress-optic coefficient taken to be 2.1×10^{-9} Pa^{-1} for LLDPE and $2.0 \times 10^{-}$

^{9} Pa^{-1} for LDPE [14]. Full order isochromatic fringes were measured resulting in integer values of N (N=0,1,2,...).

The optical setup used to measure the isochromatic birefringence patterns is shown in Fig. 4.2. The setup consisted of a laser light source (Spectra Physics model 155, λ'=632.9 nm), 10X lens, collimator, two combined polarizer 1/4 wave plate filters (Oriel circular film polarizer), and a video camera (Panasonic WV-3100). The polarizer and analyzer were crossed in order to obtain the full order fringe values (dark field). A video camera was used so that any time dependent flow patterns that might occur could be recorded.

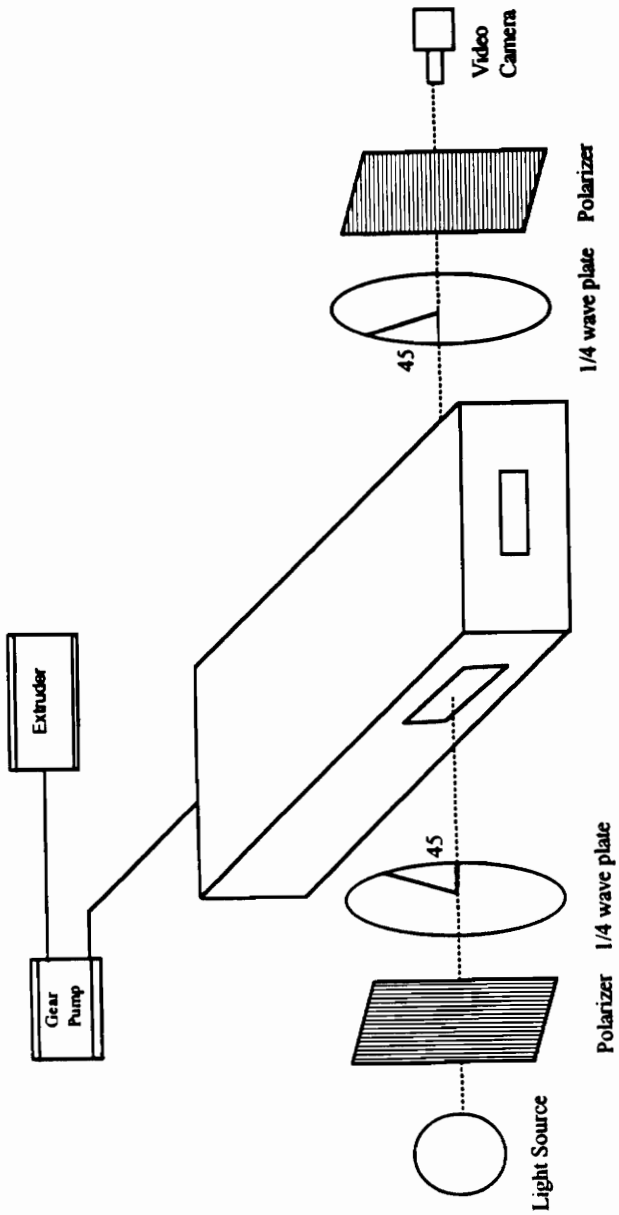

Fig. 4.2. Schematic of flow system and optical setup.

4.3 Numerical Methods

4.3.1 Finite Element Method

For the flow past a cylinder in a plane channel, the governing equations are the equations of continuity and momentum and the constitutive equation. When inertial terms and body forces such as gravity are neglected, these equations become in component form, respectively,

$$v_{i,i} = 0, \tag{4.2}$$

$$\tau_{ij,j} - P_{,i} = 0, \text{ and} \tag{4.3}$$

$$h\left(\tau_{ij}, \dot{\gamma}_{ij}, v_i, t, \ldots\right) = 0, \tag{4.4}$$

where v_i are components of the velocity vector, τ_{ij} are components of the extra stress tensor, P is the isotropic pressure, $\dot{\gamma}_{ij}$ are components of the rate of deformation tensor, t is the time, and h is a differential or integral operator. In this case, a tensile stress is taken as positive.

In this study the finite element program Polyflow (Polyflow s.a., ver. 3.1.1) was used to solve Eqs. (4.2-4). The 4x4SUPG and 4x4SU methods developed by Marchal and Crochet [10] are both used in this work to solve the governing equations where the PTT constitutive equation is used. Both of these methods use a coupled approach where the continuity equation, momentum equation, and constitutive equation are solved simultaneously in their discretized forms. The continuity equation and momentum equation are discretized using the Galerkin principle resulting in

$$\int_{\Omega} \pi_j \left[\nabla \cdot \underline{v}^a\right] d\Omega = 0 \text{ and} \tag{4.5}$$

$$\int_{\Omega} \nabla\psi_i^T \cdot \left[-p^a \underline{\underline{\delta}} + \eta_2 \underline{\underline{\dot{\gamma}}}^a + \underline{\underline{\tau}}_1^a\right] d\Omega = \int_{\partial\Omega} \psi_j \underline{\underline{\sigma}}^a \cdot \underline{n} ds, \qquad (4.6)$$

where ψ is a biquadratic shape function for the velocity, π is a bilinear shape function for the pressure, and the superscript "a" refers to the element value. The discretized forms of the constitutive equation are different for the SU and SUPG methods. The discretized form of the PTT model for the SUPG method is

$$\int_{\Omega} \phi_i \left[H\left(tr\underline{\underline{\tau}}_1^a\right)\underline{\underline{\tau}}_1^a + \lambda \underline{\underline{\tau}}_{1(1)}^a + \frac{\lambda\xi}{2}\left\{\underline{\underline{\dot{\gamma}}}^a \cdot \underline{\underline{\tau}}_1^a + \underline{\underline{\tau}}_1^a \cdot \underline{\underline{\dot{\gamma}}}^a\right\} - \eta_1 \underline{\underline{\dot{\gamma}}}^a\right] d\Omega = 0, \qquad (4.7)$$

where ϕ_i is the streamline upwinding weighting function proposed by Brooks and Hughes [10]. The discretized form of the PTT model for the SU method is

$$\int_{\Omega} \phi_i \left[H\left(tr\underline{\underline{\tau}}_1^a\right)\underline{\underline{\tau}}_1^a + \lambda \underline{\underline{\tau}}_{1(1)}^a + \frac{\lambda\xi}{2}\left\{\underline{\underline{\dot{\gamma}}}^a \cdot \underline{\underline{\tau}}_1^a + \underline{\underline{\tau}}_1^a \cdot \underline{\underline{\dot{\gamma}}}^a\right\} - \eta_1 \underline{\underline{\dot{\gamma}}}^a\right] d\Omega + \int_{\Omega} \frac{\lambda \bar{k}}{\underline{v}^a \cdot \underline{v}^a}$$

$$\left(\underline{v}^a \cdot \nabla \underline{\underline{\tau}}_1^a\right) \underline{v}^a \cdot \nabla\phi_i d\Omega = 0, \qquad (4.8)$$

where the streamline upwinding weighting function is only applied to a single term in the constitutive equation. Again, the superscript "a" refers to the element value of the approximated variable. The shape functions used for the viscoelastic extra stress are bilinear. However, each element is divided into 16 subelements where the bilinear shape functions are used for the viscoealastic extra stress.

For the simulations of flow using constitutive models of the integral type, Polyflow utilizes the method developed by Dupont et al. [11]. In this technique calculations are initialized with velocity and pressure fields obtained from a simulation using a generalized Newtonian fluid (GNF) constitutive equation with a similar viscosity dependence on deformation rate as the viscoelastic integral model. The integral constitutive equation is then solved for the viscoelastic extra stresses using

these kinematics. The resulting stress field is used in a finite element computation solving the equations of motion and continuity from the equations

$$\int_{\Omega} \pi_k \left(\nabla \cdot \underline{v}^{n+1} \right) d\Omega = 0 \tag{4.9}$$

$$\int_{\Omega} \nabla \psi_j^T \cdot \left(-p^{n+1} \underline{\underline{\delta}} + \mu_A \underline{\underline{\dot{\gamma}}}^{n+1} \right) d\Omega = \int_{\partial\Omega} \psi_j \left(\underline{\underline{\sigma}} \cdot \underline{n} \right) ds + \int_{\Omega} \psi_j \nabla \cdot \left(\underline{\underline{\tau}}_1^n - \eta_1 \underline{\underline{\dot{\gamma}}}^n \right) d\Omega. \tag{4.10}$$

The new velocity field computed from Eqs. (4.9) and (4.10) is then compared to the previous velocity field, and if convergence criteria are not met, then another iteration is performed. The additional viscosity, μ_A, is used to guarantee that the left side of Eq. (4.10) is not zero.

The mesh and boundary conditions that were used for the flow problem, shown schematically in Figs. 4.3(A) and 4.3(B), respectively, were the specification of the velocity profile at the inflow, no slip at the cylinder and wall, and a vanishing normal component of the velocity along the planes of symmetry. The finite element calculations using the PTT model required additional boundary conditions which consisted of the stresses at the inflow and velocity profile at the outflow plane. The inflow and outflow planes were placed ten cylinder diameters upstream and downstream of the cylinder so that the imposition of the boundary conditions at the inflow and outflow planes would not affect the numerical solution.

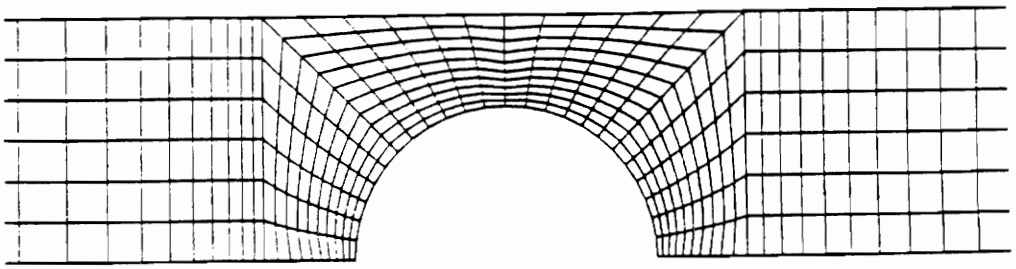

(A)

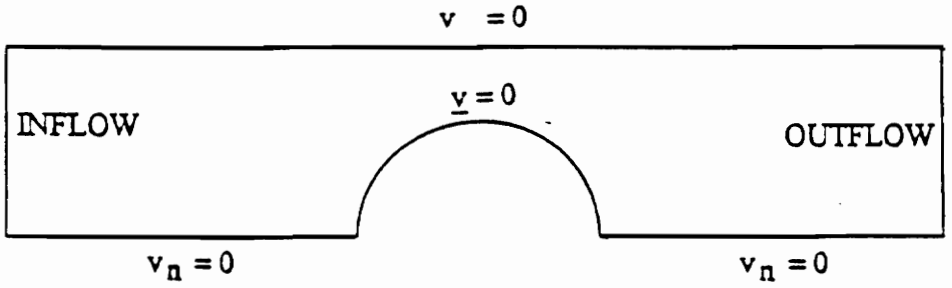

(B)

Fig. 4.3. Finite element mesh (A) with 1025 nodes; boundary conditions (B).

4.3.2 Constitutive Equations

The Phan-Thien and Tanner (PTT) constitutive equation and the Rivlin-Sawyers (RS) constitutive equation with the Papanastasiou, Scriven, and Macosko damping function have been shown to provide a good fit to the viscometric rheological properties and extensional stress growth behavior of LLDPE and LDPE [9]. In addition, these constitutive equations are able to predict some time dependent rheological properties very well. In this section the PTT model and RS model with the PSM damping function and the values of the parameters of each model are given. The procedures used to determine the values of the model parameters as well as some model predictions for basic rheological flows are given in Ref. 9.

The PTT model is given as

$$\exp\left(\frac{\lambda\varepsilon}{\eta_1}\mathrm{tr}(\underline{\underline{\tau}}_1)\right)\underline{\underline{\tau}}_1+\lambda\underline{\underline{\tau}}_{1(1)}+\frac{\lambda\xi}{2}\left(\underline{\underline{\dot{\gamma}}}\cdot\underline{\underline{\tau}}_1+\underline{\underline{\tau}}_1\cdot\underline{\underline{\dot{\gamma}}}\right)-\eta_1\underline{\underline{\dot{\gamma}}}=0, \tag{4.11}$$

where λ, ξ, η_1, and ε are adjustable parameters, and $\underline{\underline{\tau}}_{1(1)}$ is the upper convected derivative. In this form Eq. (4.11) predicts a maximum in the shear stress as a function of shear rate. Therefore the stress is expressed as

$$\underline{\underline{\tau}}=\underline{\underline{\tau}}_1+\underline{\underline{\tau}}_2 \tag{4.12}$$

where $\underline{\underline{\tau}}_1$ is the viscoelastic extra stress given by Eq. (4.11) and $\underline{\underline{\tau}}_2$ is a purely viscous contribution expressed as

$$\underline{\underline{\tau}}_2=\eta_2\underline{\underline{\dot{\gamma}}}. \tag{4.13}$$

The addition of the viscous stress to the total stress tensor prevents a maximum in shear stress versus shear rate from occurring. It has been found that to keep the stress a monotonically increasing function of shear rate, η_2 must be chosen so that $\eta_1 \leq 8\eta_2$.

The general form of the Rivlin-Sawyers constitutive equation is

$$\underline{\underline{\tau}}(t) = \int_{-\infty}^{t} M(t-t')\left[\phi_1(I_1,I_2)\,\underline{\underline{C}}^{-1} + \phi_2(I_1,I_2)\,\underline{\underline{C}}\right] dt', \tag{4.14}$$

where the relative finite strain tensors, $\underline{\underline{C}}^{-1}$ and $\underline{\underline{C}}$, are the Finger and Cauchy strain tensors, respectively [15]. M(t-t') is the viscoelastic memory function which is expressed as

$$M(t-t') = \sum_{i=1}^{N} \frac{\eta_i}{\lambda_i^2} \exp\left[-\frac{t-t'}{\lambda_i}\right], \tag{4.15}$$

where η_i and λ_i are adjustable parameters related to the relaxation spectrum. The form for ϕ_1 suggested by Papanastasiou, Scriven, and Macosko is

$$\phi_1 = \frac{\alpha}{(\alpha-3)+\beta I_1 + (1-\beta) I_2}, \tag{4.16}$$

where α and β are adjustable parameters, with β only affecting extensional flow predictions. The function ϕ_2 is taken to be zero. The scalar invariants, I_1 and I_2, are defined to be

$$I_1 = \mathrm{tr}\left(\underline{\underline{C}}^{-1}\right) \text{ and} \tag{4.17}$$

$$I_2 = \mathrm{tr}\,\underline{\underline{C}}. \tag{4.18}$$

The values of the model parameters used in this study are given in Table 4.1.

Table 4.1. Values of the parameters of the rheological models to fit simple shear and uniaxial extensional behavior of LLDPE and LDPE at 170 C.

coefficient	value	
Power Law model	**LLDPE**	**LDPE**
m	13800	5400
n	0.858	0.490
Bird-Carreau model		
η_o	12300	14300
λ	1.1	5.3
n	0.65	0.51
PTT model		
η_1	11830	15745
η_2	1479	1967
λ	0.46	4.1
ξ	0.01	0.09
ε	0.10	0.01
PSM model		
$\eta_1(\lambda_1=10^{-3})$	450	85.0
$\eta_2,(\lambda_2=10^{-2})$	2200	550
$\eta_3,(\lambda_3=10^{-1})$	4400	2100
$\eta_4(\lambda_4=10^{0})$	6100	7900
$\eta_5(\lambda_5=10^{1})$	3400	12000
$\eta_6(\lambda_6=10^{2})$	120	7600
$\eta_7(\lambda_7=10^{3})$	25.0	0.20
α	2.14	10.9
β	0.10	0.021

4.4 Results and Discussion

In this section, the birefringence patterns measured for LLDPE and LDPE flowing past a cylinder in a planar channel will be presented. The numerical predictions obtained from finite element calculations using both the PTT model and the RS model with the PSM damping function will then be compared to measured isochromatic birefringence patterns. By comparing the numerically predicted birefringence patterns to experimental birefringence patterns, a quantitative evaluation of the numerical predictions may be performed.

4.4.1 Experimental Isochromatic Birefringence Patterns

The full order isochromatic birefringence patterns (N=0,1,2,...) for LLDPE flowing past a cylinder in a planar channel for Deborah number (De)=0.42 and De=0.87 are shown in Figs. 4.4(A) and 4.4(B), respectively. In this case, De is defined to be the ratio of the longest relaxation time of the fluid to the average time a fluid element spends flowing past a cylinder :

$$De = \frac{\lambda \langle v \rangle}{2R}. \qquad (4.2)$$

The main difference in the birefringence patterns which can be qualitatively observed is the number of fringes which cross the centerline in the wake of the cylinder. For De=0.42, shown in Fig. 4.4(A), there are two fringes which cross the centerline in the wake, representing stresses which fully relax about 1.0 cylinder diameter downstream of the cylinder. For De=0.87, shown in Fig. 4.4(B), there are three fringes which cross the centerline in the wake of the cylinder. The stresses represented by these fringes

fully relax 1.2 cylinder diameters downstream of the cylinder. Thus, as the flow rate (or De) is increased, stresses imparted to fluid elements flowing past the cylinder persist for longer distances downstream of the cylinder.

The isochromatic birefringence patterns (N=0,1,2,...) for LDPE flowing past a cylinder in a planar channel for De=0.61 and De=3.2 are shown in Figs. 4.5(A) and 4.5(B), respectively. For De=0.61, shown in Fig. 4.5(A), the stresses in the wake of the cylinder relax completely 1.78 cylinder diameters downstream. For De=3.2, shown in Fig. 4.5(B), the stresses in the wake of the cylinder persist over 20 cylinder diameters downstream of the cylinder (not visible in figure). In addition, there is a cluster of isochromatic fringes around the centerline downstream of the cylinder for De=3.2.

The presence of isochromatic fringes clustered around the centerline in the wake of the cylinder for LDPE at De=3.2 is likely due to the result of two rheological properties. First, LDPE has a longer relaxation time than LLDPE. Highly stressed fluid elements flowing near the cylinder wall experience long residence times in high stress regions of the flow field. As the fluid elements flow past the cylinder into the wake, the stresses do not relax immediately due to the long relaxation time. Second, the flow along the centerline in the wake of the cylinder is a planar extensional flow as a result of fluid elements being accelerated along the centerline. The extensional viscosity behavior of LDPE may have an effect on the flow in this region. The strain hardening behavior of LDPE may result in the development of large extensional stresses in the wake of the cylinder.

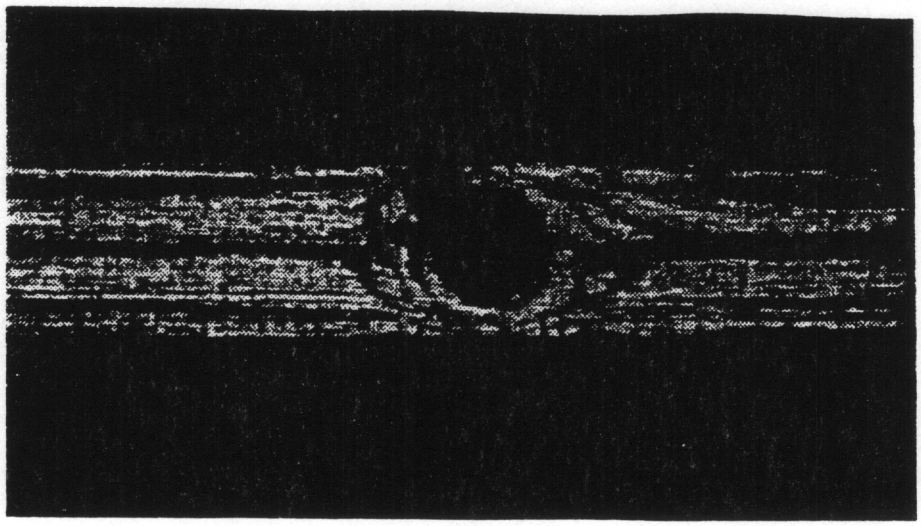

(A)

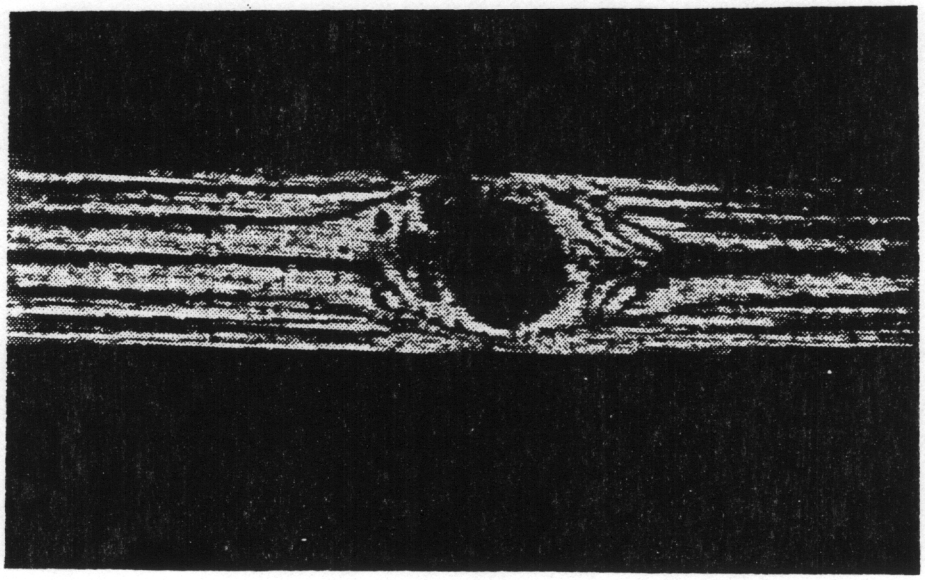

(B)

Fig. 4.4. Full order isochromatic birefringence patterns (N=0,1,2,...) for LLDPE flowing past a cylinder in a planar channel (from left to right) at 170°C: (A) De=0.42; (B) De=0.87.

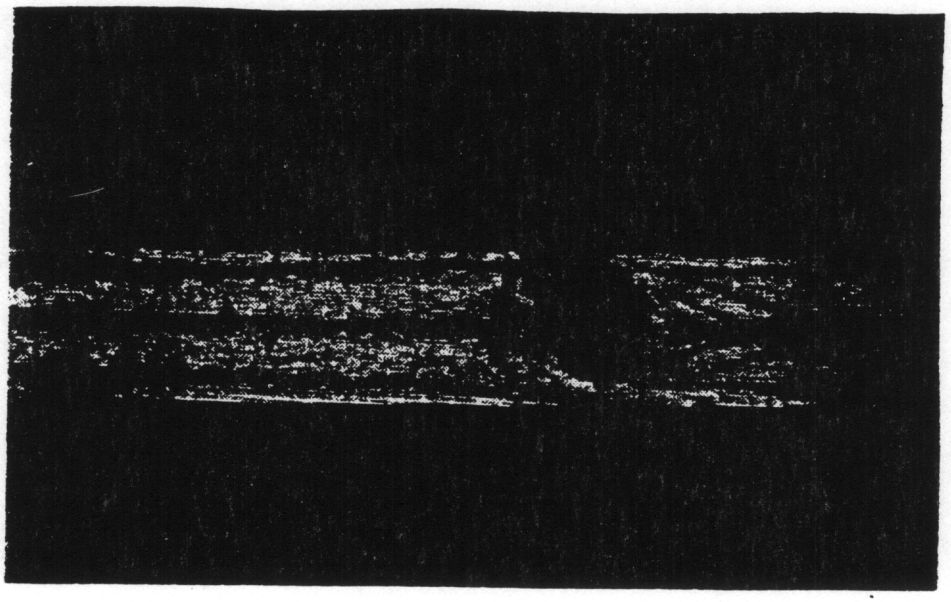

(A)

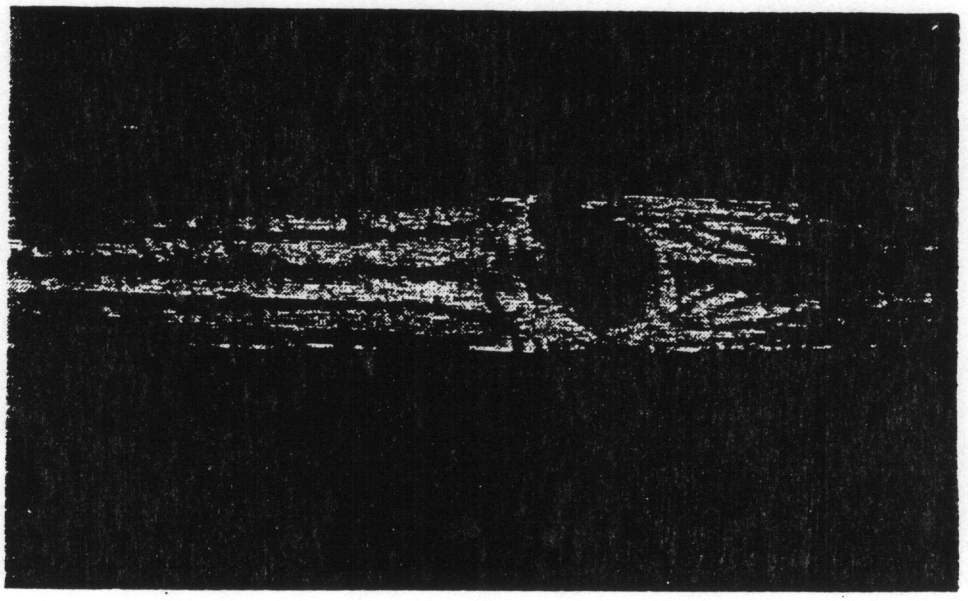

(B)

Fig. 4.5. Full order isochromatic birefringence patterns (N=0,1,2,...) for LDPE flowing past a cylinder in a planar channel (from left to right) at 170°C: (A) De=0.61; (B) De=0.3.2.

4.4.2 Comparison of Birefringence Data and Stress Predictions

In order to compare the predictions of numerical simulations to the birefringence data presented above, the full order isochromatic fringes calculated from the computed stress field were used. The numerical predictions of the fringe patterns are computed by the relation

$$N = \frac{CW}{\lambda}(\sigma_1 - \sigma_2), \tag{4.3}$$

and integer value contours of N were plotted. The stress fields were calculated by means of three methods: the 4x4SUPG method in conjunction with the PTT model; the 4x4SU method in conjunction with the PTT model; the RS model and the numerical technique developed by Dupont et al.

The experimental and numerically predicted isochromatic birefringence patterns (N=0,1,2,...) using the PTT model for LLDPE flowing past a cylinder in a planar channel for De=0.42 and De=0.87 are shown in Figs. 4.6(A) and 4.6(B), respectively. Comparison of the predictions using the PTT model obtained with the 4x4SUPG and 4x4SU methods shows that the predictions are nearly identical for this range of De. Thus the non-consistent 4x4SU method does not appear to produce inaccurate results when compared to the consistent 4x4SUPG method in this case. Comparison of the numerically predicted isochromatic fringes to experimental data shows agreement qualitatively, but only moderate agreement quantitatively. However, good agreement is obtained on the centerline in the wake of the cylinder for De=0.87.

The experimental and numerically predicted isochromatic birefringence patterns (N=0,1,2,...) using the PTT model for LDPE flowing past a cylinder in a planar channel for De=0.61 and De=3.2 are shown in Figs. 4.7(A) and 4.7(B),

respectively. For De=0.61, slight deviation between the fringes predicted by the 4x4SUPG and 4x4SU methods occurs, as shown in Fig. 4.7(A). Larger deviations between the fringes predicted by the 4x4SUPG and 4x4SU methods occur for De=3.2, shown in Fig. 4.7(B). The quantitative agreement between the numerically predicted isochromatic and experimental fringes is not good, although the main qualitative features of the fringe pattern are in agreement. Specifically, for De=3.2 the numerical predictions show a cluster of fringes around the centerline in the wake of the cylinder. However, the predicted fringes along the centerline do not persist as far downstream as the experimental fringes.

The experimental and numerically predicted isochromatic birefringence patterns for the flow of LDPE past a cylinder for De=0.62 and De=3.2 obtained using the RS constitutive equation are shown in Figs. 4.8(A) and 4.8(B), respectively. The agreement between the numerically predicted fringes and experimental fringes is good in the wake of the cylinder. The predictions of the RS model may better agree with experimental data due to the incorporation of a spectrum of relaxation times into the numerical simulations.

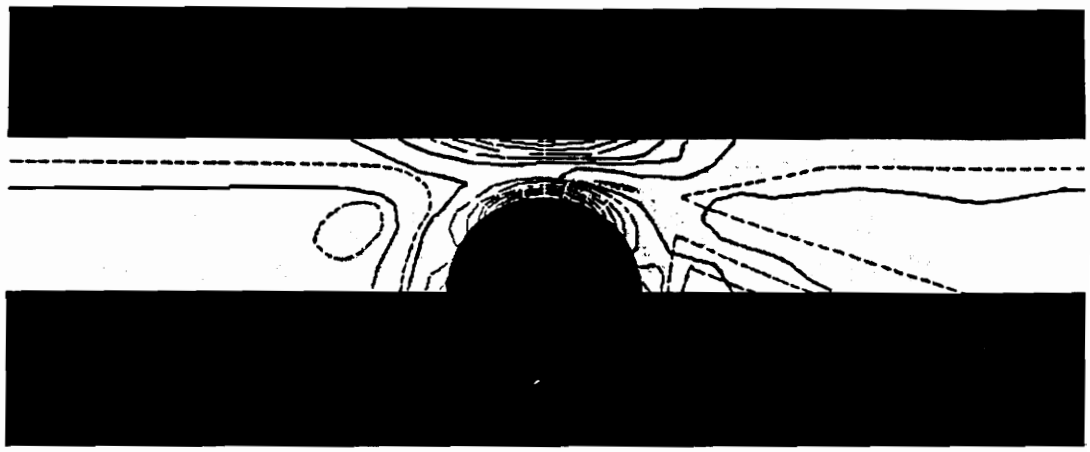

(A)

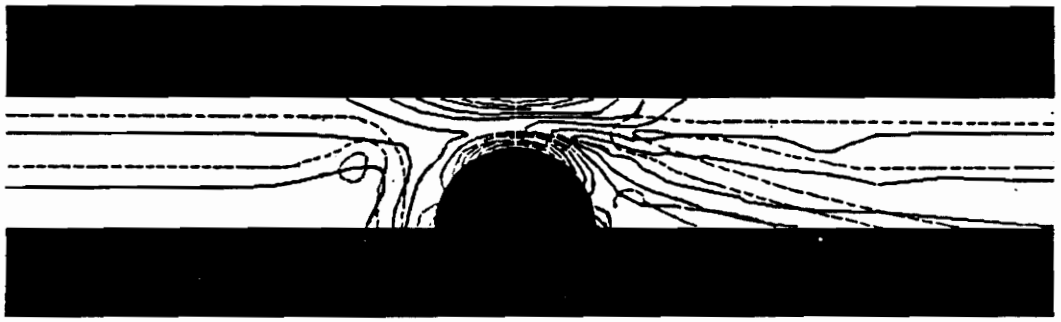

(B)

Fig. 4.8. Full order isochromatic birefringence patterns (N=0,1,2,...) for LDPE flowing past a cylinder in a planar channel at 170^{o}C; dashed lines correspond to experimental data; solid lines are results of FEM calculations using the RS model: (A) De=0.62; (B) De=3.2.

4.4.3 Flow of LDPE Past Multiple Cylinders

The isochromatic birefringence fringes (N=0,1,2,...) for LDPE flowing past the third of three cylinders in series in a planar channel for De=0.67 and De=3.2 are shown in Figs. 4.9 and 4.10, respectively. Comparison of the fringes in the wake of a single cylinder for De=0.67, shown in Fig. 4.6(A), to the fringes in the wake of a series of three cylinders, shown in Fig. 4.9, shows little difference. However, comparison of flow in the same geometries for De=3.2, shown in Figs. 4.6(B) and 4.10, respectively, indicates an effect of deformation history. The cluster of fringes present along the centerline in the wake of a single cylinder as shown in Fig. 4.6(B) are not present in the wake of the third cylinder in the series as shown in Fig. 4.10.

The deformation history effect observed to occur for the flow of LDPE past three cylinders for De=3.2 is not predicted correctly by numerical simulations performed using the 4x4SU method in conjunction with the PTT model. Numerically predicted isochromatic birefringence patterns for LDPE at De=3.2 are shown in Fig. 4.11. Comparison of the numerically predicted fringe patterns in Figs. 4.11 and Fig. 4.7(B) shows that the predicted stress field in the wake of a single cylinder is very similar to the predicted stress field in the wake of a third cylinder for De=3.2. Thus, the PTT model does not appear to predict the correct dependence of rheological properties on deformation history.

The deformation history effect discussed above was investigated in shear flow by use of double step shear rate experiments. It was found that the stress growth behavior of LLDPE is not sensitive to shear history and that the shear stress overshoot was recovered completely for very small values of t_r, while LDPE is very sensitive to shear history. The magnitudes of the shear stress

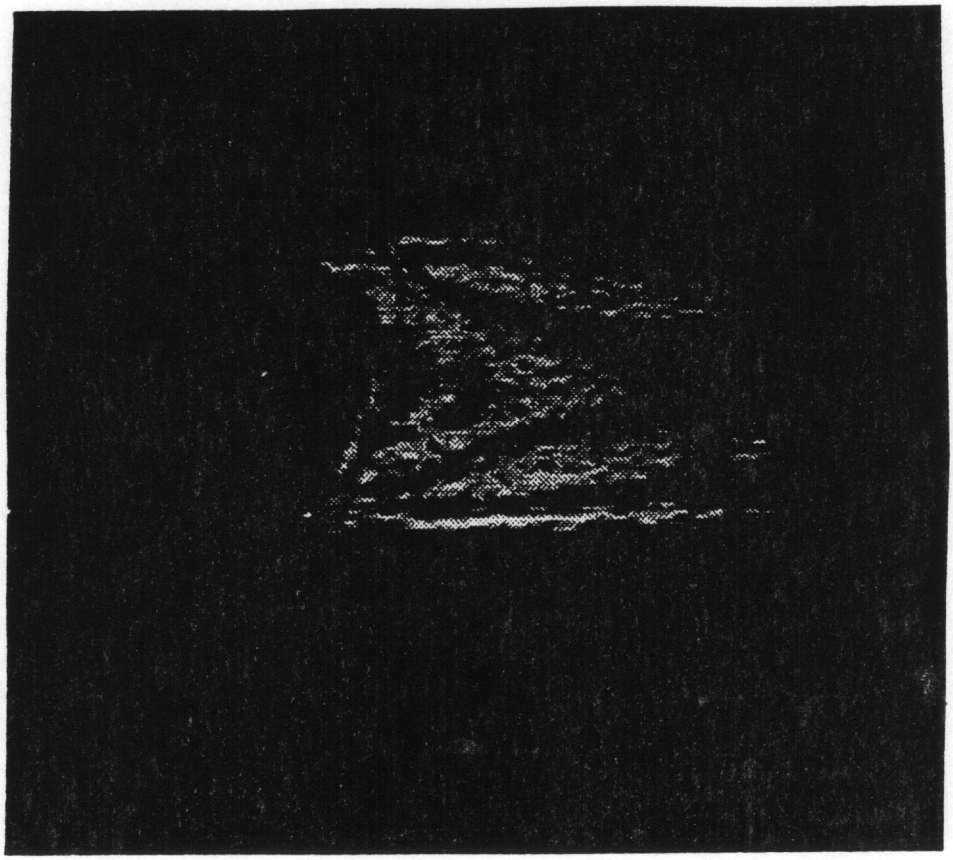

Fig. 4.9. Full order isochromatic birefringence patterns (N=0,1,2,...) for LDPE in the wake of the third of three cylinders in a planar channel (flow is from left to right); De=0.7.

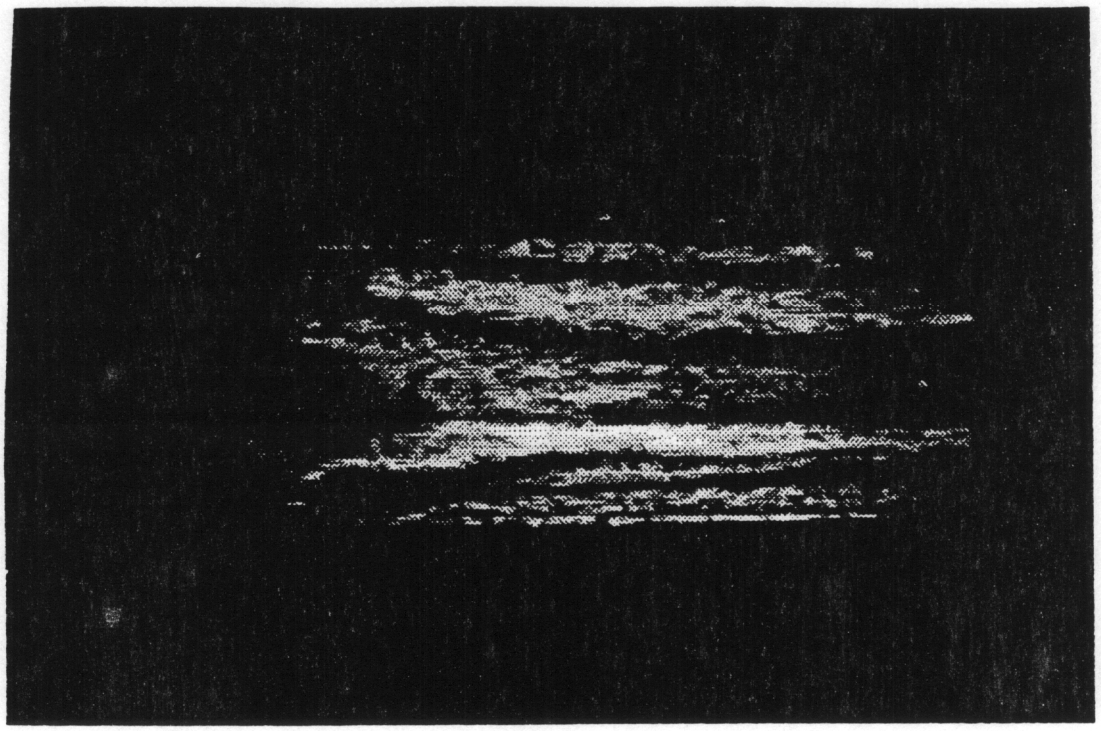

Fig. 4.10. Full order isochromatic birefringence patterns (N=0,1,2,...) for LDPE in the wake of the third of three cylinders in a planar channel (flow is from left to right); De=3.3.

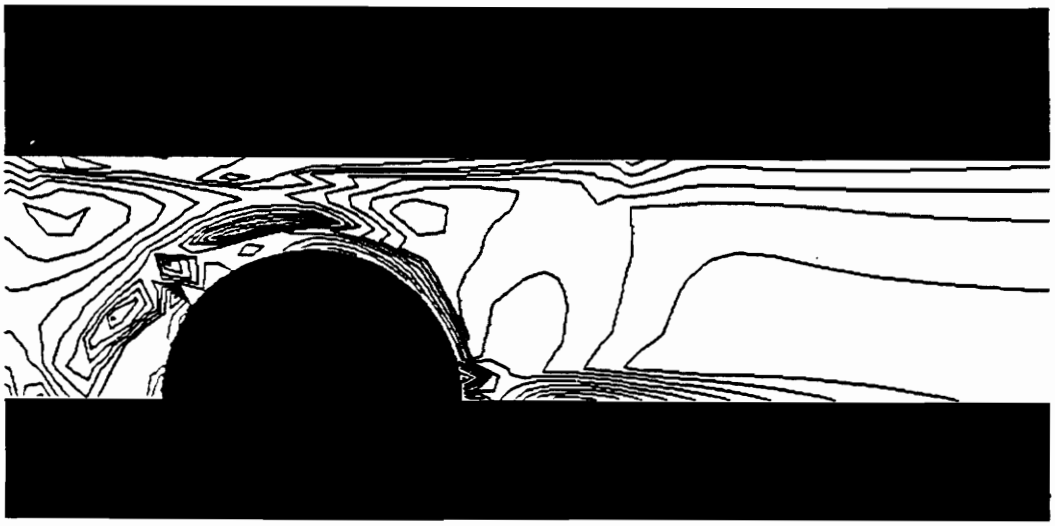

Fig. 4.11. Predicted full order isochromatic birefringence patterns for LDPE in the wake of the third of three cylinders calculated using the 4x4SU method in conjunction with the PTT model; De=3.2.

overshoots (τ_m) measured before and after the rest period (t_r) relative to the steady state value of the shear stress (τ_{ss}) was used to calculate a percent recovery (R) of the stress overshoot according to the equation

$$R = \frac{\{\tau_m(t_r) - \tau_{ss}\}}{\{\tau_m(\infty) - \tau_{ss}\}}. \qquad (4.4)$$

where $\tau_m(t_r)$ is the stress overshoot after the rest time and $\tau_m(\infty)$ is the stress overshoot of an equilibrium sample. The value of percent recovery of the shear stress overshoot was used as a quantitative measure of the depenedence of fluid structure on shear history.

The percent recovery (R) versus rest time (t_r) for LDPE at a shear rate of 1.0 s^{-1} is shown in Fig. 4.13. It can be seen that after a 100 s rest time, only 62% of the stress overshoot was recovered. The time scale associated with recovery of the stress overshoot was much longer than the average residence times of fluid elements flowing between cylinders, which varies between 0.45 and 6.2 s according to the flow rate. Therefore it is possible that for LDPE the deformation history may alter the transient rheology, in particular stress growth behavior.

The percent recovery of shear stress overshoot versus rest time predicted by the PTT and RS models for LDPE are also shown in Fig. 4.13. The predictions are not in agreement with experimental data. The PTT model predicted that the stress overshoot was nearly fully recovered after a rest time of only about 15s. The discrepancy between experimental data and the predictions of the PTT model could be related to the rates of entanglement distruction and regeneration. The PTT model is based on molecular considerations that assume entanglements (or temporary network junctions) are created and destroyed on the same time scale, which is related to the relaxation time. For polymer melts, the destruction of entanglements is of the same

order as viscoelastic relaxation time, which is generally on the order of several seconds. However, the reentanglement process for a polymer melt involves thermally driven diffusive processes, which occur on very large time scales, generally on the order of minutes [23,24,25]. The RS model does a better job than the PTT model at predicting the percent recovery of the stress overshoot as a function of t_r but still predicts that the overshoot is recovered before the data indicats. Hence, reentanglement of polymer melts may occur on a time scale much longer than viscoelastic relaxation processes.

The magnitude of the shear stress overshoot is generally no more than 10% larger than the value of the steady shear stress for LDPE at low shear rates, although at shear rates in the range of 10-20s^{-1} the stress overshoot may be much higher [15]. Therefore reduction of the shear stress overshoot behavior of LDPE may be expected to have an effect on the stress field for flow past three cylinders. However, reduction of the stress overshoot may also indicate temporary changes in other rheological properties as well. For instance, the storage modulus (G') after steady shear flow of LDPE is shown in Fig. 4.14. The steady state value of G' is regained approximately 200 s after shear flow was stopped, indicating that elastic properties of LDPE are influenced by shear history.

It has been shown here that the shear stress overshoot behavior of LDPE is sensitive to shear history. However, it is not known at present how a deformation history consisting of both shear and extensional flows affects the rheology of LDPE. Further, it is not known how deformation history affects rheological properties of LDPE other that the shear stress overshoot. Studies conducted by Rudin and coworkers [16,17,18] suggest that shear modification of LDPE decreases the elastic properties, such as $G'(\omega)$, and also decreases the die swell. Laun and Schuch have

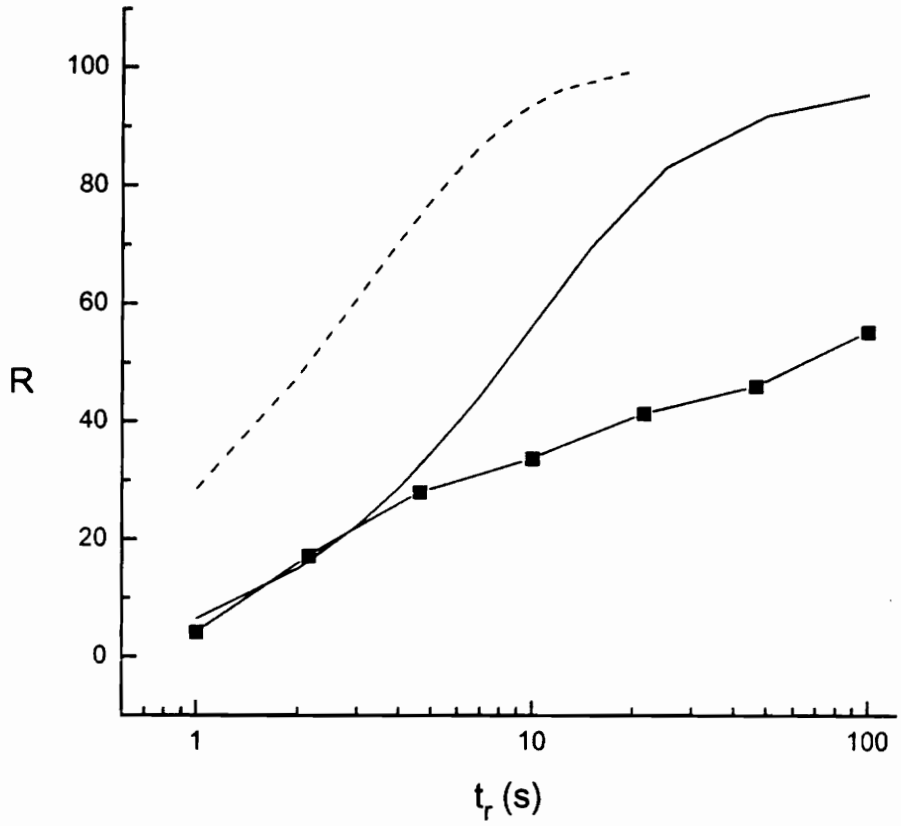

Fig. 4.13. Percent recovery of stress overshoot (R) versus rest time (t_r) for LDPE at 170°C and γ_o=1.0s^{-1}: RS model (———); PTT model (- - - -); experimental (—■—).

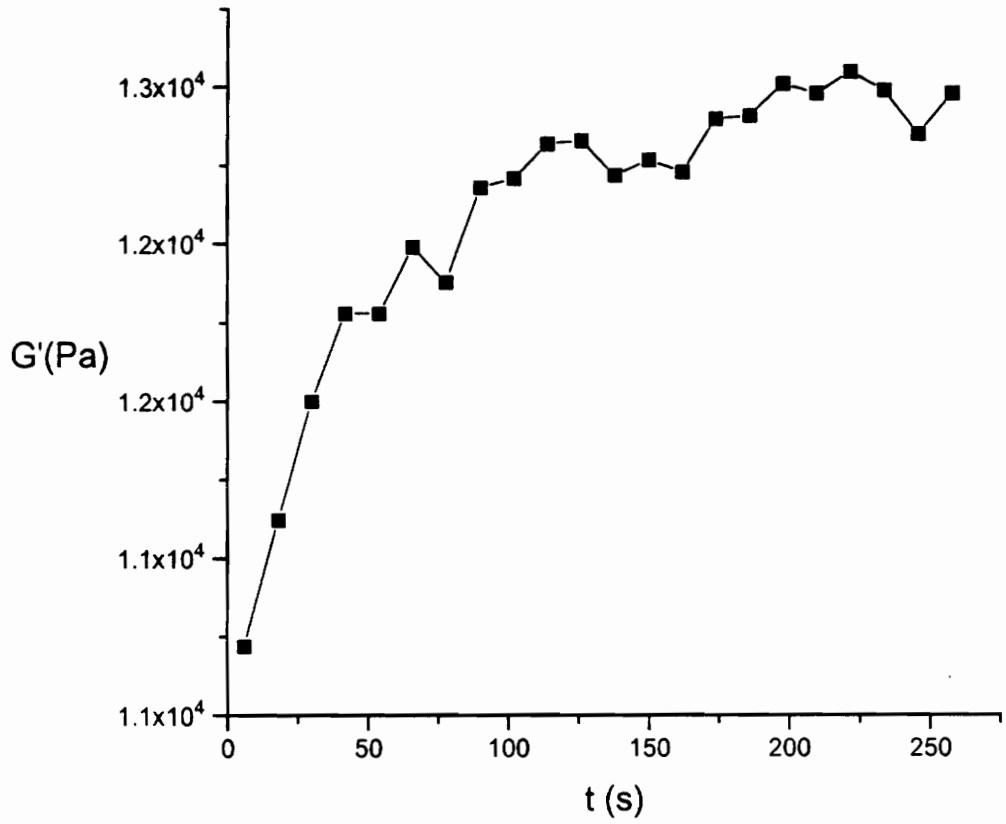

Fig. 4.14. Storage modulus versus time after cessation of steady shear flow: γ_0=1.0 s^{-1}; ω=10 rad/s.

investigated the effect of preshearing of LDPE on the extensional viscosity [20]. It was found that the extensional viscosity of LDPE was reduced by preshearing in an extruder. Hence, the deformation history imposed on LDPE flowing past cylinders may decrease the magnitude of the extensional viscosity which in turn has an effect on the stress field.

The dependence of fluid elasticity and extensional viscosity on deformation history observed to occur for LDPE may be responsible for the differences in the stress fields in the wake of a single cylinder and a third cylinder. Specifically, a decrease in fluid elasticity after preshearing, which occurs during flow past the first two cylinders, may cause stresses in the wake of the third cylinder to relax more quickly than was observed to occur in the wake of a single cylinder (see Figs. 4.6(B) and 4.10). In addition, an extensional viscosity reduced by previous defromation history may result in lower stresses in the region of planar extensional flow in the wake of the third cylinder than observed in the wake of a single cylinder (again, see Figs. 4.6(B) and 4.10).

4.5 Conclusions

It has been shown in this paper that LLDPE and LDPE polymer melts exhibit markedly different stress fields for flow past a cylinder in a planar channel. It is possible that the differences in time dependent rheology and extensional viscosity behavior of LLDPE and LDPE are responsible for the different isochromatic birefringence patterns observed along the centerline of the channel in the wake of the cylinder. The isochromatic birefringence patterns measured for LDPE flowing past a cylinder for De>1 show a cluster of fringes about the centerline in the wake of the cylinder. This behavior may result from the slow relaxation of stresses in fluid elements as they flow past the cylinder and extensional stresses developed in a region of planar extensional flow in the wake of the cylinder. The isochromatic birefringence patterns measured for LLDPE in the wake of the cylinder show that steady shear flow is resumed within about one cylinder diameter downstream of the cylinder. Hence, the differences in rheological behavior of LLDPE and LDPE result in the development of qualitatively and quantitatively different stress distributions, mainly in the wake of the cylinder.

Numerical simulations of the flow of LLDPE and LDPE past a cylinder in a planar channel using the PTT model and RS model with the PSM damping function were able to predict the differences in flow behavior observed for LLDPE and LDPE. Both of these constitutive equations described the shear stress growth behavior and extensional stress growth behavior of LLDPE and LDPE well. The quantitative agreement between $(\sigma_1 - \sigma_2)$ determined by birefringence measurements and numerical predictions was best for the RS model, although the PTT model predicted the qualitative differences. It is likely that the lack of quantitative agreement between

the prediction of the PTT model and experimental data is due to the fit of the rheological properties, which could be improved by the use of multiple relaxation times.

In addition to comparison with experimental data, calculations using the PTT model were carried out in order to assess the accuracy of the 4x4SU method. The isochromatic birefringence patterns calculated for the flow of LLDPE past a cylinder using the 4x4SUPG and 4x4SU methods were similar. This similarity is likely a result of the low De for which the calculations were performed, and the lesser degree of nonlinear rheological behavior of LLDPE relative to that of LDPE. The agreement between the predicted isochromatic birefringence patterns calculated for LDPE using the 4x4SUPG and 4x4SU methods was good, although there were some variations in the predicted patterns, especially near the cylinder wall.

Finally, the effect of deformation history on the flow of LDPE past three cylinders was investigated. It was found that the rheology of LDPE changes as the fluid flows from cylinder to cylinder in a channel. The isochromatic birefringence patterns for LDPE in the wake of a third cylinder were very different from the isochromatic birefringence patterns observed in the wake of a single cylinder. This effect of deformation history on the rheology of LDPE in a simple flow was investigated using double step shear rate tests and measurement of elastic properties after steady shear flow. These tests indicate that there is a time scale associated with reentanglement which occurs on a much longer time scale than viscoelastic relaxation processes. The PTT model was not able to predict the correct time dependence of this reentanglement process. It is suggested here that it is important from the aspect of numerical modeling that constitutive equations predict the correct rheological dependence on deformation history.

In a recent study of flow of LDPE through a periodic array of cylinders, we overpredicted the pressure drop [9]. The inability of the PTT model and the RS model with the PSM damping function to correctly predict the dependence of flow behavior on deformation history may be a cause of the inability to correctly predict the pressure drop of LDPE flowing through a periodic array of cylinders . The deformation history experienced by LDPE as it flows through a square array of cylinders is very similar to that experienced in flow past cylinders in a planar channel. In a recent study of LDPE flowing through a square array of cylinders, pressure drop predictions using the PTT model were higher than experimental measurements. The changes in flow behavior which LDPE undergoes as it flows past cylinders may serve to decrease the stress overshoot and extensional viscosity, thus decreasing the pressure drop. Therefore, the constitutive equation used to describe the rheology of LDPE must account for deformation history effects if accurate engineering calculations are to be made.

4.6 Literature Cited

1. G.H. McKinley and R.A. Brown, J. Non-Newt. Fluid Mech., 52, 407 (1994).
2. O. Hassager, J. Non-Newt. Fluid Mech., 29, 2-5 (1988) .
3. M.J. Crochet, in P.H.T. Uhlherr (Ed.) Xth International Congress on Rheology, Sydney, Vol. 1, 19-24, (1988).
4. J.S. Ultmann and M.M. Denn, Chem. Eng. J., 2, 81-89 (1971).
5. O. Manero and B. Mena, J. Non-Newt. Fluid Mech., 9, 379-387 (1981).
6. S.A. Dhahir and K. Walters, J. Rheol., 33, 781-804 (1989).
7. H. Hu and D.D. Joseph, J. Non-Newt. Fluid Mech., 37, 347-377 (1990).
8. V. Delvaux and M.J. Crochet, J. Non-Newt. Fluid Mech., 37, 297 (1990).
9. W.H.Hartt and D.G. Baird, AIChE J., to be submitted
10. J.M. Marchal and M.J. Crochet, J. Non-Newt. Fluid Mech., 22, 219 (1987).
11. S. Dupont, J.M. Marchal, M.J. Crochet, J. Non-Newt. Fluid Mech., 17, 157 (1985).
12. R.I. Tanner and H.Jin, J. Non-Newt. Fluid Mech., 41, 171 (1991).
13. R.C. King, M.R. Apelian, R.C. Armstrong, R.A. Brown, J. Non-Newt. Fluid Mech., 29, 147 (1988).
14. H. Janeschitz-Kriegl, *Polymer Melt Rheology and Flow Birefringence*, Springer-Verlag, New York (1983).
15. R.B. Bird, R.C. Armstrong, O. Hassager, *Dynamics of Polymeric Liquids, Vol. 1.*, Wiley-Interscience, New York (1987)
16. J.W. Teh, A. Rudin, and H.P. Schreiber, Plast. and Rubb. Proc. Appl., Vol. 4, 157 (1984).
17. R. Schertzer, A. Rudin, and H.P. Schreiber, J. Appl. Polym. Sci., 31, 809 (1986).
18. M.V. Prooyen, T. Bremner, and A. Rudin, Polym. Eng. Sci., 34, 570 (1994).
19. F.P.T. Baaijens, H.P.W. Baaijens, G.W.M. Peters, and H.E.H. Meijer, J. Rheol., 351 (1994).
20. H.M. Laun and H. Schuch, J. Rheol., 33(1), 119 (1989).
21. H. Munstedt, J. Rheol., 23, 421 (1979).
22. G.H. McKinley, R.C. Armstrong, and R.A. Brown, Proc. XI Int. Congr. on Rheology, Brussels, Vol. 1, 198-200 (1992).
23. M. Tirrell, Rub. Chem. Techn., 57, 523-56 (1984).
24. H.H. Kausch and M. Tirrell, Ann. Rev. Mater. Sci., 19, 341-77 (1987).
25. Pissipatti, Ph.D. Thesis, Virginia Polytechnic Institutute and State University, Blacksburg, VA.

5.0 Recommendations for Future Work

Although many questions have been answered in regards to flow of polymer melts through periodic arrays of cylinders there are many which remain to be addressed. Given below are recommendations for further work in this area.

1. Examine polymer melts other than LLDPE and LDPE. Specifically, it would desireable to perform studies with polymers with long relaxation times (similar to LDPE) that are not extensional strain rate hardening.

2. Examine polymer melts with long relaxation times and moderate strain rate hardening. It would be desireable to see how precise numerical calculations are in regards to predicting pressure drops of polymers with only slightly different extensional viscosity behavior.

3. Perfom numerical simulations with a multimode PTT model. This would allow an accurate fit of the constitutive equation to visometric properties. This would also eliminate the uncertainty associated with the fit of the constitutive equation.

4. Build a slit die in a manner such that flow in a periodic array of cylinders could be visualized and the birefringence recorded.

5. Build a flow system with the current permeability cell such that higher flow rates could be attained. Do flow instabilities develop before the onset of melt fracture?

6. Numerical methods are still a problem with the simulation of viscoelastic flow. Convergence for high De is a problem for highly nonlinear differential constitutive equations. The EVSS method may be a candidate for future work.

7. Accurate simulation of 2D flow using integral constitutive equations is highly desireable. The method used in this work does not appear to give accurate results. Development of novel methods to simulate flows using integral models should be considered.

Appendix A. Flow Birefringence

Most polymer molecules are electrically anisotropic and are therefore also optically anisotropic. This optical anisotropy may be utilized as a characteristic of the average overall orientation of the polymer chains in a system. When a polymer melt is is not subjected to stress and is under quiescent conditions, the random orientation of the polymer chains results in isotropic optical behavior. The average orientation of a polymer system changes when the system is subjected to stress. The orientation of the polymer chains induced by stress causes an optical anisotropy which may be measured experimentally and is called birefringence. The relation between stress in a polymer system and birefringence has been derived theoretically [77]. In practice however, the following relation is relied upon:

$$\underline{\underline{n}} - n_m \underline{\underline{I}} = C\left(\underline{\underline{\tau}} + p\underline{\underline{I}}\right), \qquad \text{(A1)}$$

where n is the refractive index, n_m is the mean refractive index, τ is the extra stress, and C is the stress-optical coefficient which may be measured experimentally. Once the stress-optical coefficient, C, is known, the stress may be calculated from the birefringence.

The assumptions which accompany use of the stress-optical law give above are as follows: First, the real polymer chain is well described by a statistical chain. This assumption is necessary since the stress-optical coefficient is theoretically found to be a constant using the assumption of a statistical chain. Second, only small deformations of the polymer chains are assumed to occur. If large deformations occur, the stress-optical law would become nonlinear. While the stress-optical law is believed to apply in three dimensions, in practice two dimensional flows are examined. The first principle stress difference, $\Pi = \Pi_I - \Pi_{II}$, is related to the extra stresses by the equations

$$\Pi \sin 2\chi' = 2\tau_{12}$$

$$\Pi \cos 2\chi' = \tau_{11} - \tau_{22} \qquad \text{(A2)}$$

The birefringence is related to the refractive index components by the same relations

$$\Delta n \sin 2\chi = 2n_{12}$$
$$\Delta n \cos 2\chi = n_{11} - n_{22} \qquad \text{(A3)}$$

where χ is the extinction angle. The following relations result from eqn. A1

$$n_{12} = C\tau_{12}$$
$$n_{11} - n_{22} = C(\tau_{11} - \tau_{22}) \qquad \text{(A4)}$$

Incorporation of eqn. A4 into eqns. A2 and A3 results in a useful relation between stress and birefringence:

$$\Delta n \sin 2\chi = 2C\tau_{12}$$
$$\Delta n \cos 2\chi = C(\tau_{11} - \tau_{22}) \qquad \text{(A5)}$$

Eqns. A5 may be combined to an equation which is useful for relating computed stress to birefringence

$$\Delta n = C\sqrt{4\tau_{12}^2 + (\tau_{11} - \tau_{22})^2} \qquad \text{(A6)}$$

The experimental parameters which must be known are the wavelength of light, λ, and the length of the optical path, L. In full field methods, the fringe order is related to the birefringence by the eqn.

$$N = \frac{\Delta nL}{\lambda} \qquad \text{(A7)}$$

where N is the fringe order, or optical retardation.

Appendix B

Model Parameter Estimation for The Rivlin-Sawyers Single Integral Model with the Papanastasiou, Scriven, and Macosko Damping Function

The use of single integral model constitutive equations in numerical simulation of non-Newtonian flows has been increasing during the past decade. Several groups around the world have generally approached the problem by three different methods 1.) streamline integration methods [1,2]; 2.) Lagrangian methods [3]; and 3.) methods developed by Bernstein et. al. and Dupont and Crochet et. al. [4,5]. A thorough review of these methods was given by Keunings in ref. [6]. Numerical simulation schemes utilizing streamline integration and Lagrangian techniques suffer from mesh distortion for large strains and cannot handle recirculation. The methods developed by Bernstein et. al. and Dupont et. al. are computationally demanding, but may lend themselves very well to parallel distributed computation schemes [7].

POLYFLOW implements the technique developed by Dupont and Crochet to solve integral model flow problems using the finite element method. Several integral models are available in POLYFLOW. The model which has been chosen for this work is the integral model of Papanastasiou, Scriven, and Macosko [8]. The remainder of this appendix will be devoted to estimation of the model parameters of the PSM model for NPE-953 (LDPE) and NTA-101 (LLDPE) at 170^{o}C.

The Integral Model of Papanastasiou, Scriven, and Macosko

The general form of a factorized Rivlin-Sawyers constitutive equation is

$$\tau(t) = \int_{-\infty}^{t} M(t-t')\left[\varphi_1(I_1, I_2)\gamma_{[0]} + \varphi_2(I_1, I_2)\gamma^{[0]}\right]dt', \qquad \text{(A1)}$$

where M(t-t') is the linear viscoelastic memory function, φ_i are nonlinear damping functions which depend on the first and second strain invariants, I_1 and I_2, and $\gamma^{[0]}$ and $\gamma_{[0]}$, the relative finite strain tensors [9]. Papanastasiou, Scriven, and Macosko defined the nonlinear damping functions to be:

$$\varphi_1 = \frac{\alpha}{(\alpha-3)+\beta I_1 + (1-\beta)I_2} \qquad \text{(A2)}$$
$$\varphi_2 = 0$$

where α and β are adjustable parameters, β affecting only extensional and mixed flows where $I_1 \neq I_2$. Thus the predicted homogeneous shear and homogeneous extensional rheological behavior are essentially independent of each other. The damping function was derived empirically. For a homogeneous shear flow, the damping function simplifies to

$$\varphi_1 = \frac{\alpha}{\alpha+\gamma^2}, \qquad \text{(B3)}$$

which is a sigmoidal shaped function which matches experimental data for many viscoelastic fluids quite well. For extensional flows, the parameter β adjusts the degree of strain hardening which the model predicts. In the next section the linear viscoelastic spectrum and the parameters α and β will be estimated from dynamic oscillatory data, step strain tests, and uniaxial extensional growth tests respectively.

Estimation of Model Parameters from Rheological Data

The rheological data used to estimate the model parameters consisted of dynamic mechanical data to obtain G'(ω) and G"(ω), step strain data to obtain the nonlinear damping function $h(I_1,I_2)$ which is a function of α and the imposed strain, and uniaxial extensional stress growth data to estimate the parameter β. The rheological shear data were obtained with an RMS 800 dynamic mechanical rheometer and the uniaxial extensional stress growth data was obtained with a Rheometrics RER.

The linear viscoelastic memory function, M(t-t') was determined by fitting a spectrum of moduli and relaxation times of the form

$$G'(\omega_j) = \sum_{k=1}^{N} \frac{\eta_k \lambda_k \omega_j^2}{1+(\lambda_k \omega_j)^2} \qquad \text{(B4)}$$

and

$$G''(\omega_j) = \sum_{k=1}^{N} \frac{\eta_k \omega_j}{1+(\lambda_k \omega_j)^2}. \qquad \text{(B5)}$$

Once η_k and λ_k are determined, the following linear viscoelastic memory function is used in the integral model:

$$M(t-t') = \sum_{k=1}^{N} \frac{\eta_k}{\lambda_k^2} \exp\left(-\frac{t-t'}{\lambda_k}\right). \qquad \text{(B6)}$$

Since the value of N must be finite for computational schemes and realistically about 7 or 8 , it is important to use relaxation times which are in the region of interest. Relaxation spectrums with N=7 were used in this work encompassing $\lambda=10^{-3}$ to 10^3 seconds. The relaxation spectrum for NPE-953 is given in Table I and the corresponding fit of G'(ω) and G"(ω) is shown in fig. 1. Table II and Fig. 2 contain the

relaxation spectrum of NTA-101 and the corresponding fit of the spectrum to G'(ω) and G"(ω).

The nonlinear damping function for homogeneous shear flows, eq. 3, may be obtained from step strain tests in order to determine the parameter α. The nonlinear damping function may be defined as:

$$h(I_1, I_2) = \frac{G(\gamma, t \to 0)}{G(\gamma \to 0, t \to 0)}. \qquad \text{(B7)}$$

Thus step strain data may be used to obtain the damping function, h, as a function of imposed strain, γ. In figs. 3 and 4 are shown step strain tests for NPE-953 and NTA-101, respectively. The parameter α was obtained by a nonlinear least squares fit. In this work the IMSL routine RNLIN was used for nonlinear least squares fits of rheological data to eq. 3. A listing of the driver program is given in Table III. The damping function and corresponding nonlinear least squares fit for NPE-953 and NTA-101 are shown in fig. 5 and fig. 6, respectively, along with the values of α.

Once the linear viscoelastic relaxation spectrum and the nonlinear damping function parameter, α, are determined, the homogeneous shear flow rheology is completely determined. To calculate the predicted steady shear flow predictions of the PSM model, the following strain history is applied:

$$\gamma(t - t') = \begin{cases} -\dot{\gamma}_0 t; t > 0, t' < 0 \\ -\dot{\gamma}_0 (t - t'); t > 0, t' > 0 \end{cases} \qquad \text{(B8)}$$

where a particle has a position **r'** at some past time t' and a position **r** at the present time t. The constant shear rate applied at t=0 is $\dot{\gamma}_0$. The finite strain tensor $\gamma_{[0]}$ must also be known in order to calculate the model predictions and is defined to be:

$$\gamma_{[0]} = \delta - B(t, t'), \qquad \text{(B9)}$$

where δ is the unit tensor and $B(t,t')$ is the Finger strain tensor defined to be:

$$B(t,t') = \sum_m \frac{\partial x_i}{\partial x'_m} \frac{\partial x_j}{\partial x'_m}. \tag{B10}$$

Thus for a homogeneous shear flow, the finite strain tensor, $\gamma_{[0]}$, is:

$$\gamma_{[0]} = \begin{bmatrix} -\gamma_{yx}^2 & \gamma_{yx} & 0 \\ \gamma_{yx} & 0 & 0 \\ 0 & 0 & 0 \end{bmatrix}. \tag{B11}$$

Eq. 1 may then be solved numerically for the steady or transient viscosity and normal stress differences predicted in a simple shear flow. In fig.7, the viscosity and first normal stress difference, N_1, are shown along with the curve representing the predictions of the PSM model with the parameters estimated thus far. In fig. 8, the corresponding data and model fit for NTA-101 are shown. The PSM model predicts the shear rate dependence of the viscosity and the shear rate dependence of N_1 very well. The second normal stress difference, N_2, is always equal to zero when either φ_1 or φ_2 is zero. Thus the predicted value of N_2 is zero. There may be significant effects in numerical simulations as a consequence of N_2=0. Finite values of N_2 may stabilize viscoelastic flows [10].

The parameter β may be estimated by fitting the model to uniaxial stress growth data and adjusting the parameter manually. To solve the model for the extensional stress, the kinematics associated with uniaxial extension are used to calculate the finite strain tensor, $\gamma_{[0]}$, which is

$$\gamma_{[0]} = \begin{bmatrix} 1-\lambda_x^2 & 0 & 0 \\ 0 & 1-\lambda_y^2 & 0 \\ 0 & 0 & 1-\lambda_z^2 \end{bmatrix}, \tag{B12}$$

where λ_i are the principal elongation ratios. The principal elongation ratios for uniaxial extension are

$$\begin{aligned}\lambda_x &= \exp\left(\frac{1}{2}\varepsilon(t,t')\right)\\ \lambda_y &= \exp\left(\frac{1}{2}\varepsilon(t,t')\right)\\ \lambda_z &= \exp\left(-\varepsilon(t,t')\right)\end{aligned} \qquad \text{(B13)}$$

where $\varepsilon(t,t')$ is the Hencky strain. The strain history for uniaxial extension is described by the following eq.:

$$\varepsilon(t,t') = \begin{cases} -\dot{\varepsilon}t; t>0, t'<0 \\ -\dot{\varepsilon}(t-t'); t>0, t'>0 \end{cases} \qquad \text{(B14)}$$

The predictions of the PSM model for uniaxial extensional flows are shown along with the corresponding rheological data in fig. 9 for NPE-953 along with the value of β. The strain hardening exhibited by LDPE is predicted very well by the model. Close examination of fig. 9 reveals that even the strain rate at which strain hardening begins to occur is predicted very well. However, the plateau value of the extensional stress, if one exists, is difficult to measure experimentally so the value of β is somewhat arbitrary. Different values of β have virtually no effect on the fit of the model in the region where rheological data is available as shown in fig. 10. In fig. 11, the fit of the PSM model to the uniaxial stress growth of NTA-101 is shown. NTA-101 does not exhibit strain hardening in the range of strain rates shown. Table IV shows the parameters obtained for NPE-953 and NTA-101. The PSM model predictions match the rheological data very well. The rheological data shown in figs. 9 and 11 indicate

that the PSM model may predict a wide range of extensional behavior a minimum of effort in fitting the parameters.

Summary

The parameters of the PSM model have been estimated utilizing various rheological tests to fit the linear viscoelastic spectrum, and parameters α and β. The rheological predictions of the model are excellent in simple shear flow and uniaxial extensional flows. The model provides excellent predictions in homogeneous flows. More work is necessary to determine the performance of the model in nonhomogeneous flows.

References

1. Papanastasiou, A.C., Scriven, L.E., and Macosko, C.W., "A Finite Element Method for Liquids with Memory," J. Non-Newt. Fluid Mech. **22**, 271-288 (1987).

2. Luo, X.L., and Tanner,R.I., "A Streamline Element Scheme for Solving Viscoelastic Flow Problems, Part II: Integral Constitutive Models," J. Non-Newt. Fluid Mech. **22**, 61-89(1986).

3. Hassager, O., and Bisgaard, C., "A Lagrangian Finite Element for the Simulation of Flow of Non-Newtonian Liquids," J. Non-Newt. Fluid Mech. **12**, 153-164 (1983).

4. Bernstein, B., Malkus, D.S., Olsen, T.E., "A Finite Element for Incompressible Plane Flows of Fluids with Memory," Int. J. Num. Meth. Fluids **5**, 43-70 (1985).

5. Dupont, S., Marchal, J.M., Crochet, M.J., "Finite Element Simulation of Viscoelastic Fluids of the Integral Type," J. Non-Newt. Fluid Mech. **29**, 81-91 (1988).

6. Keunings, R., "Simulation of Viscoelastic Fluid Flow," in *Computer Modeling for Polymer Processing*, by Tucker, T.C.

7. Keunings, R., Zone, O., and Aggarwal, R., "Parallel Algorithms in Computational Rheology," in *Theoretical and Applied Rheology*, edited by P. Moldenaers and R. Keunings, Proc. XIth Int. Congr. on Rheology, Brussels, Belgium.

8. Papanastaiou, A.C., Scriven, L.E., Macosko, C.W., "An Integral Constitutive Equation for Mixed Flows: Viscoelastic Characterization," J. Rheol. **27**, 387-410 (1983).

9. Bird, R.B., Armstrong, R.C., and Hassager, O., "Dynamics of Polymeric Liquids, Vol.1: Fluid Mechanics."

10. Larson, R.G., "Instabilities in Viscoelastic Flows," Rheol. Acta **31** 213-263 (1992).

Table B1. Relaxation Spectrum for NPE-953 at 170°C

k	λ (sec)	η (Pas)
1	10^{-3}	85.0
2	10^{-2}	550
3	10^{-1}	2100
4	10^{0}	7900
5	10^{1}	12000
6	10^{2}	7600
7	10^{3}	0.20

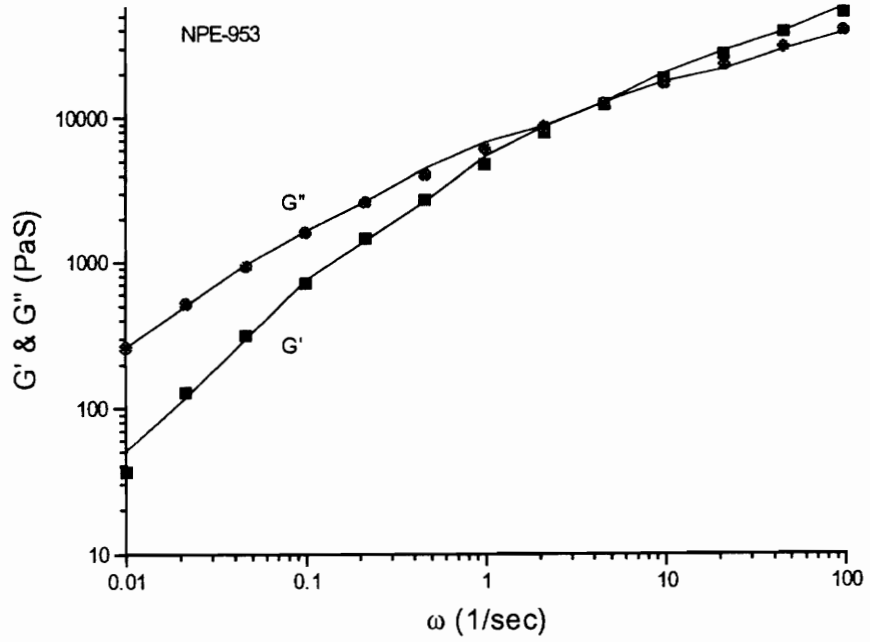

Fig. B1. Storage and Loss Modulus of NPE-953 at 170°C (symbols) and relaxation spectrum (lines).

Table B2. Relaxation Spectrum for NTA-101 at 170°C.

k	λ(sec)	η(Pas)
1	10^{-3}	450
2	10^{-2}	2200
3	10^{-1}	4400
4	10^{0}	6100
5	10^{1}	3400
6	10^{2}	120
7	10^{3}	25.0

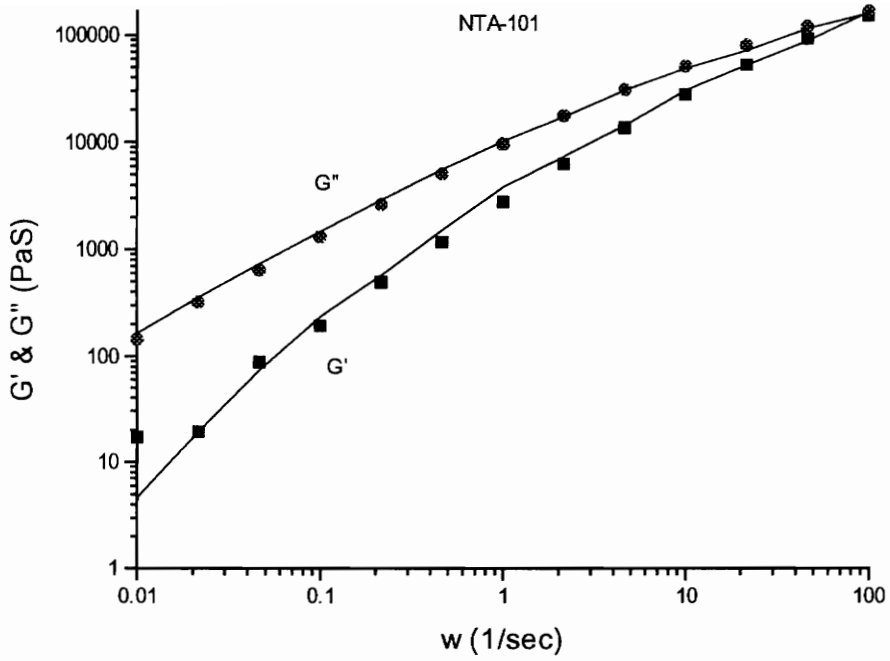

Fig. B2. Storage and Loss Modulus of NTA-101 at 170°C (symbols) with relaxation spectrum (lines).

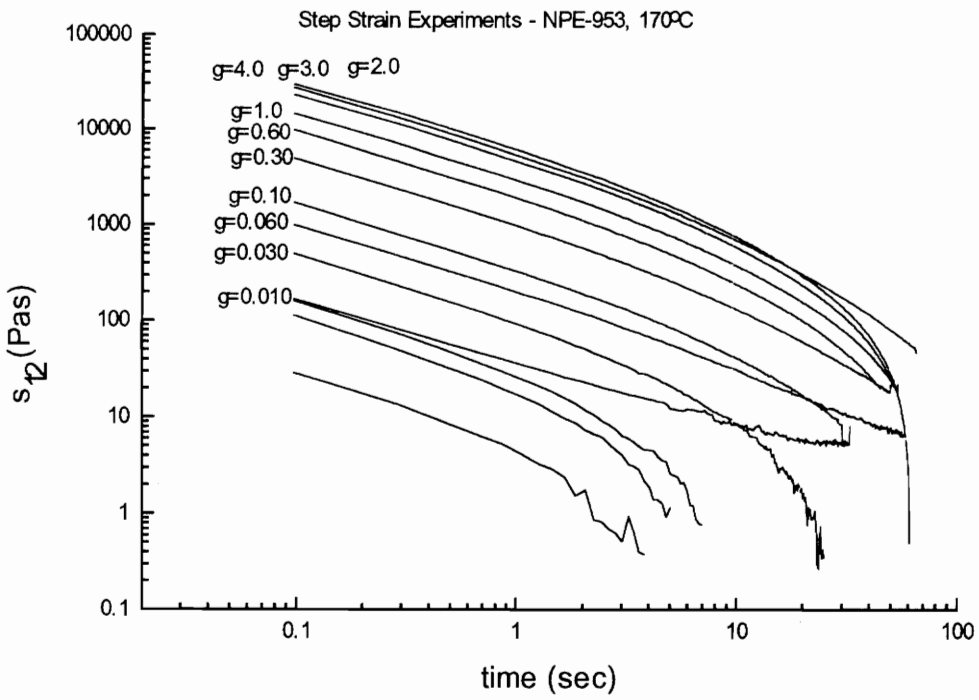

Fig. B3. Step strain tests for NPE-953 at 170°C.

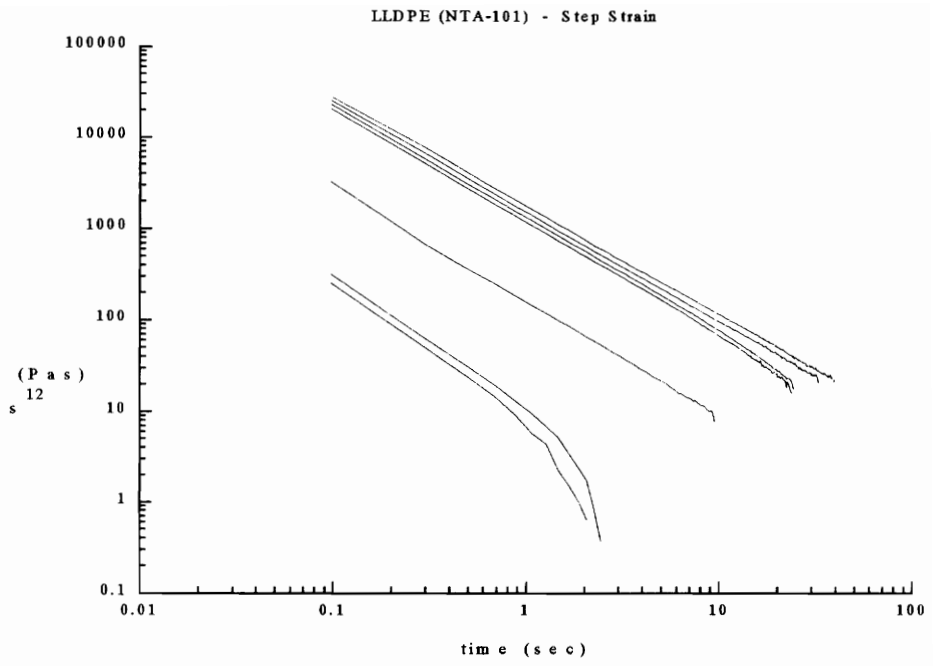

Fig. B4. Step strain tests for NTA-101 at 170^{o}C.

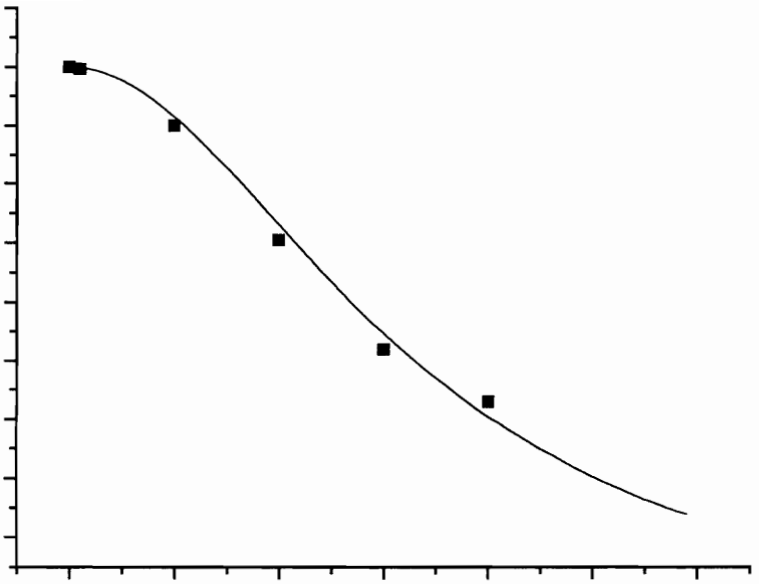

Fig. B5. Nonlinear damping function, h, and corresponding fit of the PSM damping function for NPE-953 at 170^{o}C.

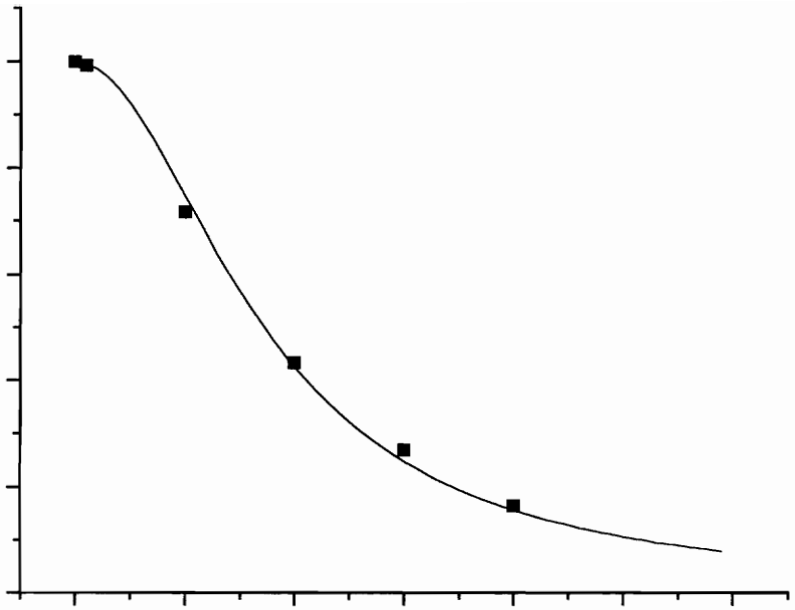

Fig. B6. Nonlinear damping function, h, and corresponding fit of the PSM damping function for NTA-101 at 170^{o}C.

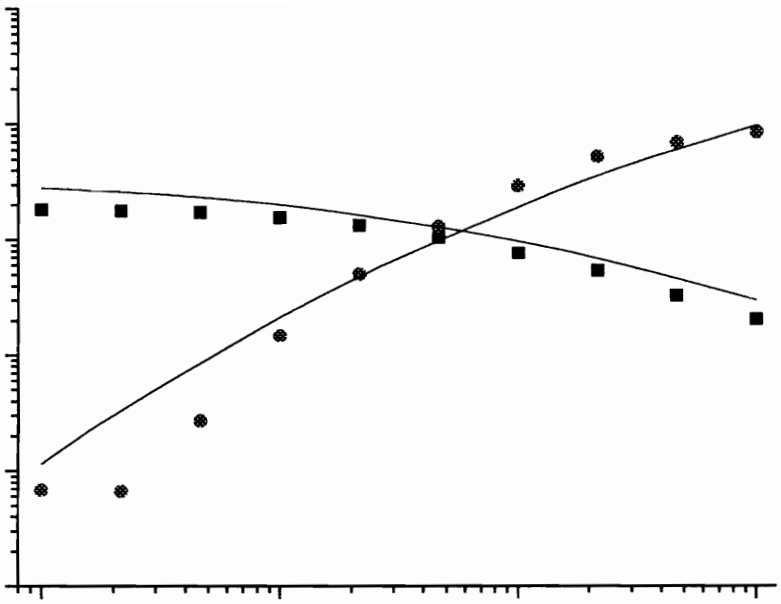

Fig. B7. Viscosity and first normal stress difference of NPE-953 (symbolds) and predictions of PSM model (lines).

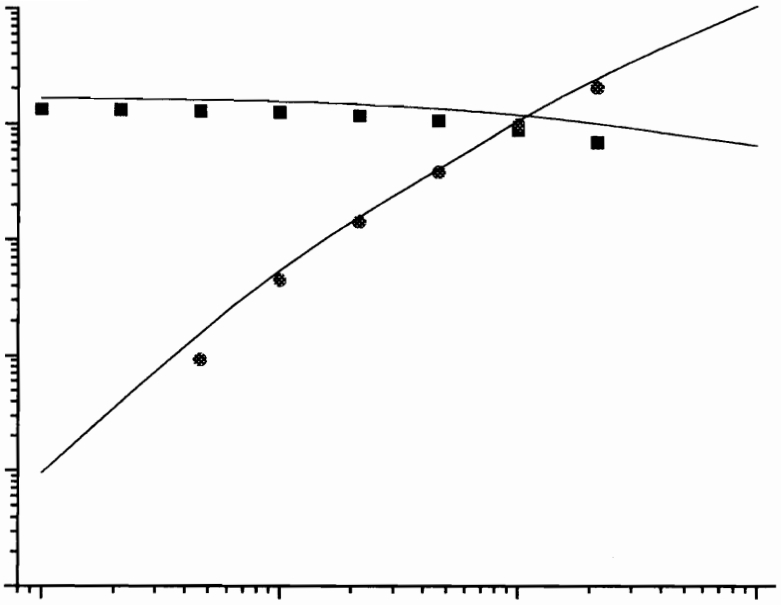

Fig. B8. Viscosity and first normal stress difference of NTA-101 (symbols) and predictions of PSM model (lines).

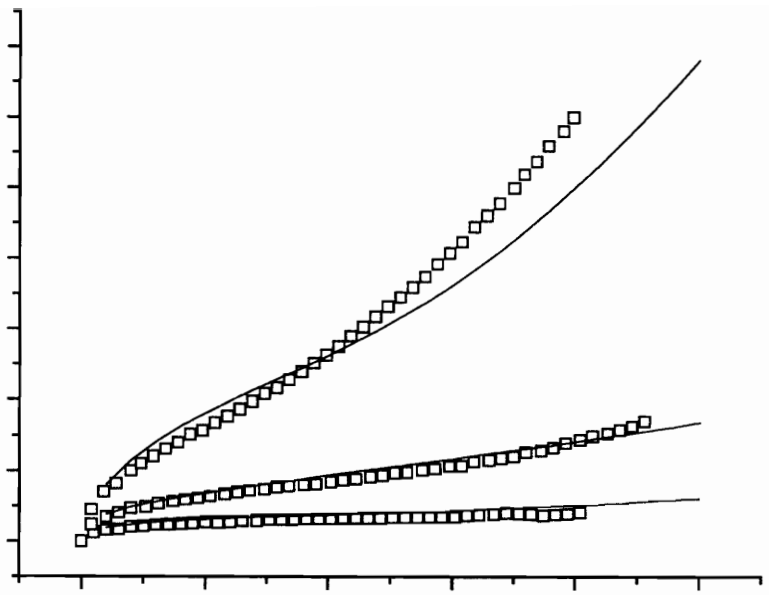

Fig. B9. Uniaxial extensional stress growth data for NPE-953 (symbols) and predictions of PSM model (lines).

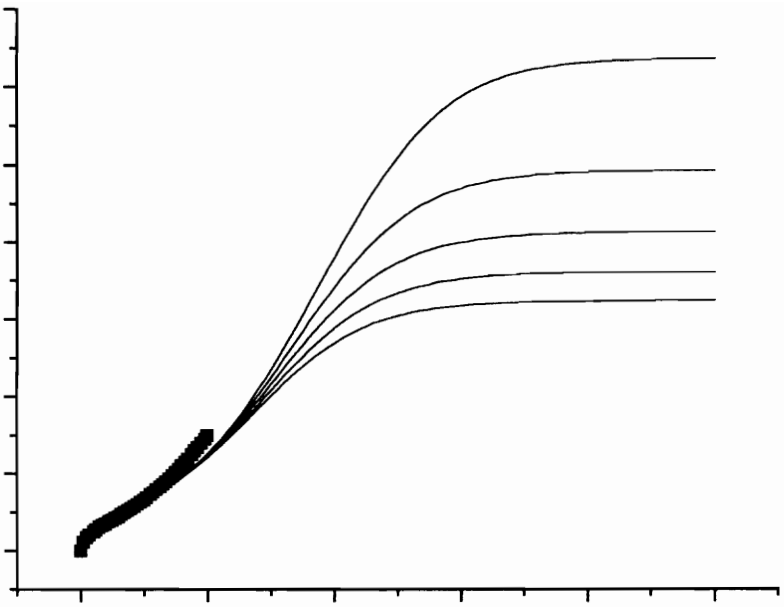

Fig. B10. Extensional stress growth data and PSM model predictions for various values of β.

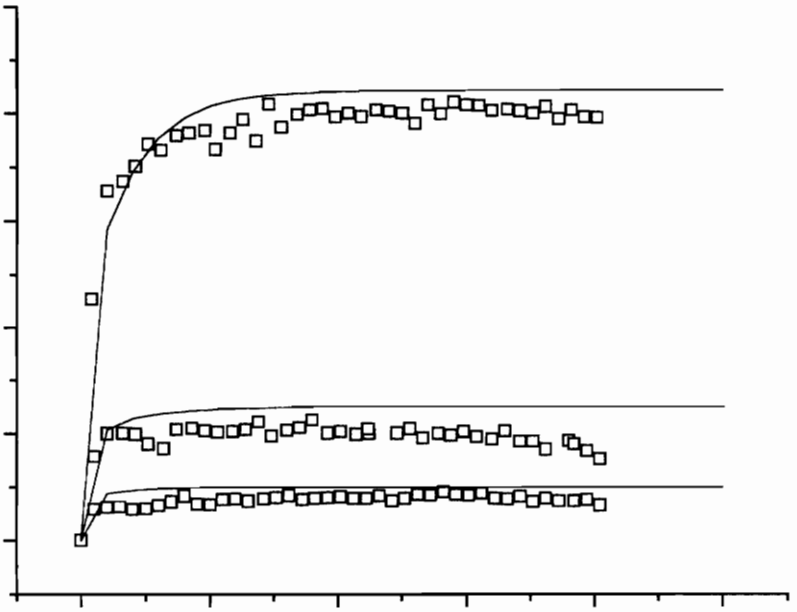

Fig. B11. Uniaxial stress growth data for NTA-101 at 170°C (symbols) and PSM model fir (lines).

Table B.3. Driver Program for IMSL Routine RNLIN to Determine Parameter α.

```
      INTEGER LDR,NOBS,NPARM
      PARAMETER (NOBS=6,NPARM=1,LDR=NPARM)
      INTEGER IDERV,IRANK,NOUT
      REAL DFE,R(LDR,NPARM),SSE,THETA(NPARM)

      EXTERNAL RNLIN,EQ

      DATA THETA/8.0/
      IDERIV=0

      CALL RNLIN(EQ,THETA,IOPT,IOBS,FRQ,WT,E,DE,IEND)

      WRITE(*,10)THETA(1)
      WRITE(*,20)IRANK,DFE,SSE
10    FORMAT(//,'THETA=',F10.3,//)
20    FORMAT(' IRANK=',I3,'DFE=',F10.3,'SSE=',F10.3)

      STOP
      END

      SUBROUTINE EQ(NPARM,THETA,IOPT,IOBS,FRQ,WT,E,DE,IEND)

      INTEGER NPARM,IOPT,IOBS,IEND
      REAL THETA(NPARM),FRQ,WT,E,DE(NPARM)
      INTEGER NOBS
      PARAMETER (NOBS=6)
      REAL XDATA(NOBS),YDATA(NOBS)

      DATA YDATA/1.0,0.993,0.717,0.434,0.270,0.165/
      DATA XDATA/0.0,0.1,1.0,2.0,3.0,4.0/

      IF (IOBS.LE.NOBS) THEN
            WT=1.0E+0
            FRQ=1.0E+0
            IEND=0
            E=YDATA(IOBS)-THETA(1)/(THETA(1)+XDATA(IOBS)**2)
```

```
ELSE
        IEND=1
ENDIF
RETURN
END
```

Table B.4. Parameters Obtained for NPE-953 and NTA-101 at 170°C.

	α	β
NPE-953	10.9	0.27
NTA-101	2.97	1.92

Appendix C. Shear Stress Growth and Shear Stress Relaxation Data - LLDPE and LDPE

This appendix contains shear stress growth and shear stress relaxation data for LLDPE and LDPE at 170^{o}C. In addition, some predictions of the PTT model and the RS model with the PSM damping functions are shown.

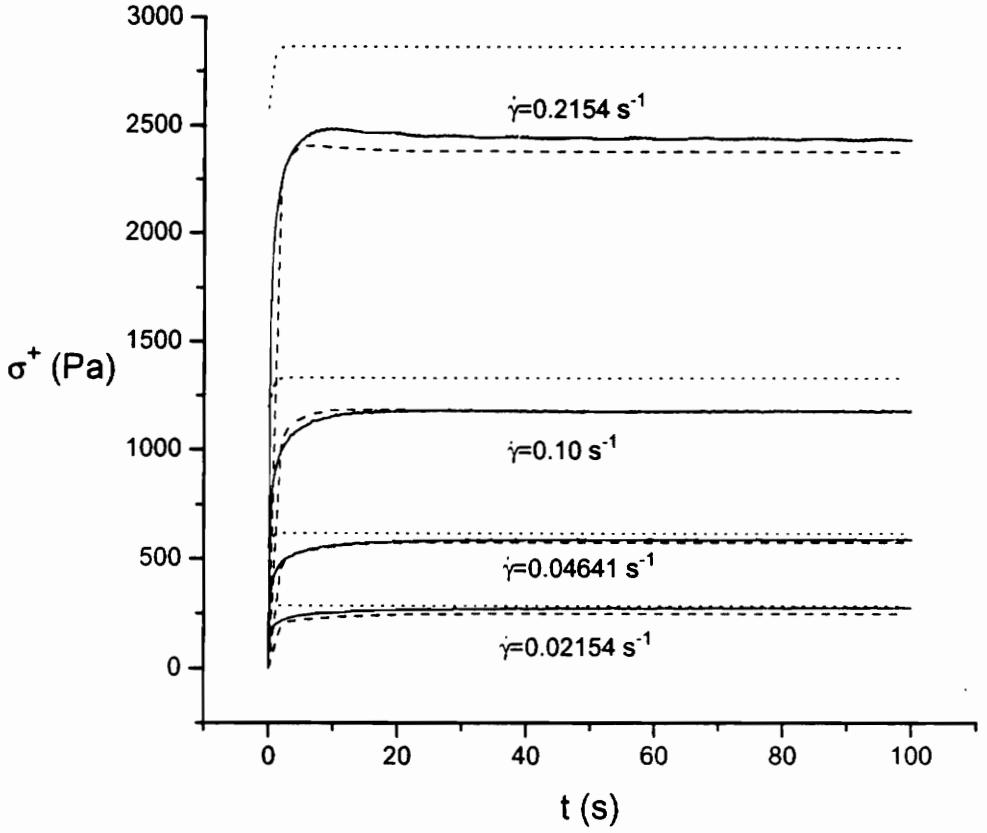

Fig. C1. Shear stress growth upon inception of steady shear flow for LLDPE at 170°C. Experimental (———), PTT model (·····), RS model with PSM damping function (- - - - -).

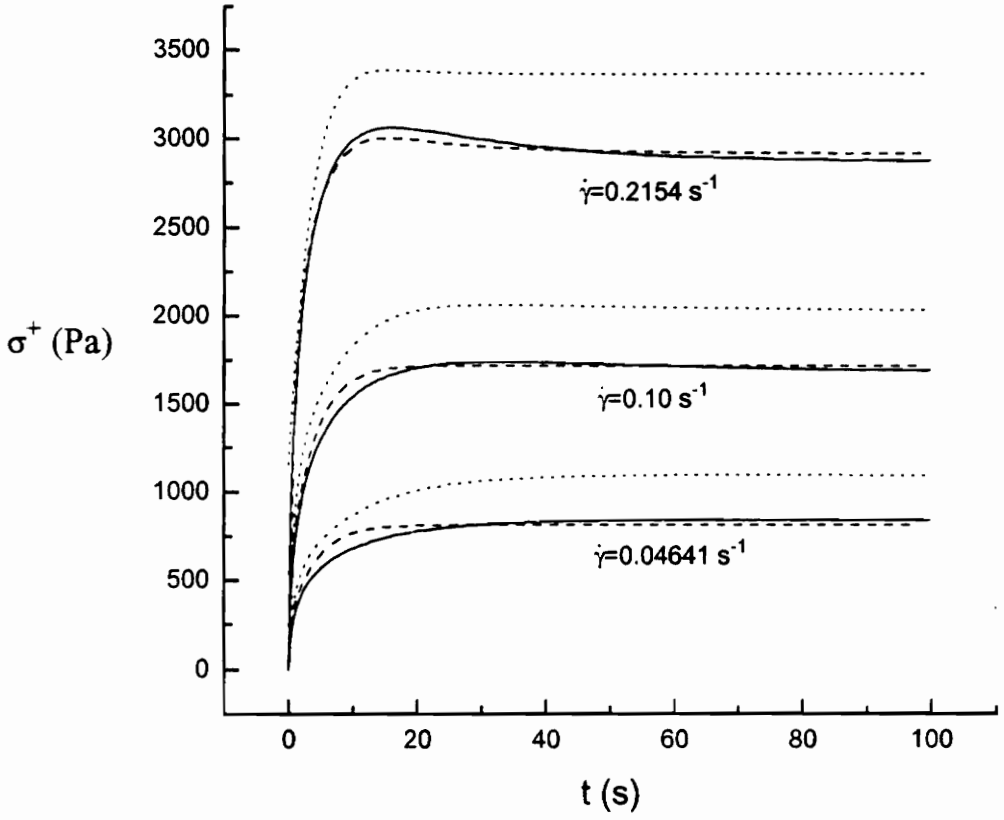

Fig. C2. Shear stress growth upon inception of steady shear flow for LDPE at 170°C. Experimental (———), PTT model (·····), RS model with PSM damping function (- - - - -).

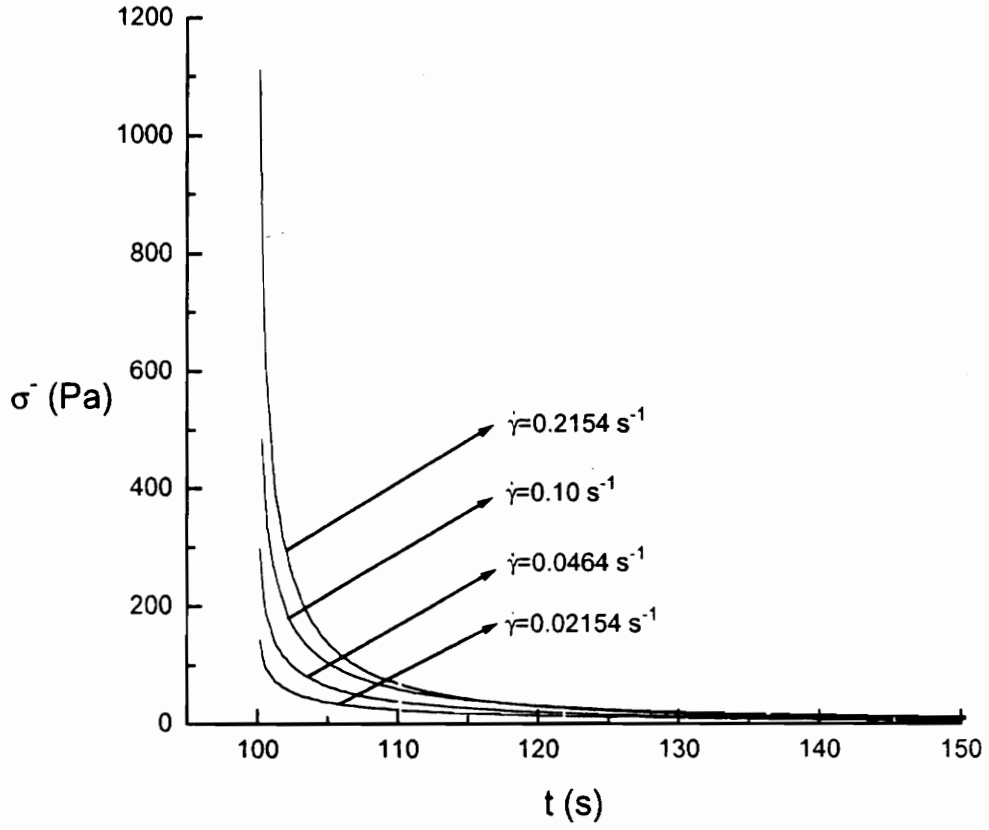

Fig. C3. Stress relaxation upon cessation of steady shear flow for LLDPE at 170°C. Same conventions as Fig. C1.

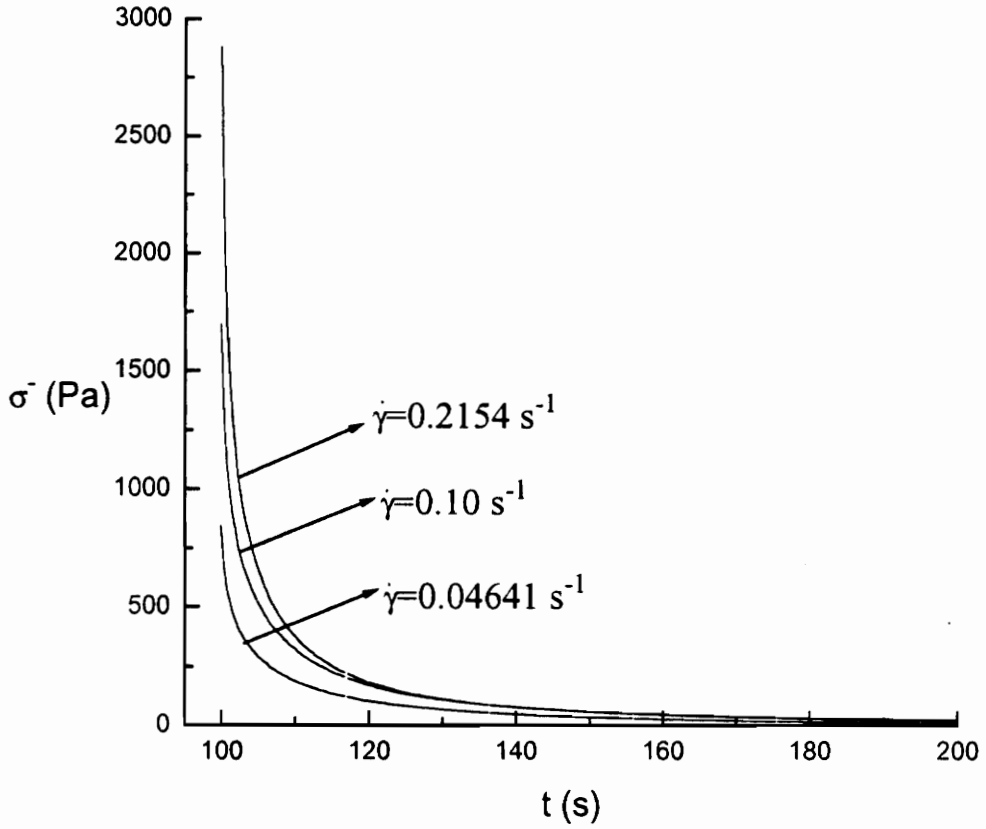

Fig. C4. Stress relaxation upon cessation of steady shear flow for LDPE at 170°C. Same conventions as Fig. C2 are used.

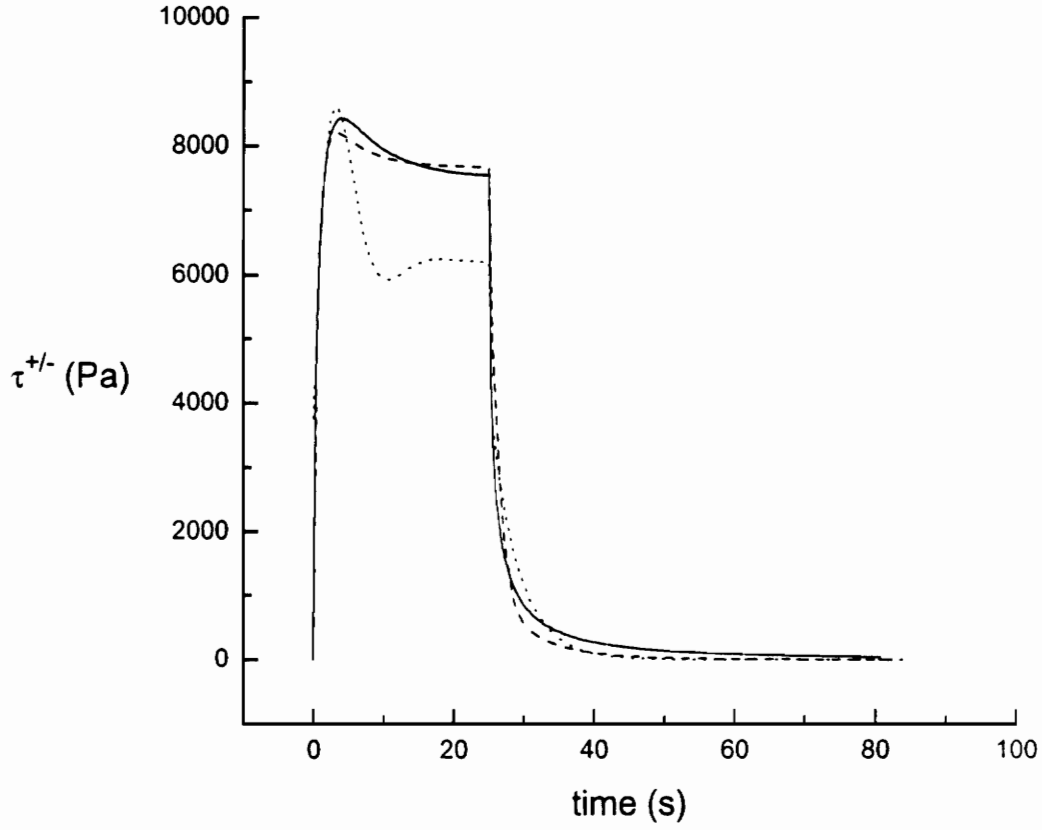

Fig. C5. Shear stress growth upon inception of steady shear flow and stress relaxation upon cessation of steady shear flow for LDPE at 170°C and a shear rate of $1.0s^{-1}$: experimental (———); predictions of RS model with PSM damping function (- - - - -); predictions of PTT model (·····).

Appendix D. Computer Program to Calculate Predictions of Rivlin-Sawyers Model with Papanastasiou, Scriven, and Macosko Damping Function in Homogeneous Flow Fields.

The following is a FORTRAN program which calculates the stresses predicted by the Rivlin-Sawyers constitutive equation with the Papanastasiou, Scriven, and Macosko damping function. This program utilizes the *Numerical Recipes* [1] subroutines STIFFBS, LUBKSB, LUDCMP, and two user supplied subroutines, DERIVS and JACBN.

The subroutines DERIVS and JACBN have been set up so that the user need only supply the parameter values in MAIN, and expressions related to the Finger strain tensor (**B**). The quantities related to **B** are as follows:

$B12 = B_{ij}$

$B1 = I_B$

$B2 = II_B$

$$DB12 = \frac{dB_{ij}}{dt'}$$

$$DB1 = \frac{dI_B}{dt'}$$

$$DB2 = \frac{dII_B}{dt'}$$

$G = \gamma$

where

$$I_B = tr(B_{ij})$$

$$II_B = \frac{1}{2}\left(I_B^2 - trB_{ij}^2\right).$$

The Finger strain tensor depends on the strain history, which is different for each integration range of t' (i.e. -∞ to 0, 0 to t_1,...). The value of -∞ is taken to be 1.E-6. Different values should be tested for accuracy of the predicted stress.

Table D1. Program XSTIFF Listing.

```
      PROGRAM XSTIFF
      INTEGER KMAXX,NMAX
      PARAMETER(KMAXX=200,NMAX=50)
      INTEGER KMAX,KOUNT,NBAD,NOK,INT,L
      REAL DXSAV,EPS,HSTART,X1,X2,Y(1),XP,YP,A(7),R(7),G1,G2,PAR1,par2,
     *     T12P,T12PP,T12,TIME,T1,DELTAT,T12P3,tr
      COMMON                                                    /PATH/
KMAX,KOUNT,DXSAV,XP(KMAXX),YP(NMAX,KMAXX)
      COMMON /RELAX/ A,R,PAR1,par2,G1,G2,INT,TIME,T1,T2

      open(5,file='tr.dat')
      read(5,1)tr
    1 format(5x,f5.2)

      KMAX=0.
      EPS=1.0e-6
      HSTART=1.


      Y(1)=0.
      A(1)=85.
      A(2)=550.
      A(3)=2100.
      A(4)=7900.
      A(5)=12000.
      A(6)=7600.
      A(7)=.2
      R(1)=1.e-3
      R(2)=1.e-2
      R(3)=1.e-1
      R(4)=1.
```

```
R(5)=10.
R(6)=100.
R(7)=1000.
PAR1=10.9
PAR2=0.021

deltat=0.1
T1=15.
t2=t1+tr
TIME=t2+deltat
G1=1.0
G2=0.0

DO L=1,50
T12=0.
INT=1
X1=-1E6
X2=0.
CALL ODEINT(Y,1,X1,X2,EPS,HSTART,0.,NOK,NBAD)
T12P=Y(1)
NOK=0
NBAD=0
Y(1)=0.
INT=2
X1=0.
X2=T1
CALL ODEINT(Y,1,X1,X2,EPS,HSTART,0.,NOK,NBAD)
NOK=0
NBAD=0
T12PP=Y(1)
Y(1)=0.
X1=T1
X2=T2
INT=3
CALL ODEINT(Y,1,X1,X2,EPS,HSTART,0.,NOK,NBAD)
NOK=0
NBAD=0
T12P3=Y(1)
Y(1)=0.0
X1=T2
X2=TIME
INT=4
CALL ODEINT(Y,1,X1,X2,EPS,HSTART,0.,NOK,NBAD)
```

```
      NOK=0
      NBAD=0
      T12P4=Y(1)
      Y(1)=0.0

      T12=-(T12P+T12PP+T12P3+T12P4)
      WRITE(*,11)time,T12
      TIME=TIME+DELTAT

      ENDDO

  999 WRITE(*,*) 'NORMAL COMPLETION'
   11 FORMAT(2X,F7.2,3F15.3)
      STOP
      END
C
C
      SUBROUTINE STIF(Y,DYDX,N,X,HTRY,EPS,YSCAL,HDID,HNEXT)
      INTEGER N,NMAX,MAXTRY
      REAL
EPS,HDID,HNEXT,HTRY,X,DYDX(N),Y(N),YSCAL(N),SAFETY,GROW,
     *    PGROW,SHRNK,PSHRNK,ERRCON,GAM,A21,A31,A32,A2X,A3X,C21,
     *    C31,C32,C41,C42,C43,B1,B2,B3,B4,E1,E2,E3,E4,C1X,C2X,C3X,
     *    C4X
c     EXTERNAL DERIVS
      PARAMETER (NMAX=50,SAFETY=0.9,GROW=1.5,PGROW=-.25,
     *        SHRNK=0.5,PSHRNK=-1./3.,ERRCON=.1296,MAXTRY=40)
      PARAMETER (GAM=1./2.,A21=2.,A31=48./25.,A32=6./25.,C21=-8.,
     *        C31=372./25.,C32=12./5.,C41=-112./125.,C42=-54./125.,
     *        C43=-2./5.,B1=19./9.,B2=1./2.,B3=25./108.,B4=125./108.,
     *        E1=17./54.,E2=7./36.,E3=0.,E4=125./108.,C1X=1./2.,
     *        C2X=-3./2.,C3X=121./50.,C4X=29./250.,A2X=1.,A3X=3./5.)
      INTEGER I,J,JTRY,INDX(NMAX)
      REAL
D,ERRMAX,H,XSAV,A(NMAX,NMAX),DFDX(NMAX),DFDY(NMAX,NMAX),
     *    DYSAV(NMAX),ERR(NMAX),G1(NMAX),G2(NMAX),G3(NMAX),
     *    G4(NMAX),YSAV(NMAX)
      XSAV=X
      DO I=1,N
         YSAV(I)=Y(I)
         DYSAV(I)=DYDX(I)
      ENDDO
      CALL JACOBN(XSAV,YSAV,DFDX,DFDY,N,NMAX)
```

```
      H=HTRY
      DO JTRY=1,MAXTRY
        DO I=1,N
              DO J=1,N
                A(I,J)=-DFDY(I,J)
              ENDDO
              A(I,I)=1./(GAM*H)+A(I,I)
        ENDDO
        CALL LUDCMP(A,N,NMAX,INDX,D)
        DO I=1,N
              G1(I)=DYSAV(I)+H*C1X*DFDX(I)
        ENDDO
        CALL LUBKSB(A,N,NMAX,INDX,G1)
        Do I=1,N
              Y(I)=YSAV(I)+A21*G1(I)
        ENDDO
        X=XSAV+A2X*H
        CALL DERIVS(X,Y,DYDX)
        DO I=1,N
              G2(I)=DYDX(I)+H*C2X*DFDX(I)+C21*G1(I)/H
        ENDDO
        CALL LUBKSB(A,N,NMAX,INDX,G2)
        DO I=1,N
              Y(I)=YSAV(I)+A31*G1(I)+A32*G2(I)
        ENDDO
        X=XSAV+A3X*H
        CALL DERIVS(X,Y,DYDX)
        DO I=1,N
              G3(I)=DYDX(I)+H*C3X*DFDX(I)+(C31*G1(I)+
     *        C32*G2(I))/H
        ENDDO
        CALL LUBKSB(A,N,NMAX,INDX,G3)
        DO I=1,N
              G4(I)=DYDX(I)+H*C4X*DFDX(I)+(C41*G1(I)+
     *    C42*G2(I)+C43*G3(I))/H
        ENDDO
        CALL LUBKSB(A,N,NMAX,INDX,G4)
        DO I=1,N
              Y(I)=YSAV(I)+B1*G1(I)+B2*G2(I)+B3*G3(I)+B4*G4(I)
              ERR(I)=E1*G1(I)+E2*G2(I)+E3*G3(I)+E4*G4(I)
        ENDDO
        X=XSAV+H
        IF(X.EQ.XSAV)PAUSE 'STEPSIZE NOT SIGNIFICANT IN STIFF'
```

```
      ERRMAX=0.
      DO I=1,N
            ERRMAX=MAX(ERRMAX,ABS(ERR(I)/YSCAL(I)))
      ENDDO
      ERRMAX=ERRMAX/EPS
      IF(ERRMAX.LE.1.)THEN
            HDID=H
            IF(ERRMAX.GT.ERRCON)THEN
                  HNEXT=SAFETY*H*ERRMAX**PGROW
            ELSE
                  HNEXT=GROW*H
            ENDIF
            RETURN
      ELSE
            HNEXT=SAFETY*H*ERRMAX**PSHRNK
            H=SIGN(MAX(ABS(HNEXT),SHRNK*ABS(H)),H)
      ENDIF
   ENDDO
   PAUSE 'EXCEEDED MAXTRY IN STIFF'
   END
C
C
   SUBROUTINE LUBKSB(A,N,NP,INDX,B)
   DIMENSION A(NP,NP),INDX(N),B(N)
   II=0
   DO 12 I=1,N
      LL=INDX(I)
      SUM=B(LL)
      B(LL)=B(I)
      IF (II.NE.0)THEN
       DO 11 J=II,I-1
         SUM=SUM-A(I,J)*B(J)
11     CONTINUE
      ELSE IF (SUM.NE.0.) THEN
       II=I
      ENDIF
      B(I)=SUM
12  CONTINUE
   DO 14 I=N,1,-1
      SUM=B(I)
      IF(I.LT.N)THEN
       DO 13 J=I+1,N
         SUM=SUM-A(I,J)*B(J)
```

```
13      CONTINUE
        ENDIF
        B(I)=SUM/A(I,I)
14    CONTINUE
    RETURN
    END
C
C
    SUBROUTINE LUDCMP(A,N,NP,INDX,D)
    PARAMETER (NMAX=100,TINY=1.0E-20)
    DIMENSION A(NP,NP),INDX(N),VV(NMAX)
    D=1.
    DO 12 I=1,N
        AAMAX=0.
        DO 11 J=1,N
          IF (ABS(A(I,J)).GT.AAMAX) AAMAX=ABS(A(I,J))
11      CONTINUE
        IF (AAMAX.EQ.0.) PAUSE 'Singular matrix.'
        VV(I)=1./AAMAX
12    CONTINUE
    DO 19 J=1,N
        IF (J.GT.1) THEN
          DO 14 I=1,J-1
            SUM=A(I,J)
            IF (I.GT.1)THEN
              DO 13 K=1,I-1
                  SUM=SUM-A(I,K)*A(K,J)
13            CONTINUE
              A(I,J)=SUM
            ENDIF
14        CONTINUE
        ENDIF
        AAMAX=0.
        DO 16 I=J,N
          SUM=A(I,J)
          IF (J.GT.1)THEN
            DO 15 K=1,J-1
              SUM=SUM-A(I,K)*A(K,J)
15          CONTINUE
            A(I,J)=SUM
          ENDIF
          DUM=VV(I)*ABS(SUM)
          IF (DUM.GE.AAMAX) THEN
```

```
          IMAX=I
          AAMAX=DUM
         ENDIF
16     CONTINUE
        IF (J.NE.IMAX)THEN
         DO 17 K=1,N
          DUM=A(IMAX,K)
          A(IMAX,K)=A(J,K)
          A(J,K)=DUM
17       CONTINUE
         D=-D
         VV(IMAX)=VV(J)
        ENDIF
        INDX(J)=IMAX
        IF(J.NE.N)THEN
         IF(A(J,J).EQ.0.)A(J,J)=TINY
         DUM=1./A(J,J)
         DO 18 I=J+1,N
          A(I,J)=A(I,J)*DUM
18       CONTINUE
        ENDIF
19    CONTINUE
    IF(A(N,N).EQ.0.)A(N,N)=TINY
    RETURN
    END
C
C
    SUBROUTINE ODEINT(YSTART,NVAR,X1,X2,EPS,H1,HMIN,NOK,NBAD)
    PARAMETER  (MAXSTP=10000,NMAX=50,TWO=2.0,ZERO=0.0,TINY=1.E-
30)
    COMMON /PATH/ KMAX,KOUNT,DXSAV,XP(200),YP(50,200)
    DIMENSION YSTART(NVAR),YSCAL(NMAX),Y(NMAX),DYDX(NMAX)
    X=X1
    H=SIGN(H1,X2-X1)
    NOK=0
    NBAD=0
    KOUNT=0
    DO 11 I=1,NVAR
       Y(I)=YSTART(I)
11    CONTINUE
    XSAV=X-DXSAV*TWO
    DO 16 NSTP=1,MAXSTP
       CALL DERIVS(X,Y,DYDX)
```

```
        DO 12 I=1,NVAR
          YSCAL(I)=MAX(1.,ABS(Y(I)))
12      CONTINUE
        IF(KMAX.GT.0)THEN
          IF(ABS(X-XSAV).GT.ABS(DXSAV)) THEN
            IF(KOUNT.LT.KMAX-1)THEN
              KOUNT=KOUNT+1
              XP(KOUNT)=X
              DO 13 I=1,NVAR
                YP(I,KOUNT)=Y(I)
13            CONTINUE
              XSAV=X
            ENDIF
          ENDIF
        ENDIF
        IF((X+H-X2)*(X+H-X1).GT.ZERO) H=X2-X
        CALL STIF(Y,DYDX,NVAR,X,H,EPS,YSCAL,HDID,HNEXT)
        IF(HDID.EQ.H)THEN
          NOK=NOK+1
        ELSE
          NBAD=NBAD+1
        ENDIF
        IF((X-X2)*(X2-X1).GE.ZERO)THEN
          DO 14 I=1,NVAR
            YSTART(I)=Y(I)
14        CONTINUE
          IF(KMAX.NE.0)THEN
            KOUNT=KOUNT+1
            XP(KOUNT)=X
            DO 15 I=1,NVAR
              YP(I,KOUNT)=Y(I)
15          CONTINUE
          ENDIF
          RETURN
        ENDIF
        IF(ABS(HNEXT).LT.HMIN) PAUSE 'Stepsize smaller than minimum.'
        H=HNEXT
16    CONTINUE
      PAUSE 'Too many steps.'
      RETURN
      END
C
C
```

```
      SUBROUTINE JACOBN(X,Y,DFDX,DFDY,N,NMAX)
      INTEGER N,NMAX,I,INT
      REAL X,Y(*),DFDX(*),DFDY(NMAX,NMAX),A(7),R(7),SUM,PAR1,G,
     $     A1,A2,A3,A4,G1,G2,B1,B2,B12,DB1,DB2,DB12,TIME,T1,par2
      COMMON /RELAX/ A,R,PAR1,PAR2,G1,G2,INT,TIME,T1,T2

      DO I=1,N
      DO J=1,N
           DFDY(I,J)=0.
      ENDDO
      ENDDO

      DO I=1,N
         DFDX(I)=0.
      ENDDO

      IF (INT.EQ.3) GOTO 2
      IF (INT.EQ.2) GOTO 1
      IF (INT.EQ.4) GOTO 3

      G=-G1*T1-G1*(TIME-T2)
      B12=G
      B1=3.+G**2
      B2=3.+G**2
      DB12=0.
      DB1=0.
      DB2=0.
      GOTO 4

    1 G=-G1*(T1-X)-G1*(TIME-T2)
      B12=G
      B1=3.+G**2
      B2=3.+G**2
      DB12=G1
      DB1=2.*G1*(-G1*(T1-X)-G1*(TIME-T2))
      DB2=DB1
      GOTO 4

    2 G=-G1*(TIME-T2)
      B12=G
      B1=3.+G**2
      B2=3.+G**2
      DB12=0.
```

```
      DB1=0.
      DB2=DB1
      GOTO 4

    3 G=-G1*(TIME-X)
      B12=G
      B1=3.+G**2
      B2=3.+G**2
      DB12=G1
      DB1=-2.*G1**2*(TIME-X)
      DB2=DB1


    4 SUM=0.

      DO I=1,7
           A1=PAR1-3.+PAR2*B1+(1-PAR2)*B2
           A2=PAR1*B12/A1/R(I)
           A3=PAR1*DB12*(PAR1-3.+PAR2*B1+(1-PAR2)*B2)
           A4=PAR1*B12*(PAR2*DB1+(1-PAR2)*DB2)
           SUM=SUM+A(I)/R(I)**2*EXP((X-TIME)/R(I))*(A2+(A3-A4)/A1**2)
      ENDDO
      DFDX(1)=SUM
      CONTINUE
      RETURN
      END
C
C
      SUBROUTINE DERIVS(X,Y,DYDX)
      REAL X,Y(*),DYDX(*),A(7),R(7),PAR1,PAR2,G,B12,B1,B2,SUM1,G1,G2
      INTEGER INT
      COMMON /RELAX/ A,R,PAR1,PAR2,G1,G2,INT,TIME,T1,T2

      IF (INT.EQ.3) GOTO 2
      IF (INT.EQ.2) GOTO 1
      IF (INT.EQ.4) GOTO 3

      G=-G1*T1-G1*(TIME-T2)
      B12=G
      B1=3.+G**2
      B2=3.+G**2
      GOTO 4
```

```
1 G=-G1*(T1-X)-G1*(TIME-T2)
  B12=G
  B1=3.+G**2
  B2=3.+G**2
  GOTO 4

2 G=-G1*(TIME-T2)
  B12=G
  B1=3.+G**2
  B2=3.+G**2
  goto 4

3 G=-G1*(TIME-X)
  B12=G
  B1=3.+G**2
  B2=3.+G**2

4 SUM1=0.
  DO I=1,7
      SUM1=SUM1+A(I)/R(I)**2*EXP(-(TIME-X)/R(I))*
 *      PAR1/(PAR1-3.+PAR2*B1+(1.-PAR2)*B2)*B12
  ENDDO
  DYDX(1)=SUM1

  CONTINUE
  RETURN
  END
```

References

1. W.H. Press, S.A. Teukolsky, W.T. Vetterling, and B.P. Flannery, *Numerical Recipes in FORTRAN*, Cambridge University Press, 1986.

Vita

The author was born in Boston, MA on March 26, 1968. Six months later, he moved to Boca Raton, FL where he graduated from Spanish River Community High School. After receiving his B.S. in Chemical Engineering from Virginia Tech, he immediately began the quest for a Ph.D. At present he lives with his wife in Blacksburg, VA. He is currently a candidate for the Doctor of Philosophy degree in Chemical Engineering at Virginia Tech under the direction of Dr. Donald G. Baird.